An Experimental Investigation of Angled Sight Flame Detectors with 850nm Photodiode Sensor

Development of experimental equipment

Morten Norlemann Holme

A thesis submitted in partial fulfillment of
the requirements for the degree of *Master of Science* in
the subject of Physics; Process Safety Technology

Department of Physics and Technology
University of Bergen
Bergen, Norway
November 2014

Preface

The present work is a master thesis that all graduate students at the master program of Process Safety Technology at the Department of Physics and Technology at the University of Bergen, have to submit as a part of the Master of Science degree. The experimental work has been done at CMR GexCon As at Fantoft and their large-scale test facilities at Sotra.

Acknowledgements

First, I want to thank my supervisors; associate Professor Bjørn J. Arntzen at the University of Bergen, Gisle André Enstad and Ivar Børtnes Kalvatn at CMR GexCon AS. They provided much appreciated support, helpful discussions and feedbacks. I would like to thank you for the degree of freedom given to me during the thesis. I would also like to thank the others at GexCon for making me feel welcome, their openness and kindness towards me for the period I was there. I want to thank the laboratory department for making me feel integrated and for giving me the opportunity to develop the detectors and test them at the large-scale testing site at Sotra.

I would like to thank my beautiful Carina for always being patient, loving and supporting. You are the light when things become dark.

I would also like to thank my parents, Kjell Magne and Anny Margrethe for have given me a safe and secure childhood, and with guidance helped me to become what I am today through endless support. My big brother Jostein does also deserves my thanks. You are the indirect reason for where I am today, regarding thesis about gas explosions. Thank you!

Last, I want to thank the people I became friends with throughout my time at the University of Bergen. I will always remember the exam periods where pointless discussion endured, where we had breaks from the breaks.

Morten N. Holme

Abstract

This thesis describes an experimental investigation of applying photodiodes as sensors inside flame detectors exposed to laminar, transient and turbulent gas explosions, and reflecting environment of various degrees.

Small-scale and large-scale experiments have been carried out, in a 0.135m^3 apparatus and a 50m^3 vessel, respectively, with vented premixed gas explosions. The experimental approach of small-scale is transferable to that of large-scale experiments. Experiments with mixtures of propane/air and methane/air with different fuel-air ratios were carried out.

High-speed cameras recorded the flame front propagations. The time of arrival detected by the flame sensors, in combination with the high-speed videos, made it possible to validate the functionality of the detectors.

Three different optical detectors were investigated, two in small-scale and one in large-scale explosions. A total of 99 tests were carried out, 80 in small scale and 19 in large scale.

The data and experience acquired through tests and optimization in small-scale experiments were used to develop flame detectors for the large-scale experiments. The developed detectors were tested and optimized in a 50m^3 test vessel.

Table of Contents

Abbreviations

BR	Blockage Ratio
DDT	Deflagration to Detonation Transition
DUV	Deep ultraviolet
EMS	Electromagnetic spectrum
EUV	Extreme ultraviolet
FIR	Far infrared
fps	Frames per second
HS	High speed
IFT	Department of Physics and Technology at UoB
IR	Infrared
LabVIEW	Laboratory Virtual Instrumental Engineering Workbench
MIR	Mid infrared
MOGELEG	Mitigation of Gas Explosions Using Inert Gases
NIR	Near infrared
PD(s)	Photodiode(s)
PMMA	Polymethylmethacrylate
rms	Root-mean-square
UoB	University of Bergen
UV	Ultraviolet
VI	Virtual Instrument
VIS	Visible light

Nomenclature

Latin symbols

F	Spectral radiance (W/m^{2}µm)
H	Enthalpy (J)
H_F	Enthalpy of formation (J/mole)
j	Emissive power (W/m^2)
ℓ	Turbulent integral length scale (m)
Mw	Molar weight (kg/mol)
n	Number of mole (mol)
p	Pressure (Pa)
Q	Heat (J)
R	Universal gas constant (8.314 J/mol K)
S	Burning velocity (m/s)
S_F	Burning rate (cm/s)
T	Absolute temperature (K)
t	Time (s)
$T_{ad,f}$	Adiabatic flame temperature (K)
t_F	Flame time (s)
u	Flame velocity (m/s)
u_{lam}	Laminar flame velocity (m/s)
V	Volume (m^3)
W	Work (J)
x	Mole fraction (-)

Dimensionless groups

Ka	Karlovitz number (-)

Constants

c	Speed of light (2.998 x 10^8 m/s)
h	Planck's constant (6.626 x 10^{-34} Js)
k_B	Boltzmann's constant (1.380 x 10^{-23}J/K)
σ	Stefan-Boltzmann's constant (5.670 x 10^{-8} W/m^{2}T^4)

Greek symbols

ϵ	Emissivity (-)
η	Kolmogorov length scale (m?)
λ	Wavelength (nm)
ν	Kinematic viscosity (m^2/s)
ρ	Density (kg/m^3)
τ	time scale (s)
ϕ	Fuel-air ratio (-)

1 Introduction

1.1 Motivation

From the beginning of mining, centuries ago, and until today, gas explosions has been a threat to workers and their surroundings. In mines, methane gas leaking from the bedrock is the most common explosion hazard. Mixtures of methane in the air can in combination with an effective ignition source create a catastrophic outcome.

After the discovery of Ekofisk in 1969, the industrial development of Norway changed drastically, and safety became an important aspect right from the start. Opinions in the industry stated that the safety precautions on the Norwegian Continental Shelf were exaggerated however, after the horrendous Piper Alpha accident the mindset changed drastically throughout the petroleum industry [1]. Experience has shown that "learning by doing" is an effective way of acquiring new knowledge. Unfortunately, this also applies to learning about explosions, which can give rise to much human suffering and grief, as well as material damage and loss of profit[1].

There are several regulations that the petroleum industry is imposed by, e.g. ICS 91 – Construction materials and building, ISO 31000 Risk management, ISO 9000 – Quality management[2] and NORSOK S-001[3], to mention some.

The safety development is always moving forward, trying to improve itself. Regardless of safety precautions, the probability of an accident is always present. However, measures can be implemented to reduce the extent, probability and/or consequence of accidents. One of the main principles for prevention and mitigation of unwanted incidents within the petroleum industry is flame and gas detection. NORSOK S-001[3] sets requirements for the use and functionality of gas and fire/flame detection. Gas detection is primarily a proactive measure and fire/flame a reactive measure. When detecting a flame, the detector gives an alarm to an operator and also the rest of the plant/platform, and could active other relevant measures. The development of these detection principles have become quite extensive and are in development through experimental validation. Due to the fact that flame detection is a reactive measure, it is necessary that the response time is as short as possible, and that the detectors can sustain demanding environmental strain and stresses without losing its integrity, i.e. during a gas explosion.

Flame detectors can also be used to investigate the flame phenomena through research and experiments For CMR GexCon, it is of important interest to obtain accurate flame detectors for several reasons. Mainly to acquire accurate flame velocities and ensuring yes-or-no tests of flame presence, with utmost certainty and accuracy.

1.1.1 Accidental gas explosions

In the event of incidents occurring while safety precautions fail to work as intended, due to various reasons, accidents may happen. The consequences can be catastrophic, leading to loss of materials and damage to personnel, industrial properties and reputation. Worst of all is the loss of lives. Below, is an overview of several severe gas explosions were, unfortunately, people lost their lives or were injured. [1, 4-7]

- Flixborough - June 1. 1974 - Explosion - cyclohexane.
  28 killed and 36 injured.
- Beek, Holland - November 7. 1975. Explosion, C3-C4 hydrocarbon fractions.
  14 killed and 104 injured.
- San Carlos de la Rapita - July 11. 1978. Fire and explosions, a tanker carrying propylene.
  215 killed.
- Arendal, Gothenburg, Sweden - May 8. 1981. Explosion, propane.
  1 killed and 1 injured.
- Mexico City - November 15. 1984. Fire and explosions, PEMEX plant involving LPG.
  500 killed.
- Piper Alpha – July 6. 1988 – Gas explosions and fires.
  167 killed – 62 survived with various levels of injuries
- Pasadena - October 23. 1989 - Fires and explosions, Phillips 66 Company's chemical complex involving a mixture of ethylene, isobutane, hexene and hydrogen.
  23 killed, 130 - 300 injured
- Buncefield, England – December 11. 2005 – Fires and explosions, Buncefield oil storage and transfer depot, Hemel Hempstead.
  43 injured, zero seriously injured nor killed.
- Deep Water Horizon –April 20. 2010, Gulf of Mexico – Fire and Explosion at the Macondo well
  11 killed, 17 injured

1.1.2 Prevention and mitigation of gas explosions

A gas explosion requires five parameters, fuel (gas), oxidant (i.e. oxygen), right mixture (gas concentration), confinement or congestion and finally an ignition. Measures against gas explosions often focus on removing one or several of these parameters.

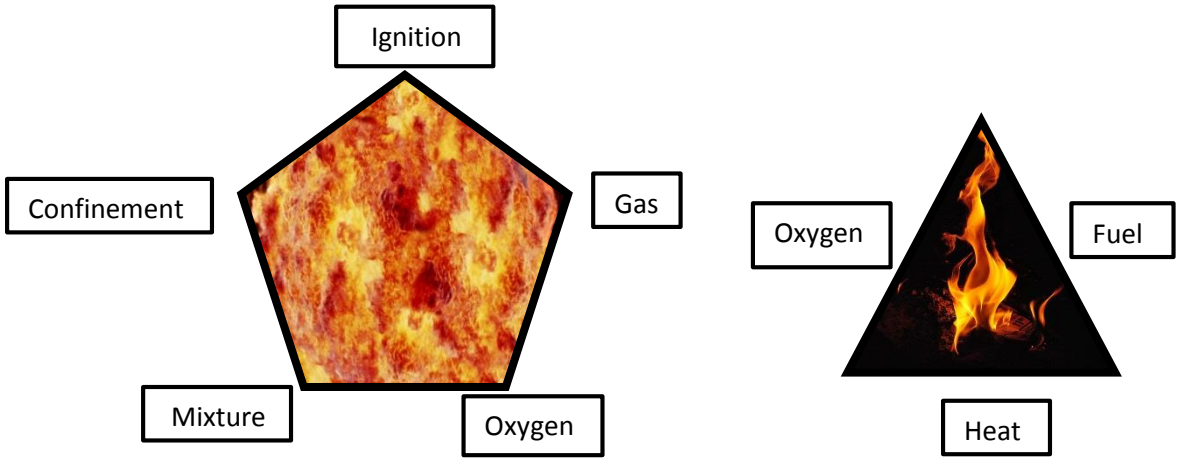

Figure 1-1: The explosion pentagon and the fire triangle.

As a methodology for assessing the hazard risk analysis is often performed. Risk can be defined as the probability times the consequence. How risks are dealt with is often reflected through the management of the present risks. Risk management can be divided into two parts, proactive and reactive. Proactive are measures before incidents and reactive are measures after incidents

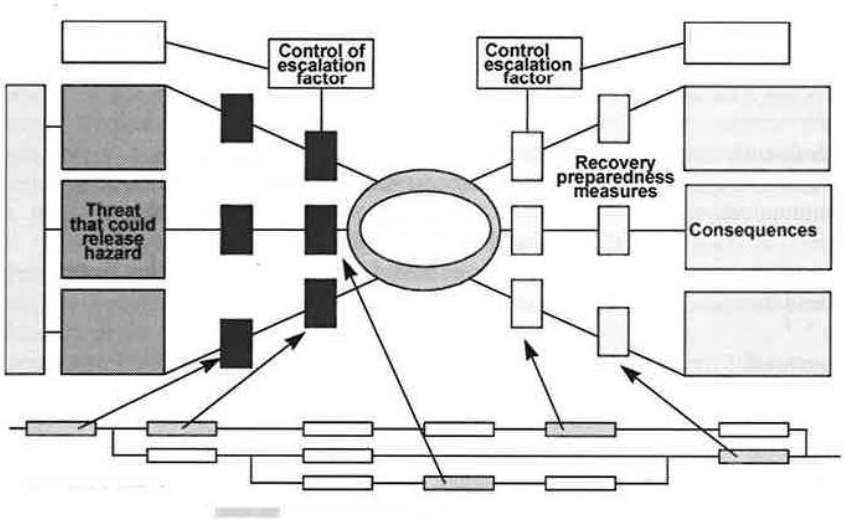

Figure 1-2: General bow-tie principle.

Figure 1-2 shows an example of a bow-tie methodology. Its purpose is to show the sequence of events for a specific accident (i.e. gas explosion), from the initiation of the specific accident to the consequences of the accident, and its barriers to stop the events. The light grey boxes at the left, represents initiating conditions or causes, the black boxes representing barriers intended to stop the sequence of events to developing into an accident (the ring). The big white boxes on the right is the consequences of the accident, the small white ones between consequence and accident represents the barriers which are supposed to stop the sequence of events and after accident, hence, reducing its consequences. Summarized, the proactive measures are on the left side of accident and the reactive measures on the right side. In other words, flame detection is represented on the right side of the accident as a reactive measure, inside the small white boxes.

The following overall aims have high priority in gas explosion risk management [1]:

- Prevention and control of potential leaks of combustible gases (proactive)
- Good ventilation to minimize extent and duration of explosive atmosphere due to gas releases (proactive)
- Prevention and control of possible ignition sources (proactive)
- Minimizing high equipment congestion/blockage to ease explosion venting, and to minimize flow-induced turbulence during gas cloud formation and explosion (reactive)
- Installation of blast and fire barriers (reactive)

1.1.3 Flame detection

There are many types of flammable gases. Hydrocarbon gases are among the most known and applied. These gases have different properties, i.e. flammability, explosive concentration range, etc. There are many ways to detect a flame and there are discussions around how to detect it accurately.

In the Norwegian oil sector, flame detectors have been used during recent decades. These detectors are a part of a fire detection system, which monitors the specific plant continuously. There are different requirements for offshore and onshore applications of the detectors.

There are multiple types of these detectors depending on requirements. Spectrex Inc. is one of the companies that deliver these detection systems and have used them on Asgard FPSO and Norne in the North Sea. [8]

The flame detector from Spectrex in Figure 1-3, is sensitive at three small and specific wavelengths intervals where characteristic emissions regarding flames occur, hence, removing the chance for fail-detection.

Figure 1-3: Spectrex's ultra fast SharpEye IR3 flame detector, detecting at three wavelengths.

Onshore, on the other hand, Spectrex has delivered flame detectors for a various number of plants, including Enagas Barcelona Offloading Terminal and Tank Farm, Lek Process Plant Ljubljana, Slovenia.

Other suppliers would be Det-Tronics, Siemens, Simtronics Fire & Gas, among others.

1.1.4 The optical measurement principle applied to explosions

Photodiodes (PDs) has been widely used in experiments for flame detection. Their spectral properties may vary. What kind of PD to use depends on the electromagnetic radiation produced by the flame. The radiative emissions of combustion processes within the electromagnetic spectra differ by the type of fuel used, e.g.

- Coal
- Oil
- Gas
- Wood, etc.

The difference of radiative properties is due to their different atomic and molecular properties.

Figure 1-4 shows a general spectral radiance distribution of gas and oil flames within the UV, VIS and NIR region.

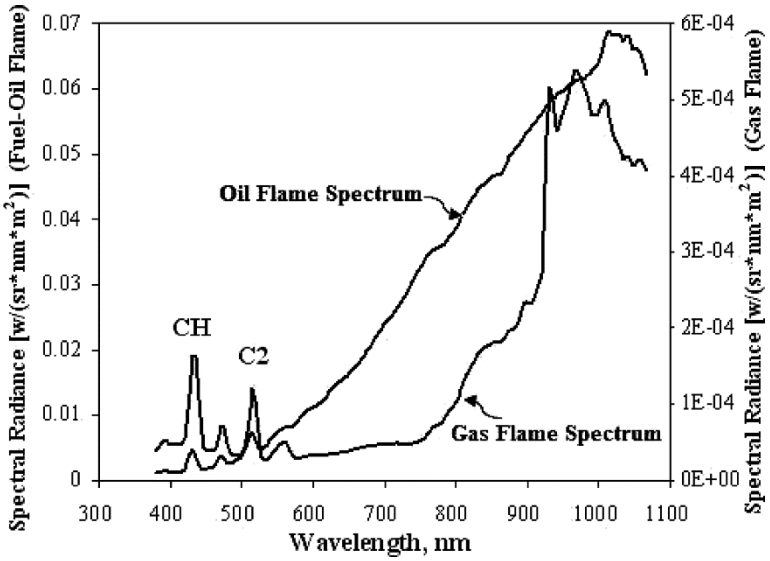

Figure 1-4: Typical spectrum of gas and oil flames.[9]

The main difference between oil flame and gas flame spectra is the presence of a continuous background emission due to the soot formation resulting from the combustion process. It has been shown that the spectral emission of flames is a combination of its monochromatic emissivity ϵ_λ and the Planck's law of black body radiation [9]

One way to detect a flame is with IR flame detection using a single sensor. Since IR radiation is present in most flames due to their temperature and mass of hot gases (reaction products) which emits specific spectral patterns, it is possible to detect these characteristics with IR sensor technology. But since IR is related to heat, all hot surfaces could also be detected by the flame detector sensor.

1.2 Aim of the Current Work

The motivation for the present work is develop accurate and robust flame detectors though studying of properties and behaviors of specific photodiodes detecting flame fronts at different types of combustion, approximated laminar and transient, and turbulent.

The experiments are divided into three parts, preliminary, optimization and large scale testing. The two first part were conducted in a 0.3x0.3x1.5m channel, called the MOGELEG channel. The channel has one closed end and one open end. One of its long sides is fitted with transparent plastic which makes it possible to see the interior of the whole channel, see Figure 1-5. Before each test, flammable gas was mixed with air through a circulation system. After preparing the mixture, the gas was ignited at the closed end. Photodiodes registered the flame propagation towards the opening, and a high speed (HS) camera filmed the process. By examining the video, the accuracy of the photodiodes was determined.

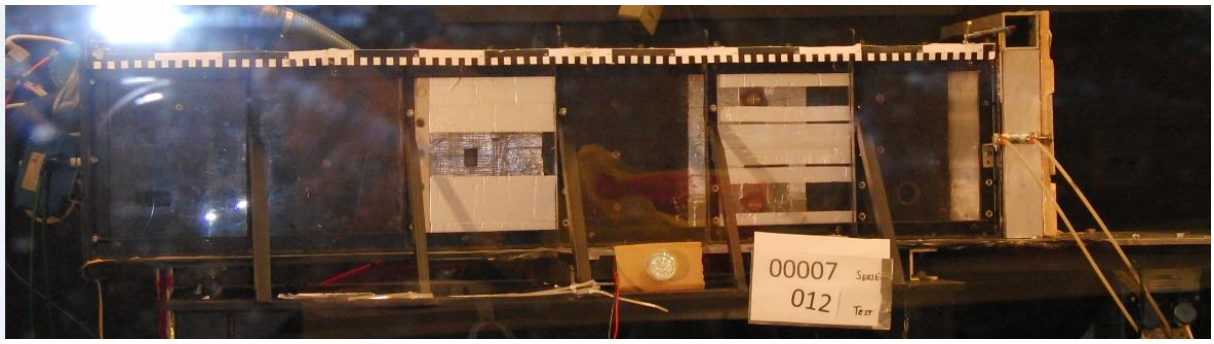

Figure 1-5: The 0.3x0.3x1.5 m MOGELEG channel with transparent plastic front side. Closed end to the left and open end to the right..

The second part, large-scale testing, was performed in a 2.5x2.5x8m downscaled Gullfaks A compressor module. It has the same, approximately, properties as the MOGELEG channel, only on a bigger scale.

The aim for the three experimental parts was as follows:

Preliminary tests

- Testing the basic concept and detector design.
- Investigating the influence of gas concentration for flame detection.

Optimization tests

- Investigation of false flame arrivals due to reflections, and optimization of the detectors.
- Reduce the influence on flame detection due to reflection.

Large-scale tests

- Investigate the performance of detectors in large-scale experiments.
- Test the detection principle at industrial scale.

2 Theory and Previous Work

2.1 Definitions and Basic Concepts

2.1.1 Combustion

The Oxford Dictionary defines the term *combustion* as
" a rapid chemical combination of a substance with oxygen, involving the production of heat and light" [10]

Combustion has been a tool for humans for more than 1 million years, making it our oldest technology. In 2006, the majority (90%) of the energy support is provided by combustion [11].

It is a well-known fact that combustion may be a complicated and intrigued science. Combustion cover multiple scientific branches: chemical kinetics, thermodynamics, fluid dynamics and radiation physics. These branches intervene each other under the terms of combustion.
¨

Multiple processes occur when a candle light is burning. Radiation from the flame, chemical reactions between fuel and oxygen producing water vapor and carbon dioxide. Convection forces between the products leaving the reaction zone (the flame) and the reactants coming into the reaction zone, diffusion forces giving drive to mix the air and fuel molecules. Figure 2-1 show some of these processes.

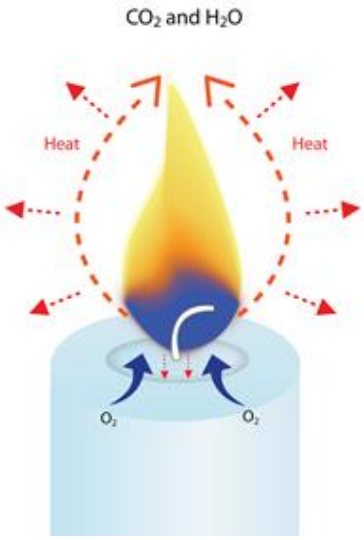

Figure 2-1: Burning process of a candle (from www.candle.org).

A chemical reaction is the exchange and/or rearrangement of atoms between colliding molecules [11]. For a combustion process. This is simplified as

$$Fuel + Oxygen \rightarrow H_2O + CO_2 \qquad 2\text{-}1$$

Combustion consists of two main categories, premixed and non-premixed. For non-premixed combustion, fuel and air is present spatially separated. Combustion takes place in a surface in between the gases. Convection and/or diffusion is transporting fuel into the air, air into the fuel and combustion products away. The combustion regarding the candle light is non-premixed combustion. Premixed

combustion represents a mixture of both fuel and gas that are mixed prior to ignition. The flame burns through the premixed gases, leaving a volume of products behind. In a premixed combustion of a mixture the gas can be divided into two parts, unburnt and burnt mixture with a flame separating them.

Table 2-1 shows different type of premixed and non-premixed combustion with respective examples.

Table 2-1: Basic flame types[11].

Fuel/Oxidizer Mixing	Fluid Motion	Examples
Premixed	Turbulent	Spark-ignited gasoline engine
		Low NO_x stationary gas turbine
	Laminar	Flat flame
		Bunsen burner
Non-Premixed	Turbulent	Pulverized coal combustion
		Aircraft turbine
	Laminar	Wood fire
		Candle

Not all flames are visible for the naked eye. Examples of "invisible" combustion is smoldering combustion in dust [1]. A hydrogen/air flame, however, is barely visible. Figure 2-2 shows two of the most common combustion processes we know of.

Figure 2-2: Two of our most common combustion processes, bonfire with a visible flame and the smoldering combustion of a cigarette.

2.1.2 Basic description of a combustion process

Combustion is a chemical process with the reactants and products. Below is the chemical reaction of a stoichiometric mixture of propane in air (20.9% O_2 and 79.1% N_2).

$$C_3H_8 + 5\left(O_2 + \frac{79{,}1}{20.9}\,N_2\right) \rightarrow 3CO_2 + 4H_2O + 5\frac{79{,}1}{20.9}\,N_2 \qquad 2\text{-}2$$

A stoichiometric mixture implies a mixture where all the reactants on the left side of the arrow are spent producing products (except for N_2, which is an inert gas). We assume all the reactants, inerts and products are in gas phase.

Regarding premixed combustion, it is of interest to know the ratio between fuel and air, Φ. the fuel-air ratio is the actual concentration normalized using the stoichiometric concentration. In general stoichiometric mixtures releases more energy in form of heat and radiation than concentrations both above and under stoichiometry.

$$\Phi = \frac{\left(\frac{n_{fuel}}{n_{air}}\right)_{mixture}}{\left(\frac{n_{fuel}}{n_{air}}\right)_{stoichiometric}} \qquad 2\text{-}3$$

The fuel-air ratio is often divided into three parts that cover the main areas of mixtures, lean, rich and stoichiometric.

Table 2-2: Mixtures described by equivalence ratio

Equivalence ratio	Type of mixture
$\boldsymbol{\Phi < 1}$	Lean – less fuel than air
$\boldsymbol{\Phi > 1}$	Rich – more fuel than air
$\boldsymbol{\Phi = 1}$	Stoichiometric

By using chemical reaction in 2-2 it is possible to find the mole fractions

$$x_i = \frac{n_i}{n_{TOT}} \qquad 2\text{-}4$$

The sum of all mole fractions will always be equal to unity, the same goes for the weight fractions.
When working with gas mixtures it is often convenient to use a weighted average molar weight for later calculations if it is applicable

$$\overline{Mw_{mix}} = \sum_{i}^{N} x_i Mw_i \qquad 2\text{-}5$$

where $\overline{Mw_{mix}}$ is the weighted average molar weight (kg/mole), Mw_i is the molar weight for the respected substance/gas *i* and *N* is the number of substance/gas.

The reactants and the products of the combustion can be considered as *ideal gases*. Hence the equation of state is applicable:

$$pV = nRT \qquad 2\text{-}6$$

Where p - pressure (Pa), V - volume (m^3), n - number of moles, R - universal gas constant (J/K mol) and T - temperature (K).
This assumption is considered valid when we consider the high temperatures obtained during combustion, which generally result in sufficiently low densities for ideal-gas behavior to be a reasonable approximation [11]

When combining the *equation of state*, and the weighted average molar weight it is possible to find the gas density.

$$\rho = \frac{p\overline{Mw_{mix}}}{RT} \qquad 2\text{-}7$$

ρ is the density (kg/m^3), *p* is the pressure (bar), *R* is the universal constant 8.314 (J/K mol) and *T* is temperature (K).

2.1.3 Adiabatic flame temperatures

Combustion is an exothermic reaction. By assuming an adiabatic system, no energy released from the reaction is lost to the surroundings. If the reaction is allowed to approach chemical equilibrium from a specified initial pressure and temperature during a constant pressure process adiabatically, the final temperature attained by the system is called the *adiabatic flame temperature*, T_{ad}. The adiabatic flame temperature depends on the initial pressure, the initial temperature and the composition of the reactants [12].

Since the system is regarded as adiabatic, all the chemical energy released during the reaction of reactants to products raises the temperature and the volume of the system. The correlation is therefore

$$\Delta H_{reactants} = \Delta H_{products} \qquad 2\text{-}8$$

Where the total enthalpy of the reactants is defined as the sum of enthalpy of formation for all reactants.

$$\Delta H_{reactants} = \sum_{j=reactants} n_j \Delta h_{f,j} \qquad 2\text{-}9$$

The total enthalpy of the products is defined as the sum of enthalpy of formation for all products plus the sensible enthalpy from the resulting temperature elevation of the reaction.

$$\Delta H_{products} = \sum_{i=products} n_i \Delta h_{f,i} + \sum_{i=products} \int_{T_{298K}}^{T_f} n_i c_{p,i} dT \qquad 2\text{-}10$$

Hence,

$$\sum_{i=products} \int_{T_{298}}^{T_f} n_i c_{p,i} dT = -\Delta H^o_{reaction,298K} \qquad 2\text{-}11$$

By Hess' law interpretation of T_f

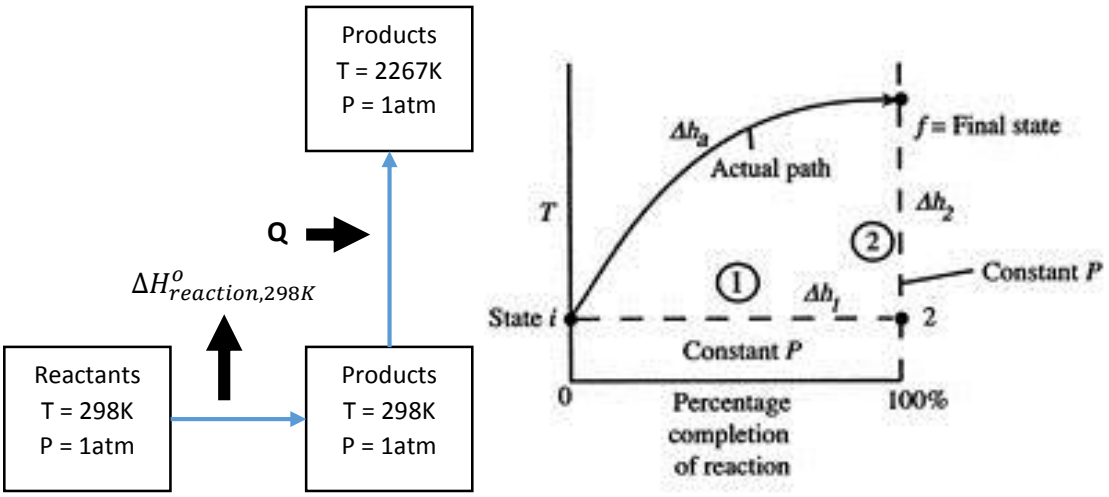

Figure 2-3: Hess' law interpretation of T_f, from [12],[13].

Since the heat capacities for both reactants and products are temperature dependent, a simplification is necessary to avoid complicated calculations. Temperature estimation can be done by iteration using equation 2-11 [12] and by finding new mean heat capacity for every step.

2.2 Premixed Combustion

If a mixture of fuel and oxidizer is within the flammability limits a flame will propagate through the mixture from the point of ignition. For premixed combustion, these limits are called upper explosive limit (UEL) and lower explosive limits (LEL) and differ for various gases, see Table 2-1.

Table 2-3: Explosion limits for propane and methane

Explosion limits	LEL (vol-%)	UEL (vol-%)
Propane	2.1	9.5
Methane	5	15

Heat release combined with temperature sensitive reaction chemistry, i.e. chain branching and chain braking, generates combustion phenomena like ignition and extinction.

Figure 2-4 shows the maximum temperature in a homogeneous flow combustor as function of the Damköhler number, which is represented by equation 2-12. The lower branch represents a combustor prior to ignition which is slowly reacting due to the short residence time, preventing thermal runaway. Lowering the flow rate, hence, increasing the residence time leads to an increase of the Damköhler number until it reaches point I, ignition. If Da reaches a value higher than Da_I, then the flow goes through a rapid and unsteady transition to the upper close-to-equilibrium branch. If the flow rate is in a close-to-equilibrium and the value of Da is decreased by reducing the residence time until Da_Q is reached and beyond, the reaction will be extinct. Hence, the flow becomes slow reacting again.

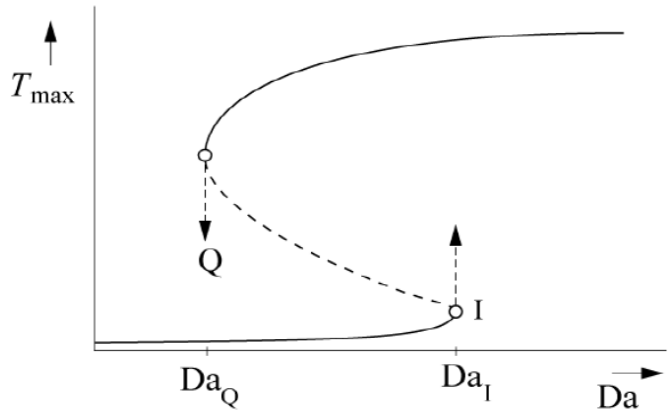

Figure 2-4: The Damköhler number's dependency on temperature of the flow.[14]

The Damköhler number is an expression for the relationship between the reaction time scale (reaction rate) and the convection time scale (flow rate);

$$Da = \frac{residence\ time}{chemical\ time} \qquad 2\text{-}12$$

2.2.1 One-dimensional combustion model - laminar flame velocity

By combining the enthalpy, first law of thermodynamics, the law of continuity and calculating the adiabatic flame temperature, one can derive an expression for the laminar flame velocity by using a one-dimensional combustion model. The premixed is ignited at the closed end and the flame propagates towards the open end. The pipe is still while the flame front burns with the flame speed *S*. The unburned mixture flows from the right to the left in Figure 2-6 [15].

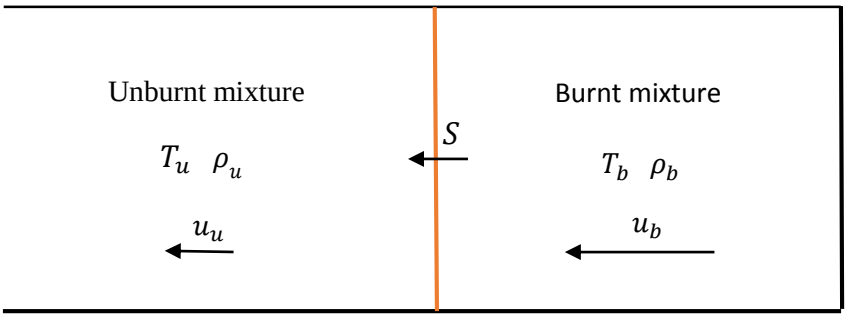

Figure 2-5: one-dimensional combustion model

Figure 2-6 shows a predicted structure of a premixed laminar methane/air flame, which is the interface between the unburnt mixture and the burnt mixture.

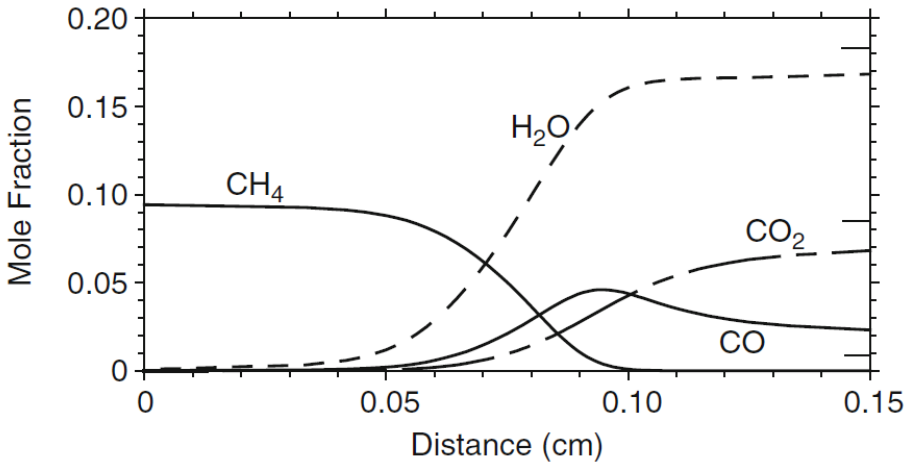

Figure 2-6: Predicted structure of premixed laminar stoichiometric methane-air flame[15]

2.2.2 Turbulence

A characteristic feature of turbulent flows is the occurrence of eddies of different length scales [16]. As Figure 2-7 shows, there are different type of flows when adding fuel with a high velocity through a nozzle and into initially quiescent air. It is observable that the fuel's flow pattern changes after it exits the nozzle. Firstly, it is quite laminar with unstable shear layer between itself and the surrounding air due to the high velocity difference between the fuel and the air[16]. Secondly, a transition to turbulence occurs, where the shear layer disintegrates and eddies generating turbulence occur The center flow remains almost the same. Thirdly, the generated eddies occur all over the fuel flow and a fully developed turbulent jet is present.

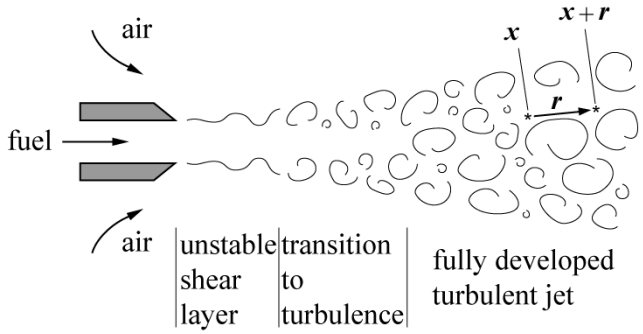

Figure 2-7: A schematic illustration of a jet flow into quiescent air [16].

Eddies are being generated in the flow of Figure 2-7, small in the beginning and larger at the end. The sizes of eddies are explained by length scales. Most known is the Kolmogorov length scale, η, which is the smallest eddy size where the kinetic energy is larger than the diffusion, and the integral length scale, ℓ, representing the eddy sizes which account for most of the kinetic energy in a turbulent flow. Figure 2-8 shows an example of the energy distribution in a turbulent flow, or turbulent field. The energy is transported from large eddies into smaller ones, and are dissipated into heat when the eddies are the same size as the Kolmogorov length scale.

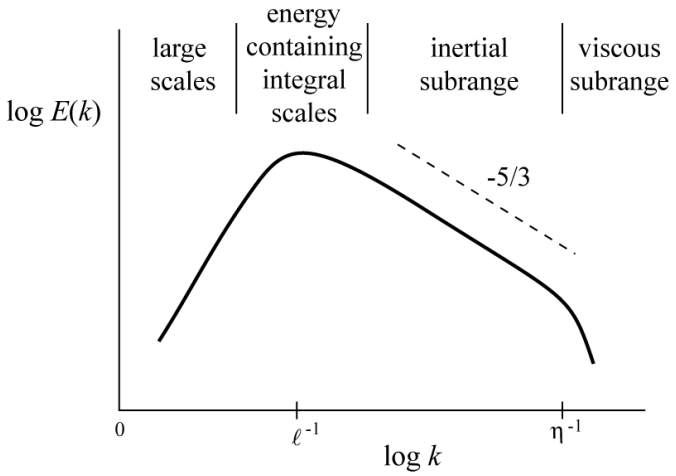

Figure 2-8: Example of an energy spectrum of the entire wave number range for a turbulent flow

The regime diagram for premixed turbulent combustion processes in Figure 2-9 depends on the length scales, turbulent velocity fluctuation.

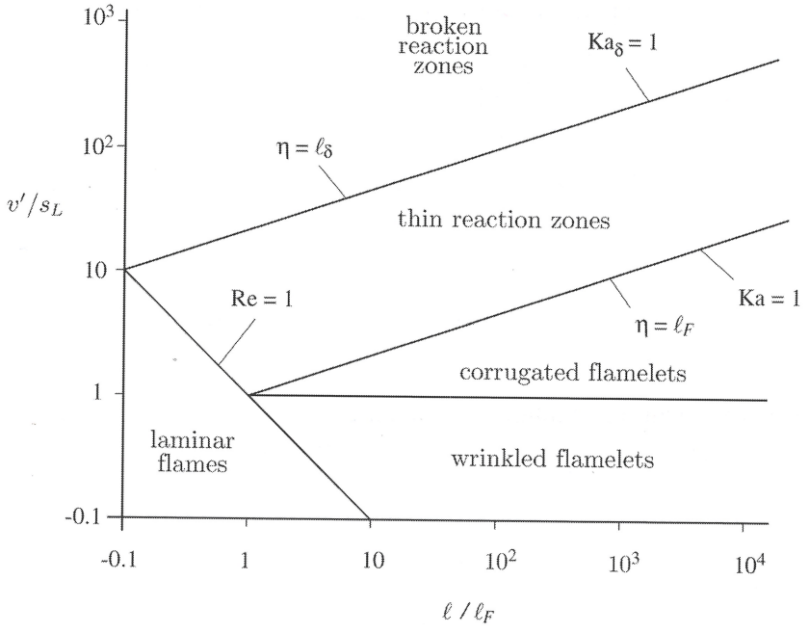

Figure 2-9: Regime diagram for premixed turbulent combustion processes [16].

2.2.3 Gas explosion

CMR GexCon defines a gas explosion as a process where combustion of a premixed gas cloud, i.e. fuel-air or fuel-oxidizer, is causing rapid increase of pressure[17].

The consequences of a gas explosion depends on the environment in which the gas cloud is contained or which the gas cloud engulfs. Therefore, it has been common to classify a gas explosion from the environment where the explosion takes place:

I. Confined Gas Explosions (within vessels, pipes, channels or tunnels)
II. Partly Confined Gas Explosions (in a compartment, buildings or off-shore modules)
III. Unconfined Gas Explosions (in process plants and other unconfined areas)

These terms are not strictly defined. In events of an accident it may be hard to classify the explosion, i.e. an unconfined explosion in a process plant may also involve partly confined explosions in compartments into which the gas cloud has leaked [17].

From the classifications of CMR GexCon's *Gas Explosion Handbook*, the experiments conducted in this thesis will be considered *partly confined*, meaning that explosion occur inside a geometry which is partly open.

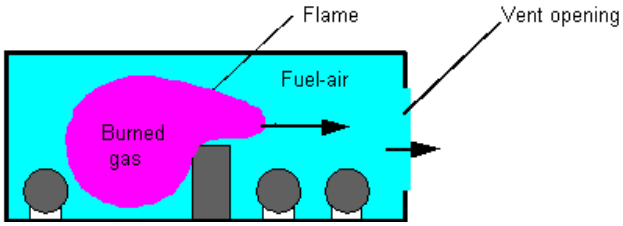

Figure 2-10: Partly confined explosion.[17].

2.3 The Electromagnetic Spectrum and Radiation

The electromagnetic spectrum describes the main characteristic of different types of radiation, from the longest wave that exists – radio waves – and to the shortest waves – nuclear radiation. Visible light – which we see as light and colors, is in the midrange. In a flame, radiation is due to several phenomenon. The main cause of radiation is however glowing gases, due to their highly elevated temperatures.

Infrared radiation by a gas is dependent on its compositions. The emission are discontinuous and consists of few narrow bands dispersed over the infrared spectrum. The IR radiation occurs at the wavelength(s) correspond to its atoms' and/or molecules' vibrations frequencies. The different modes of vibrations are dependent the degrees of freedom of the relevant molecules within the gas.

The energy relating the wavelengths above can be calculated with help equation 2-13.

$$\Delta E = hf \qquad 2\text{-}13$$

where h is the *Planck's constant* (6.62606876 x 10^{-34} J s), where the relation of the frequency is represented by

$$c = \frac{\lambda}{f} \qquad 2\text{-}14$$

c represents the speed of light, λ the wavelength. At lower wavelengths, the frequency is higher and the radiation is more energetic due to the more movement of atoms, molecules, photons and other sub particles.

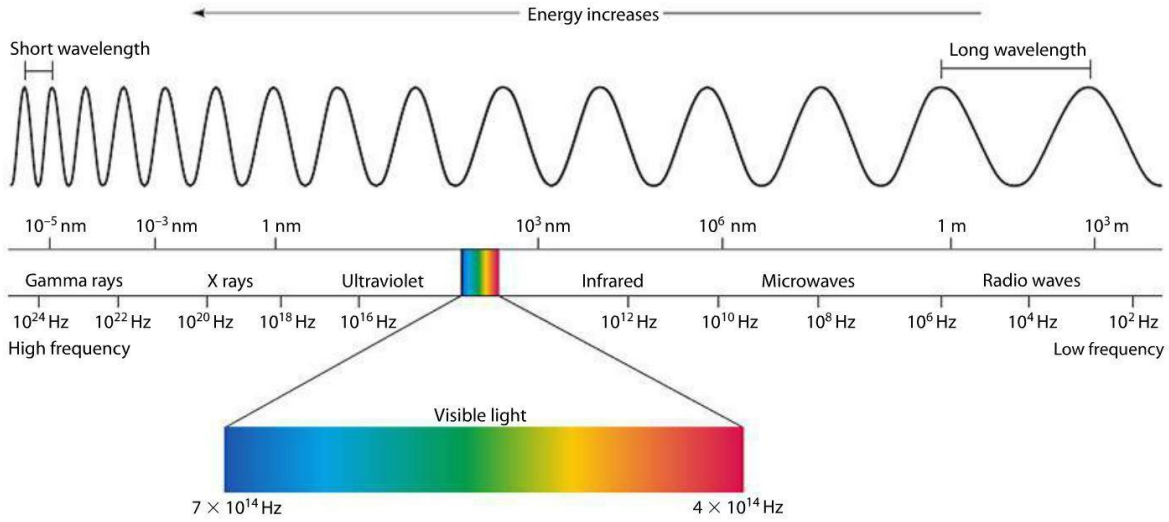

Figure 2-11: The electromagnetic spectrum (from studyblue.com).

When discussing thermal radiation, it is common to assess the radiation within the ultraviolet (UV), visible (VIS) and infrared (IR) regions. There are several definitions of where the limits between UV, VIS and IR, and their sub limits. The ISO 20473:2007 definitions with respect to wavelength of these regions are shown in the table below.

Table 2-4: ISO 20473:2007 Classification of UV, VIS and IR radiation [2]

Designation of the radiation		**Short designation**			**Wavelength λ nm**
Ultraviolet radiation	Extreme UV	UV		EUV	1 to 100
	Vacuum UV		UV-C	VUV	100 to 190
	Deep UV			DUV	200 to 280
	Mid UV		UV-B		280 to 315
	Near UV		UV-A		315 to 380
Visible radiation, light		VIS			380 to 780
Infrared radiation	Near IR	IR	IR-A	NIR	780 to 1 400
			IR-B		1 400 to 3 000
	Mid IR		IR-C	MIR	3 000 to 50 000
	Far IR			FIR	50 000 to 10^6

2.3.1 Thermal radiation

«The energy radiated by solids, liquids and gases as a result of their temperature." [18]

The Encyclopedia of Science & Technology, 1987 explains that the thermal motion within a gas consists substantially of unhindered movement of the individual particles with different velocities and that its extent depends on the temperature. Hence, the hotter substance the greater thermal motion and higher intensity and energy of the radiation, and vice versa. The emitted radiation shifts to shorter wavelengths as the temperature increases. On the other hand, the amount of radiation decreases until finally at absolute temperature reaches zero kelvin. In this situation, theoretically, the substance radiate no energy because all atomic motion has ceased to exist.[18]

As mentioned earlier, the radiation of a gas depends on the degrees of freedom of its molecules.

When radiation hits an object, one fraction of the radiation will be reflected, one fraction will be absorbed and the last fraction will be transmitted. The sum of these fractions equals unity, often written as

$$r + \alpha + \tau = 1 \qquad \textit{2-15}$$

where r, α and τ are fractions for reflection (reflectivity), absorbed (absorptivity) and transmitted (transmissivity), respectively. These three parameters are material dependent and often looked on as optical properties of the specific material. The reflection, absorption and transmission is shown in Figure 2-12

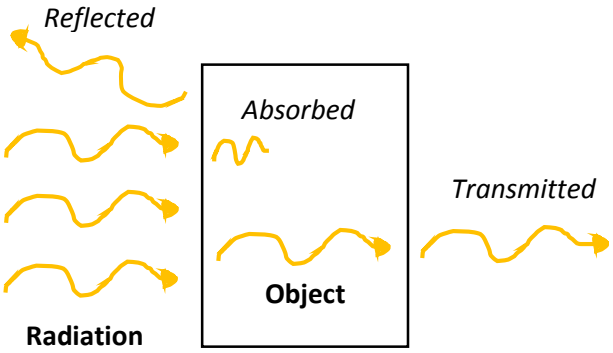

Figure 2-12: Reflection, absorption and transmission regarding an object

Reflectivity is the property of a surface that defines the fraction of incident energy that is reflected by the surface. This property depends not only on the wavelength and directional characteristics, but it also describes the directional distribution of reflected radiation. [19]

2.3.1.1 Black radiation

An *absolute black body* is a hypothetical and ideally object that absorb all radiation, therefore black body. Hence, the transmissivity and reflectivity of the absolute black body equal zero and the absorption equals unity according to equation 2-15.

"Two quantities characterize a heat radiator completely: the total emissivity and the spectral emissivity, which are designated by ε and ε_λ, respectively. Both emissivities, in conjunction with the radiation properties of a blackbody, describe fully the behavior of a real heat radiator."[18]

In *Generell fysikk for universiteter og høgskoler bind 2* from 2006, the authors describe an approximated black body as a hole in a box that has blackened interior so that a negligible amount radiation escapes back through the hole. If the box is at thermal equilibrium, the energy absorbed is emitted back out again as black body radiation.

By assuming thermal equilibrium for the hole, temperature T for the radiation inside the box and the radiation as a cloud of photons, then by using the second law of thermodynamic (equation 2-16) it is possible to show that the energy density *u* is only dependent on temperature T .

$$dS = \frac{\delta Q}{T} \qquad \textit{2-16}$$

By using the averaged number of molecules impacting against a hole per time unit (of time?) and unit of area [20]

$$\langle N \rangle = \frac{1}{4}\rho\langle v \rangle$$

$$q_b = \frac{1}{4}u(T)c \qquad \textit{2-17}$$

or

$$q_b = \sigma T^4$$

where ρ and $\langle v \rangle$ are the molecule density and averaged molecule velocity, respectively. By assuming the photons have a uniform speed (speed of light) *c*, and by substituting the molecule density with the energy density one has

- the *Stefan-Boltzmann's law*, where σ is the *Stefan-Boltzmann's constant* (5.670400 x 10^{-8} $Wm^{-2}K^{-4}$).

From [20], the definition of a *grey body* is when the absorption coefficient, *α*, is less than unity. By assuming that the grey body emits the fraction, ε, of what a black body does. Through an energy balance at thermodynamic equilibrium, it can be shown that the directional spectral emissivity is always equal to the directional spectral absorptivity of the source (from Kirchhoff's law):

$$\epsilon = \alpha$$

Stefan-Boltzmann's law for a grey body

$$q = A\epsilon\sigma T^4 \qquad \textit{2-18}$$

It is impossible for an object to be completely isolated from thermal radiation by the surroundings. If the object radiates the surroundings more than the surroundings radiates the object, the temperature of the objects reduces beneath that of the surroundings and vice versa. The *energy flux* of a grey body can, simplified, be described as (if the absorption coefficient are equal for both surfaces)

$$net\ energy\ flux = \frac{\mathrm{q_{netto}}}{A}\ \alpha\ \sigma\left(T^4 - {T_0}^4\right) \qquad \textit{2-19}$$

2.3.1.2 Planck's Law

The adiabatic flame temperature of propane and methane are 2267 K and 2226 K, respectively. Even though flames can be treated as grey object, it is observable from Figure 2-13 that λ_{max} remains the same for a distribution of a blackbody and a distribution of a grey body with same temperatures. This observation is also confirmed with the relation of equations 2-17 and 2-20, 2-21 and 2-18 which shows that the emissivity only changes the magnitude of the radiation distribution, not the wavelength of the distribution's maxima on the x-axis.

From Planck's law the spectral radiance of the wavelength as a function of temperature can be calculated:

$$F(\lambda, T) = \frac{2\pi hc^2}{\lambda^5} \frac{1}{e^{\frac{hc}{\lambda k_B T}} - 1} \qquad \textit{2-20}$$

Where *F* is the spectral radiance from a circle ($W/m^2\mu m$), λ is the wavelength, *c* – speed of light, *h* – Planck's constant, k_B – Boltzmann's constant, *T* – absolute temperature. It is possible to calculate the emitted radiation from a black body at the temperature *T* when in thermal equilibrium. From equation 2-21, it is possible to find the energy density distribution for a black body at a certain absolute

temperature with respect to wavelength. By integration of equation 2-21, over all wavelengths the total energy emitted is proportional to the Stefan-Boltzmann's law (equation 2-17).

$$u(T) = \frac{4\pi}{c} F(\lambda, T) \qquad 2\text{-}21$$

When assessing two black bodies of different absolute temperatures, say ambient room temperature about 300K and an adiabatic flame temperature about 2300K. With equation 2-21, one achieves the graph in Figure 2-13. As seen on the figure, the dominating wavelength shifts into shorter waves when the temperature increases.

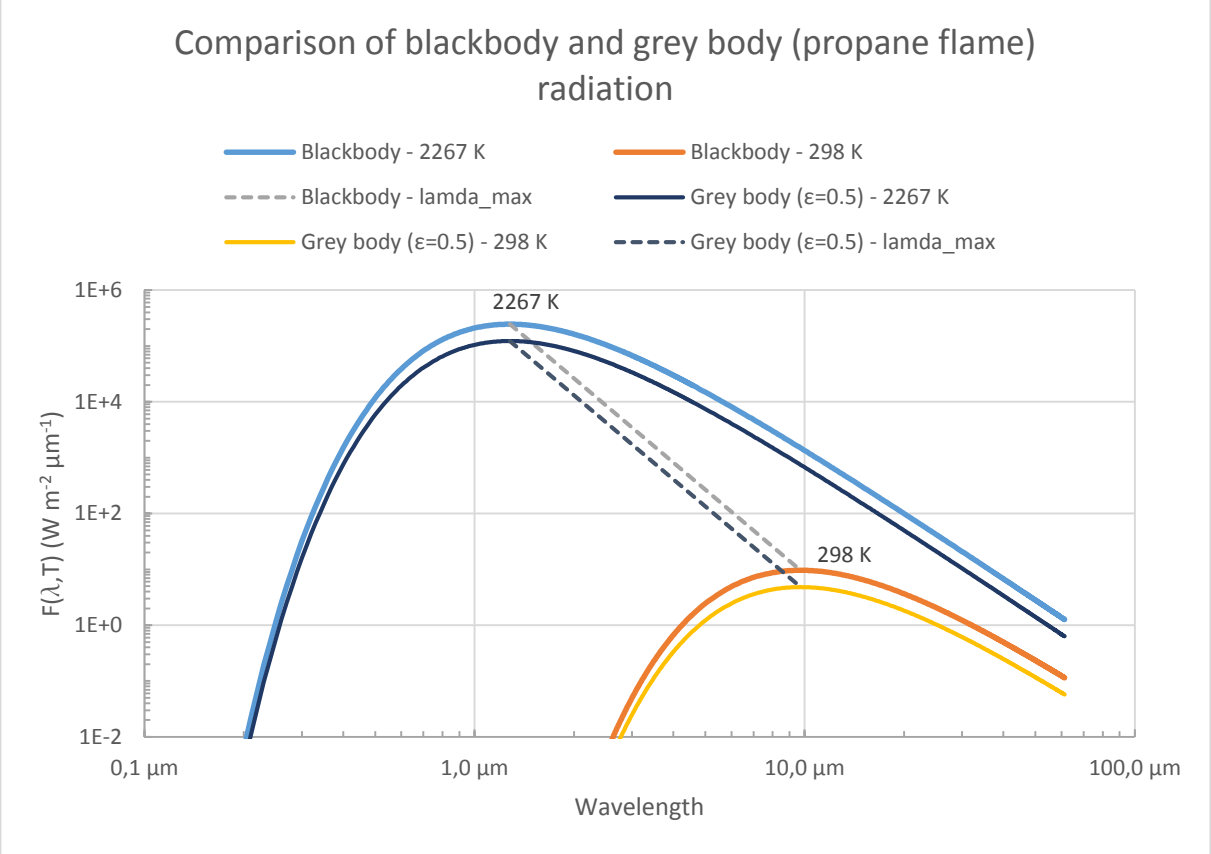

Figure 2-13: Comparison of blackbody and grey body radiation.

From derivation of the energy density function (equation 2-21) with respect to wavelength, it is possible to a correlation between the dominating wavelength and the temperature. This is the *Wien's Law of Displacement*. A sufficient simplification of the law is often given as

$$\lambda_{max} T = 2{,}898 \cdot 10^{-3} m\, K \qquad 2\text{-}22$$

Below are the results from Wien's Law of Displacement with respect to the adiabatic flame temperature and ambient air temperature. λ_{max}

Table 2-5: Radiative properties of air with ambient temperature and a flame with adiabatic temperature

Wien's Law of Displacement for grey body		
	$T_{ad,f} = 2267K$	$T_{ambient} = 298K$
$\boldsymbol{\lambda_{max}}$ (μm)	1,28	9,72
Radiation Class	NIR, IR-A	MIR, IR-C
Maximum Energy Density (W/m^{2}μm)	$1{,}23\ x\ 10^5$	4,81

It is very difficult to describe the radiative properties of surfaces on real bodies. Parameters affecting the radiation are the surface roughness, the reflectivity, the non-uniformity of the surfaces, etc. A *grey body* is defined such that the *monochromatic emissivity*, ε_λ, of the body is independent of wavelength. The monochromatic emissivity is defined as the ratio of the monochromatic emissive power of the body to the monochromatic emissive power of a blackbody at the same wavelength and temperature.[21]

$$\epsilon_\lambda = \frac{q_\lambda}{q_{b\lambda}} \qquad \textit{2-23}$$

According to Holman, 2010, the total emissivity of the body may be related to the monochromatic emissivity by noting that

$E = \int_0^\infty \epsilon_\lambda q_{b\lambda}\, d\lambda$ and $E_b = \int_0^\infty q_{b\lambda}\, d\lambda = \sigma T^4$

so that

$$\epsilon = \frac{E}{E_b} = \frac{\int_0^\infty \epsilon_\lambda q_{b\lambda}\, d\lambda}{\sigma T^4} = \epsilon_\lambda \qquad \textit{2-24}$$

Where E is the total emissivity of a grey body and E_b is the total emissivity of a black body.

For analysis purposes surfaces are usually considered as gray bodies, with emissivities takes as the integrated average value.[21]

View factor is defined as the fraction of radiation/energy leaving the surface of the radiator that hits the radiated surface.

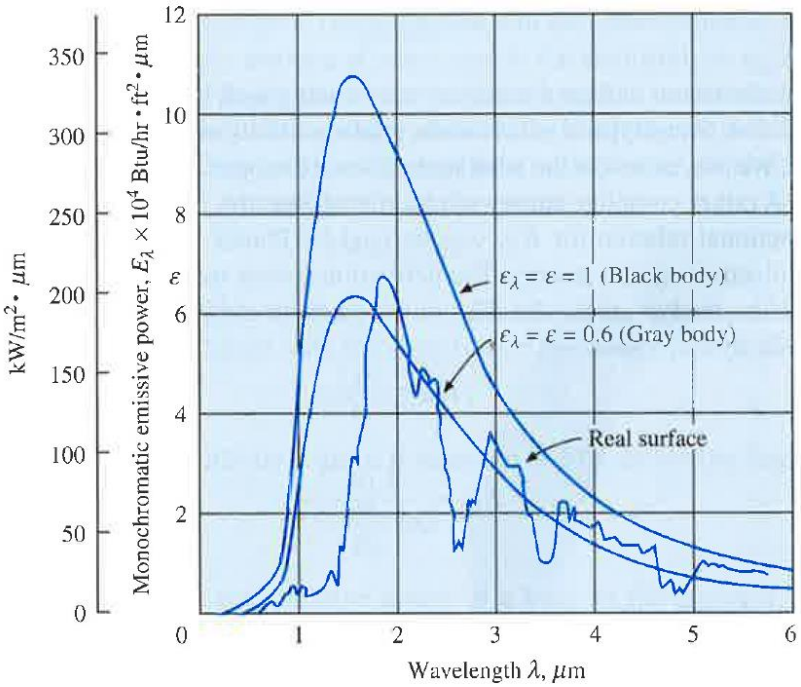

Figure 2-14: Comparison of blackbody, grey body and realistic body[21].

Thermal Radiation net Intensity described as

$$I = F\sigma\varepsilon(T^4 - T_0^4) \qquad 2\text{-}25$$

where I – intensity (W/m^2), F – view factor, σ – Stefan-Boltzmann's constant, ε – emissivity constant, T – absolute temperature of radiating body, T_0 – absolute temperature of absorbing/receiving body. The equation describes the net heat flux a body with temperature T radiates another body with a lower temperature T_0. The bodies' geometries and the special relation with respect to each other is taken into account through the view factor. Since flames can be regarded as grey bodies, the emissivity factor is also taken into account.

2.3.2 Gas flames

Radiation from flames is a complex subject. Giorgio Zizak [22] have a following description of the problem:

"*It is hardly possible to give a description of the spontaneous emission of flames that will be valid generally because the radiation is not only sensitive to temperature, varying with wavelength and the kind of gas mixture, but also depends on many other factors which include the gas/air or gas/oxygen mixture ration, the gas purity, the burner type, the gas flow (laminar or turbulent), the presence of sprayed additives and the height of the observed flame"[22].*

Gas flames emit thermal radiation over a wide specter, from UV and deeply into IR, as shown in

. In the UV spectrum, flames have characteristic spikes in the intensity distribution at various known wavelength. It is put a lot of time and energy into the study of characteristics of flames emissions, starting in the 1800sDuring the years, one has found out that in the combustion reactions intermediate excited ions or atom, called *radicals*, occurs in the flames. These radicals has characteristic features when looking into the emission distribution with respect to wavelength. One can pinpoint spikes in the intensity. This is where the radicals emits radiation. The most known radicals in a flame are listed in Table 2-6.

Table 2-6: Radicals with characteristic wavelength[9]

Radicals	**Characteristic wavelength**
OH	306-315 nm
CH*	390, 431 nm
C_2*	469-473, 510-516

2.4 Detection and Measurements of flames

2.4.1 PIN photodiode

PIN diodes consists of three layers, P-layer, I-layer and N-layer, hence the name. The P-layer works as an anode and the P-layer as a cathode. The I-layer divides the two other layers and works as a depletion region. When scintillating photons reaches the I-layer with sufficient energy, electrons from the atomic structure of the depletion region releases electrons creating a free electron and an empty space within the atom (called hole). Thus, the atom is positive charged (marked with "+" in the figure) and the electron is negatively charged by nature ("-"). The electron-hole pair may be pulled away from the I-layer by an external field resulting in change of current through the photodiode, hence, producing photocurrent. PN photodiodes has large capacitance due the interface between the P- and the N-layer, this effect is significantly reduced due to the I-layer in PIN-photodiodes. When the PIN-photodiode is not exposed to photons with a high enough energy, the natural electron interactions within a substance create something called black current which is a background current or natural current through the photodiode.

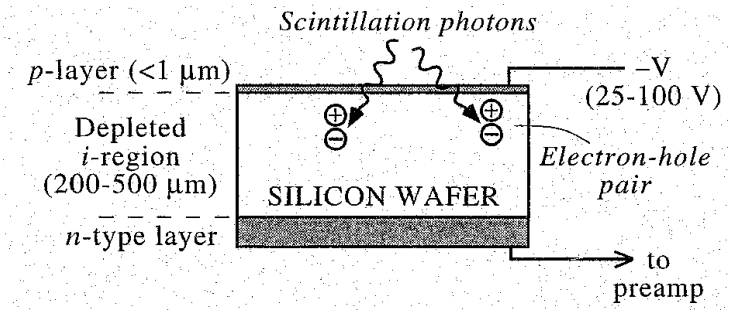

Figure 2-15: Example of PIN photodiode structure[23].

The figure above is of a silicon PIN photodiode, Knoll et al.[23] displayed the spectral response of a typical photodiode in Figure 2-16.

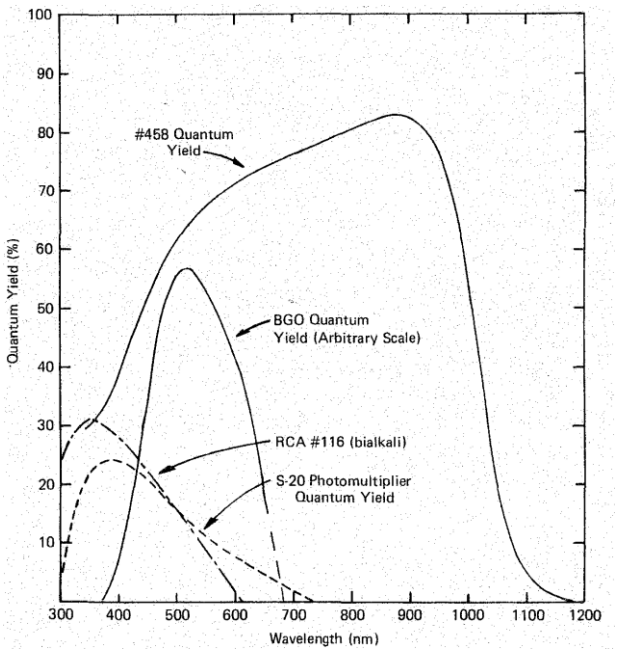

Figure 2-16: Comparison of quantum efficiency of a silicon photodiode (#458) with other photoelectric equipment. [23]

Dark current is one of the contributors to the noise, its contribution and the overall noise figure can be reduced by cooling the photodiode, (Figure 2-17). The rapid rise in dark current above room temperature has generally prevented the use of silicon photodiodes in applications requiring operation at elevated temperatures. The affect the temperature have on the photodiode can be reduced when applied to detection of flame fronts in gas explosion due to two parameters. Firstly, the photodiode can be placed inside a casing, protecting it. Secondly, the time frame of high temperature exposure is quite low, hence, the elevated temperature of the casing protecting the photodiode, due to the exposure, is most probably negligible.

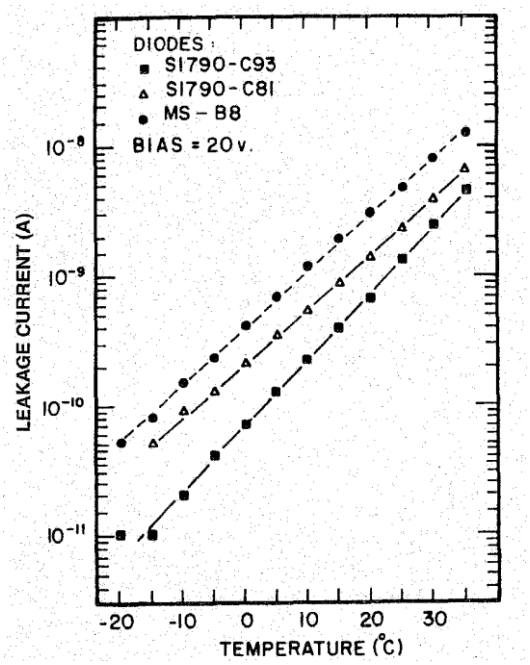

Figure 2-17: Temperature dependencies of leakage current for some type of silicon photodiodes. [23]

2.5 Previous Work

2.5.1 Previous work on photodiode as flame front detectors

Many experiments of different scales with photodiodes tracking or detecting flame fronts have been carried out during the last 30 years. In that time, photodiodes have become less costly and more accurate due to technology development.

Due to the short response time of photodiodes, it is possible to use them over a wide range of high flame velocities, from deflagration velocities of a few hundred meters per second to detonation velocities of almost 2000 meters per second (1800 m/s for both propane and methane).

The photodiodes react on thermal radiation, making the technology applicable also for dust explosion. Conti and Cashdollar et al. [24] developed a probe which could measure the density of dust clouds and register the presence of a flame without the probe reaching saturation. The probe was tested in both small-scale experiments in an 8 liter closed vessel and in full-scale explosions in a mine . The probe monitored the density of the dust cloud based on the principle of light attenuation and was fitted with gallium-arsenide LED, which emitted NIR radiation of 950 ± 50nm, and a silicon photodiode with optical interference filter with centerline at 950nm and bandwidth equal 50nm. To avoid saturation when the flame passes by, an optical filter was fitted to the photodiode. The probe was also fitted with an air flushing system in order to prevent dust from settling on the diodes. Figure 2-18 shows the design of the probe.

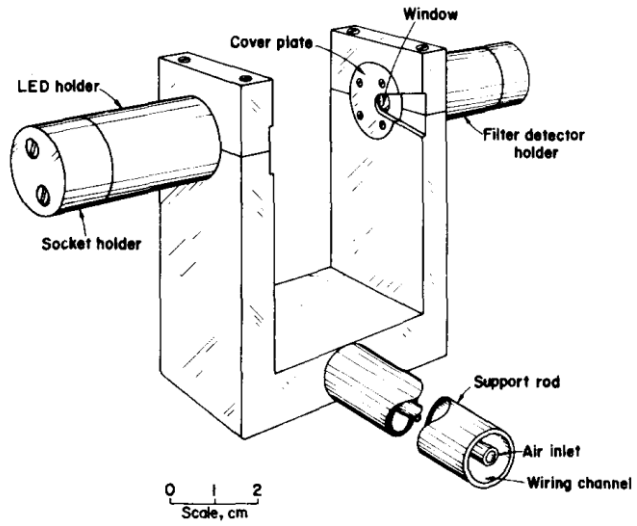

Figure 2-18: Optical dust probe developed by Conti et al.[24].

Figure 2-19 shows measurements from a dust probe during a dust explosion in the 8 liter vessel. After the ignition of the dispersed dust, radiation from the flame increased the probe signal according to the signal output.

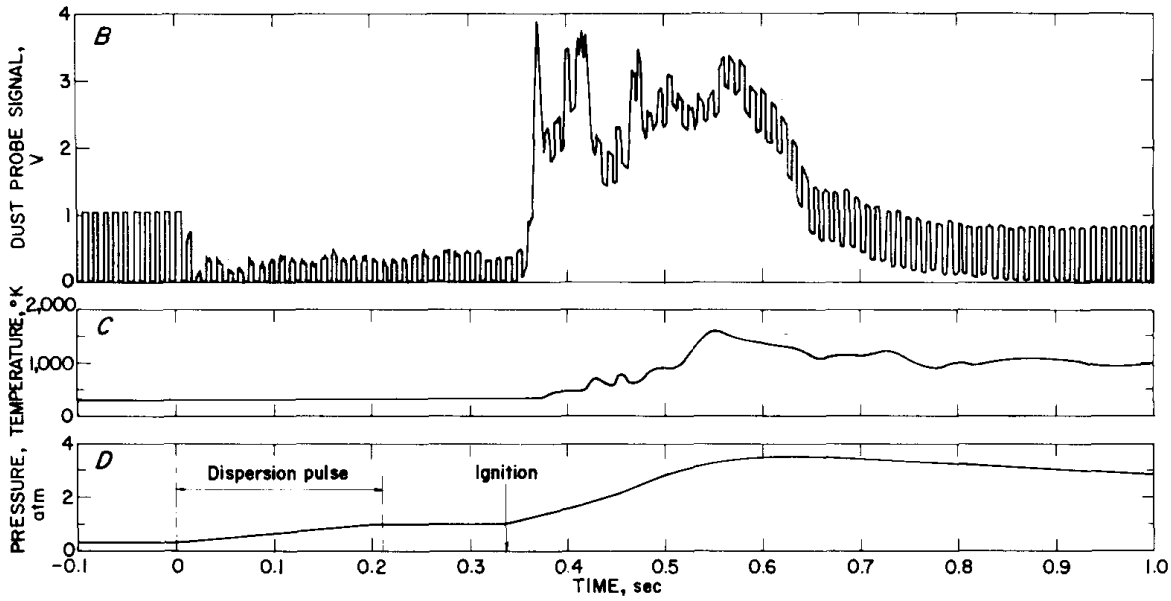

Figure 2-19: Dust explosion measurements, Dust probe signal output on top. [24]

The output signal from the probe is decreased after the initiation of dust dispersion due to absorption before it leaps after ignition of dust cloud. Conti and Cashdollar et al. [24] made foundation for further works.

Eckhoff, Fuhre and Pedersen [25], carried out experiments studying the influence of dust concentrations and location of ignition point on flame propagation and pressure development, through a series of vented maize starch explosions in a 236 m^3 steel silo. The silo was cylindrical with height of 22m and a 3.7m diameter with numerous threaded holes permitting diagnostic probes to be mounted at desired levels.

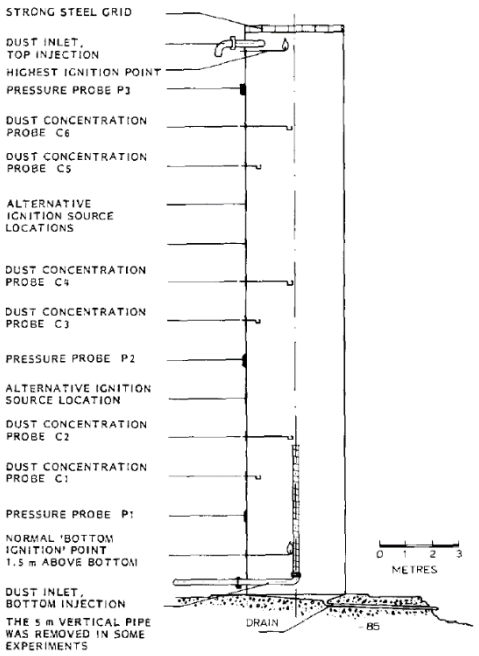

Figure 2-20 A vertical section of the 236m3 steel silo [25].

For flame arrival measurements, photodiodes could be mounted at up to six different locations as shown in Figure 2-18. Three probes 0.5m from the silo wall and three probes 1.5m from the wall. Figure 2-21 shows the vertical displacement of flame front as a function of time after ignition at 1.5m above silo bottom. The highest vertical flames speed measured during the experiments were recorded to more than 100 m/s.

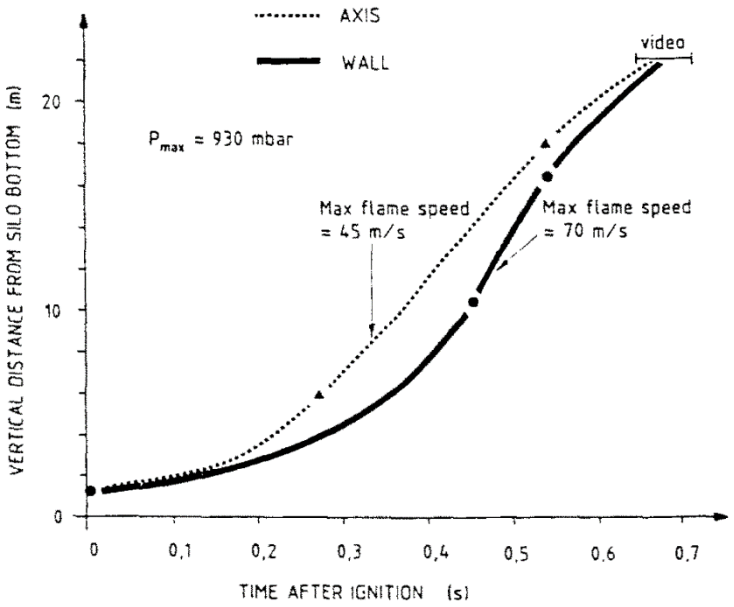

Figure 2-21: Vertical displacement of flame front as a function of time after ignition at 1.5m above silo bottom[25].

The highest vertical flames speed measured during the experiments were recorded to more than 100 m/s.

Kalvatn et al. [26] studied further development from the idea of Conti and Cashdollar et al. [24] by detecting both flame front and measure dust cloud concentration by light attenuation with Beer's. The flame front was detected when the signal from the PDs was saturated.

Lu, Guo, Li, Fan, Zhang, Yang, and Wang et al. [27] studied the propagation of methane-air flame and its interaction with a coal dust deposit. A horizontal flame-acceleration tube, 148x8.9x8.9cm square crossed, was used for the experimental purposes. A digital video camera, 25 fps, and photodiodes were used to detect the propagation of the flame front. The tube was pumped down to a given vacuum prior the filling of premixed methane/air mixture. The experimental setup is shown in Figure 2-22.

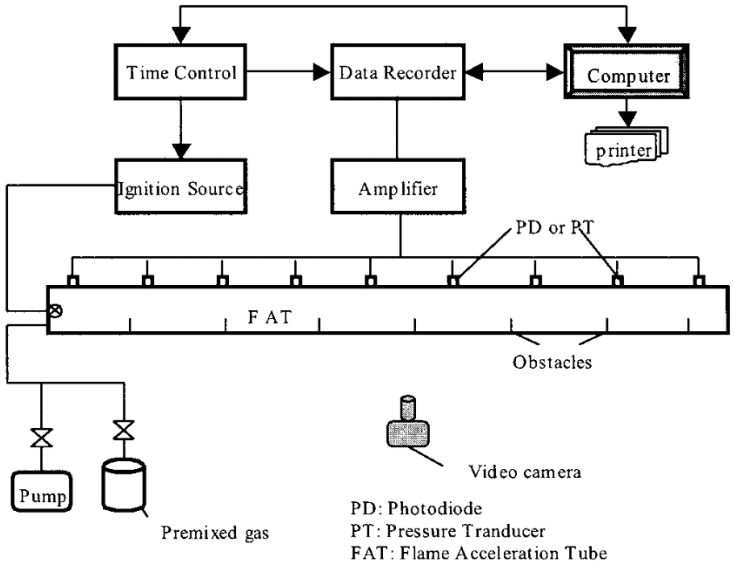

Figure 2-22: The applied experimental setup[27].

Propagation of the flame front and how it interact with the dust were observed through the glass wall of the FAT, with PDs mounted on back wall. Flame front propagation is illustrated in Figure 2-23. It was found that the terminal flame speed in a tube with obstacles with a blockage ratio BR = 0.05 was about four times greater than in the same tube without obstacles. For BR = 0.10, terminal flame speed was 16 times greater.

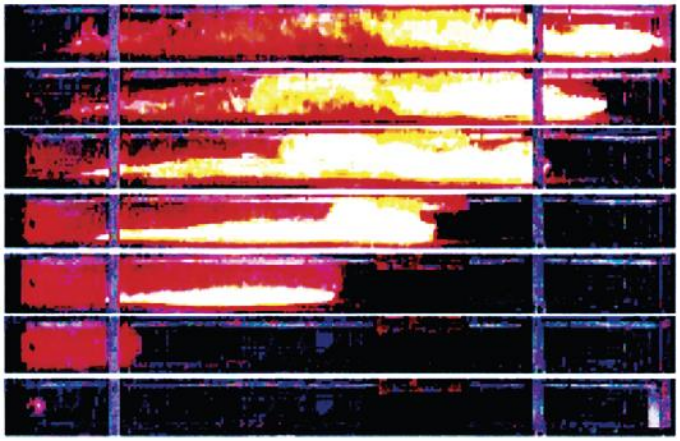

Figure 2-23: Flame front propagation recorded with 25 fps[27].

Bauer et al. [28] used photodiodes to investigate the performance of flame/detonation arresters regarding safety in the process industry. The experiments were carried out in a 3 meter long tube with inner diameter of 28mm. The arrester consisted of 2mm inner diameter tubing arranged in a specific geometry, and were placed in the mid of the tube representing BR=0.20. A premixed gas mixture was fed to the tube and a 150 J igniter of black powder ignited the mixture. Photodiodes were coupled separately to optical probes via optical fiber and measured the flame front velocities. Due to the low temperatures, the photodiodes operated in the IR range in order to record the low emissivities. Figure 2-24 shows the experimental setup used by Bauer.

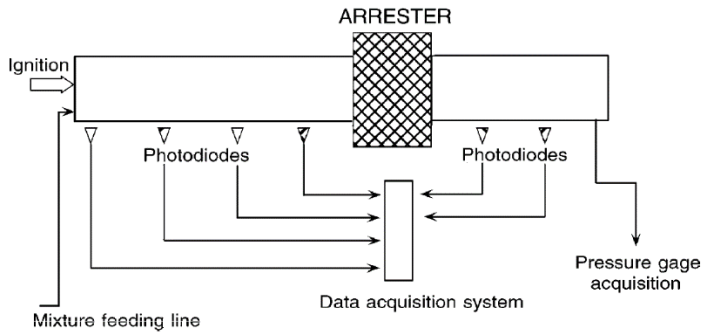

Figure 2-24: Experimental setup for testing flame/detonation arrester[28].

As mentioned in start of this section, photodiode technology has become more affordable decades. Airas, Torres, Sbarbaro and Farias [9] designed a low-cost silicon photodiode based sensor to analyze the formation and behavior of excited CH* and C_2* radicals in the combustion process of oil and gas, by sensing the spectral emission of hydrocarbon flames. They tried to demonstrate the use of photodiode based sensor for flame sensing and combustion process monitoring through spectral detection. Two silicon photodiode assembled with separate filters were used giving required sensitivity of the characteristic wavelength of CH* and C_2* at 430nm and 514.5, respectively, as shown in Figure 2-25

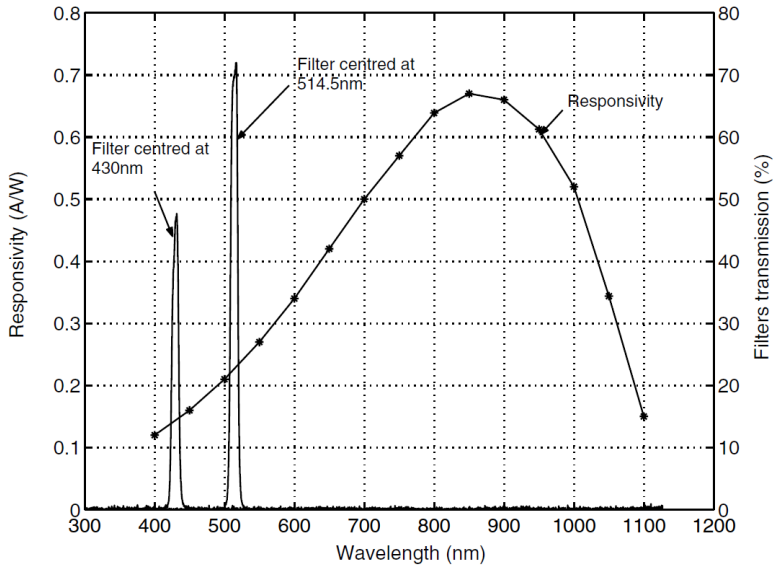

Figure 2-25: Responsitivity of silicon photodiodes and transmission of filters with respect to wavelength. [9]

Babkin, Korzhavin and Bunev [29] measured velocities of flame propagation for methane/air and propane/air mixtures in four porous medium under initial pressures from 0.06 to 2.5 MPa and fuel-air ratios of 0.7 to 1.65. The velocity measurements were performed by using photodiodes in tubes of 0.96, 1.44, 1.92 and 2.88m lengths with 48x48mm squared cross section, that were filled with porous medium. The tubes were filled with premixed propane/air or methane/air mixtures prior to ignition. A pressure transducer tracked the pressure development during experiments. Figure 2-26 shows the experimental setup used by Babkin et al.

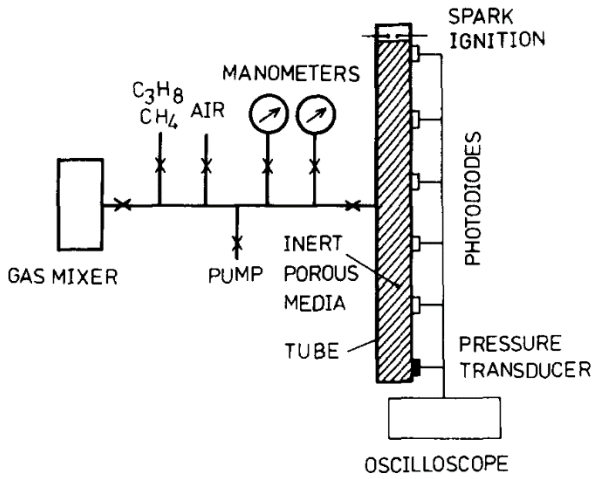

Figure 2-26: Experimental setup used by Babkin et al. [29].

Dependencies of flame propagation speed and laminar burning velocities with respect to fuel-air ratio in methane/air and propane/air mixtures were found in the experiments performed by Babkin et al. as shown in Figure 2-27.

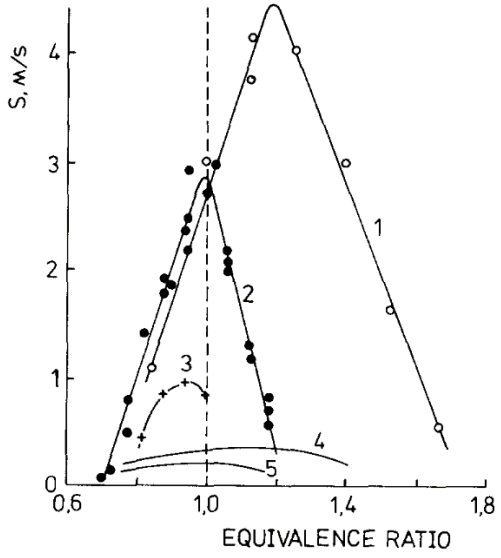

Figure 2-27: Dependencies of flame speed in porous media (1-3) and burning velocities (4,5) for air mixtures of propane and methane, respectively[29].

Due to their high responsitivity, photodiodes are also capable of detecting flame fronts of detonations. Dorofeev et al. [30] carried out large-scale experiments on turbulent flame propagation and DDT in a confined volume of lean hydrogen/air mixtures, in a strong 480m^3 enclosure with length of 69.9m. The experimental volume consists of three parts as shown in Figure 2-28. First part were a 34.6x.2.3x2.5 m channel, second part was called a canyon with the dimensions 10.55x6.3x2.5m. Hydrogen was added

and continuously mixed with the air with three fans, gas sampling were taken from three different points with a 0.1% accuracy.

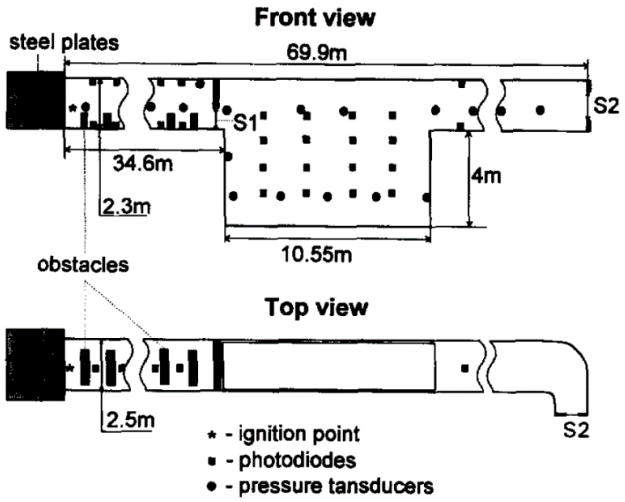

Figure 2-28: Experimental setup for DDT [30].

Four photodiodes were placed in the second part of the channel, 16 in the canyon and twenty along first part of the enclosure (left in Figure 2-28). The pressure was measured with Kistler 7031 and 701 piezoelectric pressure transducers, and PCB 113H.

The photodiodes were used to determine the position of the flame front in the channel and to determine the shape of the flame front based on the arrival time data by using a simple mathematical method, see Figure 2-29.

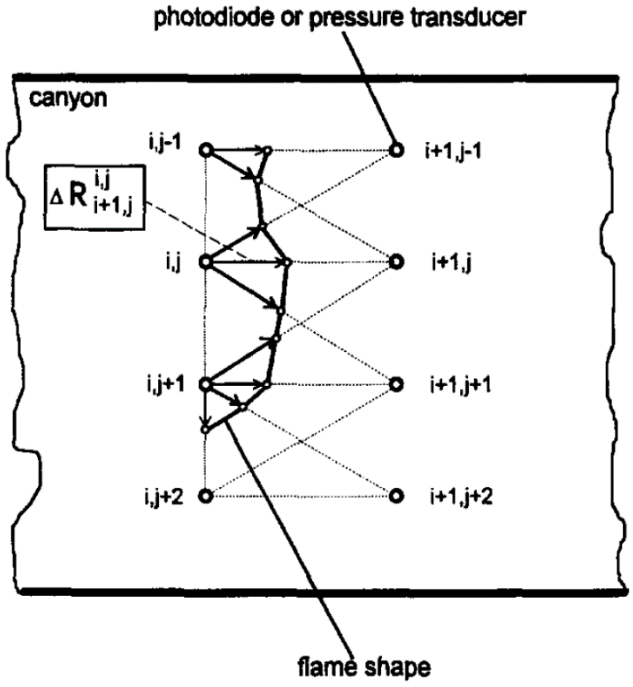

Figure 2-29: Flame front shape determination from arrival time data experiments performed by Dorofeev et al. [30].

Haloua et al. [31], used two photodiodes and their difference in analogue signal output to measure the flame front position of the detonation in 25.3m long tube with 38mm inner diameter. Two piezoelectric pressure transducers were fitted, for pressure measurements. Figure 2-30 shows the experimental setup.

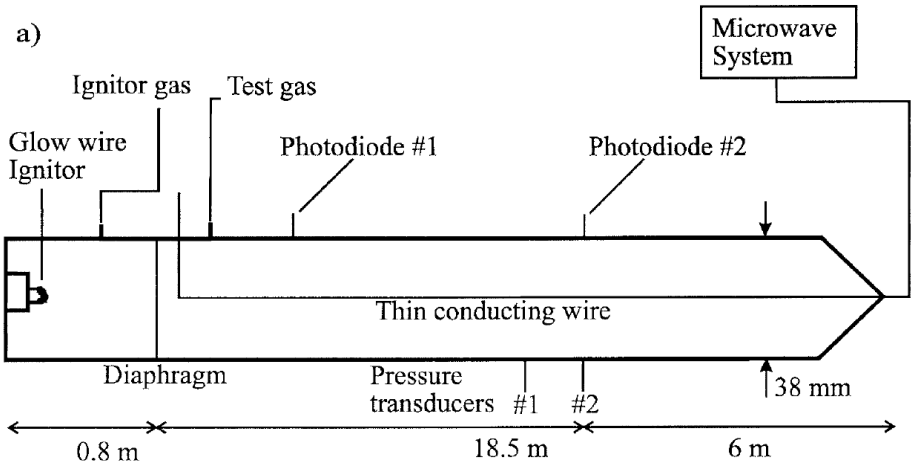

Figure 2-30: An experimental arrangement of a detonation tube [31].

2.5.2 Previous work on turbulent premixed explosions in the MOGELEG channel

Pedersen [32] studied the influence of fuel-air ratio on flame speed and overpressure in a premixed propane/air explosion in two geometrically similar vented channels of different scales. The lab-scale channel called the MOGELEG channel measured 150x30x30cm squared cross section, , the medium-scale rig measured 6.0x1.2x1.2m. The velocity was measured using video footage from a Phantom v210 HS camera configured with 5000fps. Figure 2-31 shows pressure-time histories and flame speeds from the small-scale experiments with different fuel-air ratios. Figure 2-31 shows pressure-time histories and flame speeds from the small-scale experiments with different fuel-air ratios.

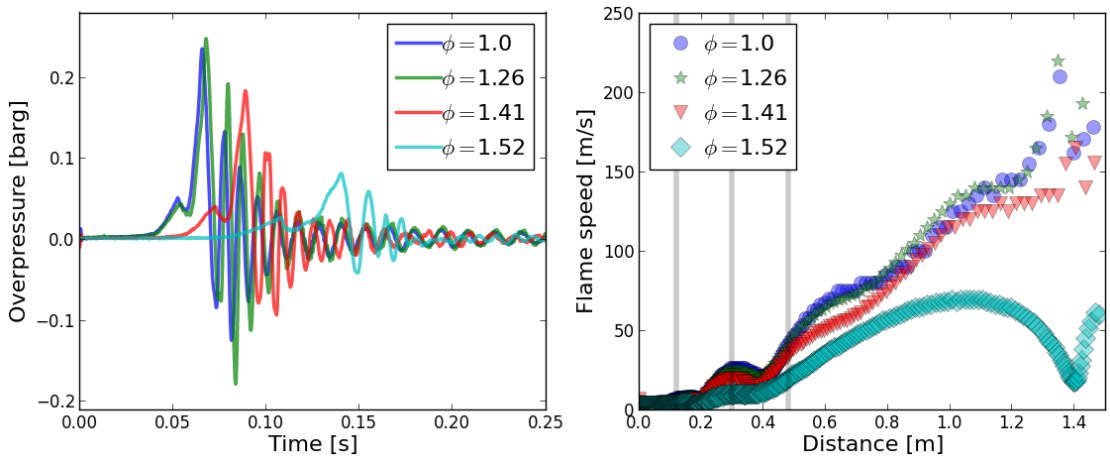

Figure 2-31: Pressure-time curves (left) and flame speeds (right) form the small-scale experiments with respective fuel-air ratios. Vertical lines in flame speed graph represents obstacle locations[32].

Clear video footage was available due to the HS Camera's resolution and fps configuration, giving possibility for accurate velocity measurements. The velocity measurements were calculated by an in-house programmed VI in LabVIEW, which identified the flame front through a series of frames from video footage and scaling. Figure 2-31 shows footage from the HS camera during an explosion experiment performed by Pedersen in the MOGELEG channel with fuel-air ratio of 1.4.

Figure 2-32: Explosion experiment in MOGELEG channel with fuel-air ration equal 1.4[32].

3 Experiments

This chapter describes the experimental equipment, the experimental setup and procedures as well as the aim for the different parts of the experiments.

The experiments mainly focus on the accuracy of flame front detection using photodiodes compared with HS recordings of the experiments. The experimental approach is based on previous work carried out by [9, 25-27, 30, 32], using two different types of flame detectors based on photodiodes.

In total nine test series were conducted, eight in small-scale and one in large-scale. As Table 3-1 indicates, the test series had five digits numbers (0000x). The respective tests had three digits numbers (0xx).

The conducted tests can be divided into three different sections. Preliminary tests where the behavior and properties of the photodiodes are tested. Secondly, optimizing the angled sight detector with respect to flame arrival with/without added reflection. Thirdly, large-scale testing of the third generation detectors.

Table 3-1: Overview of the experimental test series

Test series #	Test conditions and recordings	Numbers of tests	Types of tests
00001	Recordings: • HS video: Camera: Casio Elixim 600fps Test conditions • Empty MOGELEG channel • Gas: methane	20	Preliminary
00002	Recordings: (yields for test series 00002 - 00005) • Pressure data recorded • HS Camera: Phantom V210 HS 3000fps Test conditions • Empty MOGELEG channel • Gas: methane	11	
00003	• Obstructed MOGLEG channel (BR = 0.05) • Gas: methane	6	
00004	• Obstructed MOGLEG channel (BR = 0,20) • Gas: methane	7	
00005	• Obstructed MOGLEG channel (BR = 0,20) • Reflective surface added • plastic releasing system added • Gas: methane and propane	6	Optimizing
00006	Recordings: (yields for test series 00006 - 00008) • Pressure data recorded • HS Camera: Phantom V210 HS 5000fps Test conditions • Obstructed MOGLEG channel (BR = 0,20) • Sensitivity adjusted for optimization • Gas: propane	9	
00007	• Obstructed MOGLEG channel (BR = 0,20) • Optimizing FD4's slit configuration • Gas: propane	16	
00008	• New generation of detectors tested in Obstructed MOGLEG channel (BR = 0,20) o One PD based detector -> Two PD based detector o One angled detector -> Combined two angled detector • With/without reflection • Gas: propane	5	Large-scale
00009	Recordings: • Pressure data recorded • HS Camera: Edgertronic 2000fps Test conditions • Testing in 50 m^3 downscaled Gullfaks A compressor module • Gas: propane Test conditions and recordings	19	

3.1 Photodiodes

Photodiodes (PDs) with sensitivity within the NIR area were chosen on the basis of general and simplified radiation theory and the foundation from previous works. The PDs were delivered by STM Sensors (now STM Balluff). The signal from the amplifiers are a simple on or off state, with adjustable sensitivity (threshold) for positive flame detection. This product consists normally of two parts, one emitter and one receiver (photodiode) as shown in Figure 3-1. Only the photodiodes were used.

Figure 3-1: DLM60 emitter and sensor, 1:1 size.

The photodiode chip inside the receiver (from here on called sensor) has a responsivity peak at 850nm, its responsivity distribution is given in Figure 3-2. The figure also displays the emissive power of a theoretical propane flame with an adiabatic temperature. Table 2-5 shows that the maxima of the emissive power of the propane flame, when regarded as a grey body, is at 1.28µm, sufficiently close to the responsivity maxima of the PDs at 0.85µm. The magnitude of the flame's emissive power at 80% responsivity indicates that the amount of expected thermal radiation form the flame fronts at these conditions should result in a detection. By Wien's displacement law and based on the work performed by Airas et al. [9], flame temperatures of 1500K and above should also be detected.

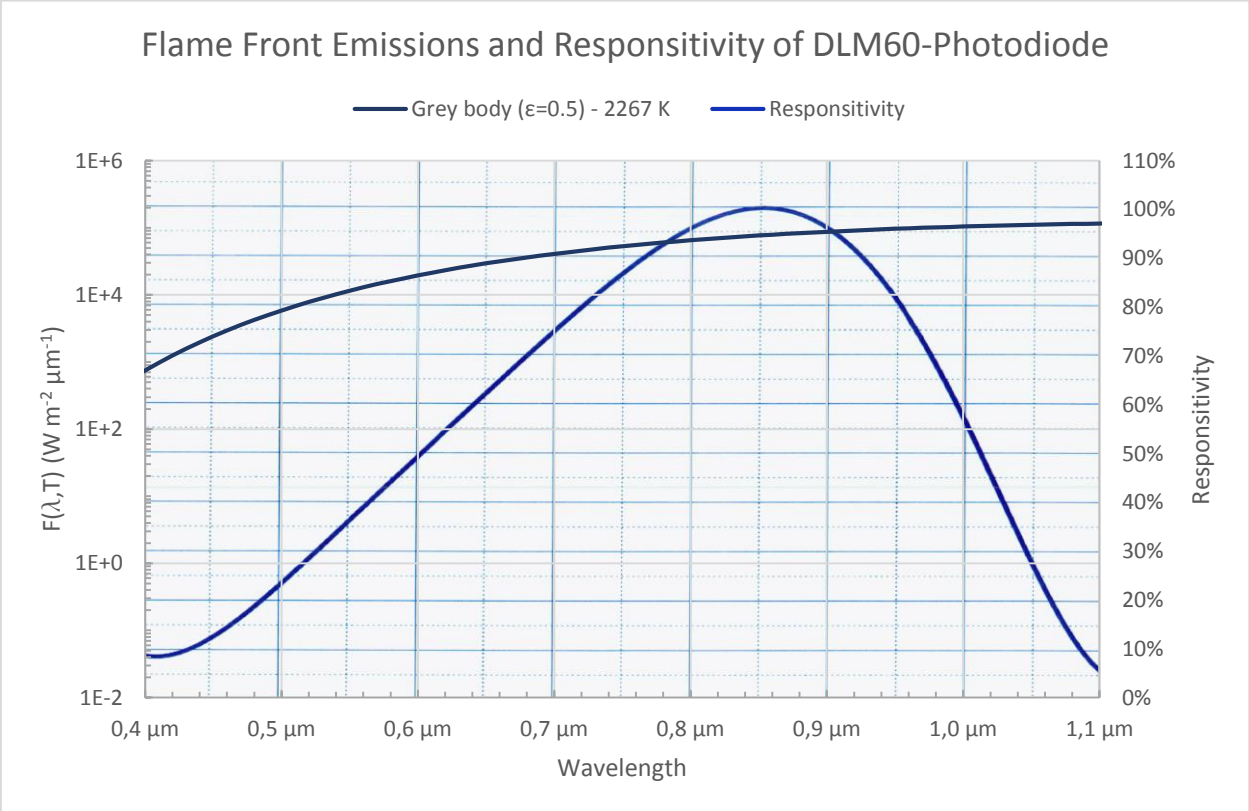

Figure 3-2: Comparison of Flame front emissions and the responsitivity of the DLM60 photodiode.

3.2 Small-scale experiments

The small-scale experiments (preliminary and optimization tests) were conducted at GexCon AS Laboratories at Fantoft, Bergen. A channel referred to as the “MOGELEG channel” with dimensions 150x30x30cm was used.

3.2.1 The MOGELEG channel

The MOGELEG channel, as shown in Figure 3-3. The channel is open in one end. One of the long sides was made of reinforced transparent plastic to make the internal visible. The other long side (back wall) consists of 10mm aluminum, modified with different types of fittings for various equipment.

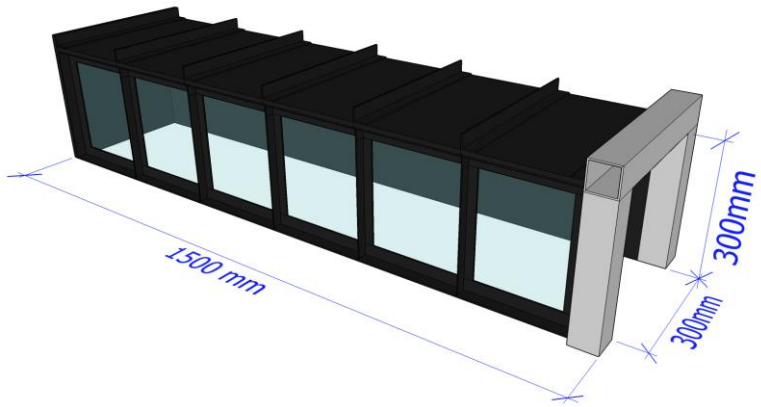

Figure 3-3: The MOGELEG channel.

A re-circulation system was used for mixing gas and an electrical spark at the closed end served as an ignition source. Prior to mixing the gas a thin plastic sheet was mounted on the open end, allowing the gas to be prepared in the test volume. A pneumatic plastic release system was added to the open end of the channel to ensure effective venting. The experimental setup and procedures are described in detail in section 3.2.6.

A gas pump sucks gas from the mixture and a gas analyzer measures the gas concentration in the air of the circulation stream.

The valves mentioned in Table 3-2 and the fan running the circulation, are connected to a valve and fan interface (see Appendix A). This allows remote operation of the test apparatus.

A pneumatic plastic releasing system was added to the experimental channel due to undesirable pressure developments, which counteracts the grade of repeatability of the tests.

Obstructions could be mounted inside the channel, generating turbulence in the explosion induced flow.

3.2.2 Angled sight flame detector

A geometry with slit configurations was mounted onto one of the sensors, giving it an approximated plane angled view. The detector has a 60° vertical vision through a 2mm wide slit as shown in Figure 3-7. The purpose of the angled sight detector is to observe a narrow cross section of the channel during the explosion in order to avoid early detection and ensure flame detection as the flame passes by. This configuration reduce the probability for the flame front to propagate past the detector before detection, compared to the line-of-sight detectors described in section 0. The geometry was designed using Google SketchUp and constructed at the workshop at IFT.

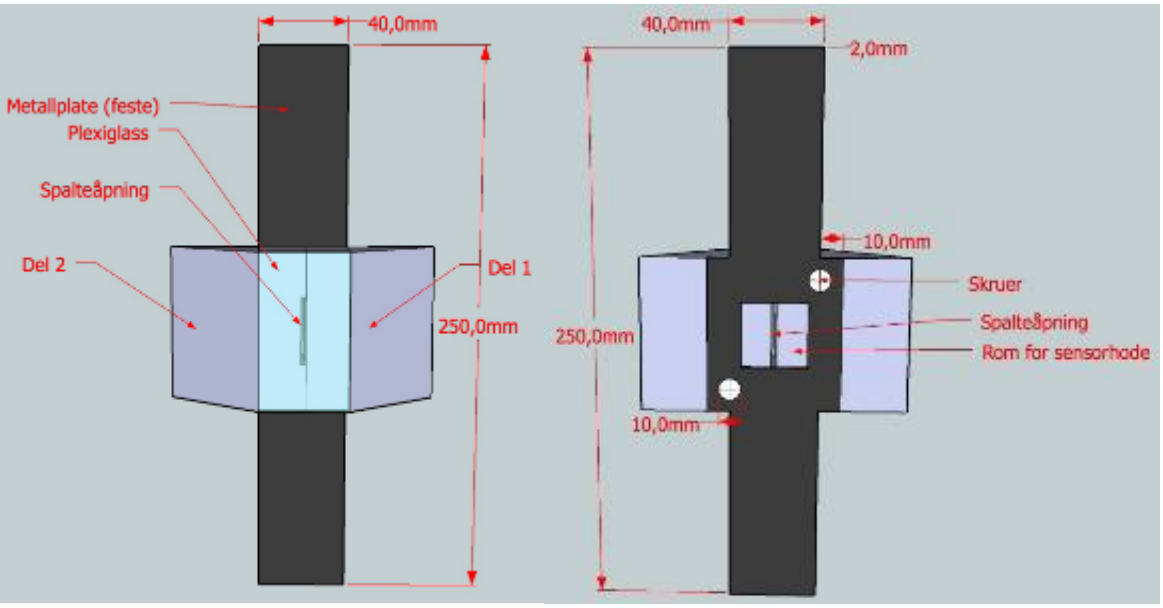

Figure 3-4 The Angled Detection Principle – Front and back.

3.2.3 Line-of-sight flame detectors

Three sensors were fitted into three hollowed bolts with BOROFLOAT glass covering the front. This configuration gave the sensors a line of sight. A line-of-sight detector is shown in Figure 3-5. The photodiodes are fitted into the hexagon heads, looking through the hole.

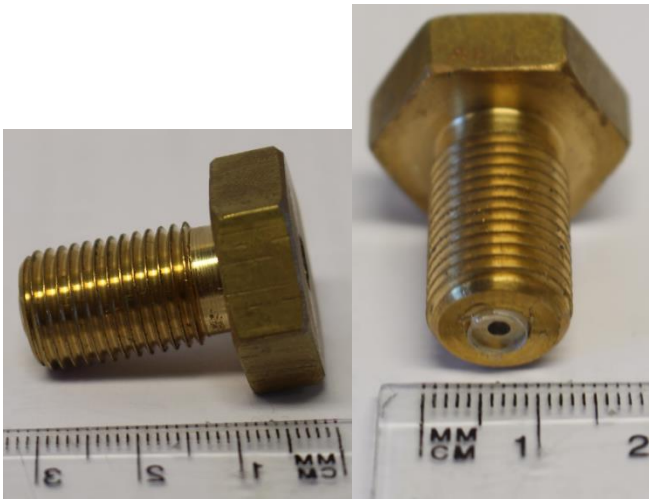

Figure 3-5: A line of sight detector without fitted photodiode.

The hollowed bolts used in the experiments have a BOROFLOAT® glass mounted in front to protect the sensor from heat, soot and pressure impacts. The glasses were 1.75 ±0.2 mm thick with a diameter of 5.0 ±0.5mm with wavelength and transmission percentage of 90%.

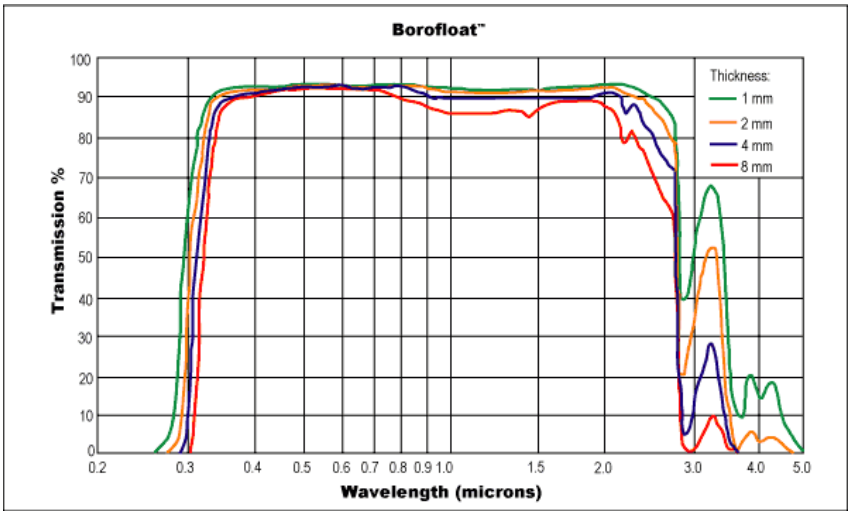

Figure 3-6: Transmissivity for BOROFLOAT® glasses with respect to wavelength (µm) and thickness of glass.

3.2.4 General experiment setup for MOGELEG channel

The MOGELEG channel was fitted with both an angled sight detector and line-of-sight detectors as shown in Figure 3-7. The purpose of the angled sight detector is to achieve more accurate flame detection. The angled sight detector has a larger sensing area than that of the line of sight detector and a narrower sight than that of a regular flame sensor (cone vision). Figure 3-7 shows an illustration of the vision of the angled sight detector and the line of sight detectors in the MOGELEG channel. The purpose of this setup is to test the behavior of the photodiodes, and investigate if FD1, FD2 and FD3 are fast enough to detect the flame front in such a way that they reproduce the flame front curvature as seen in Figure 2-29.

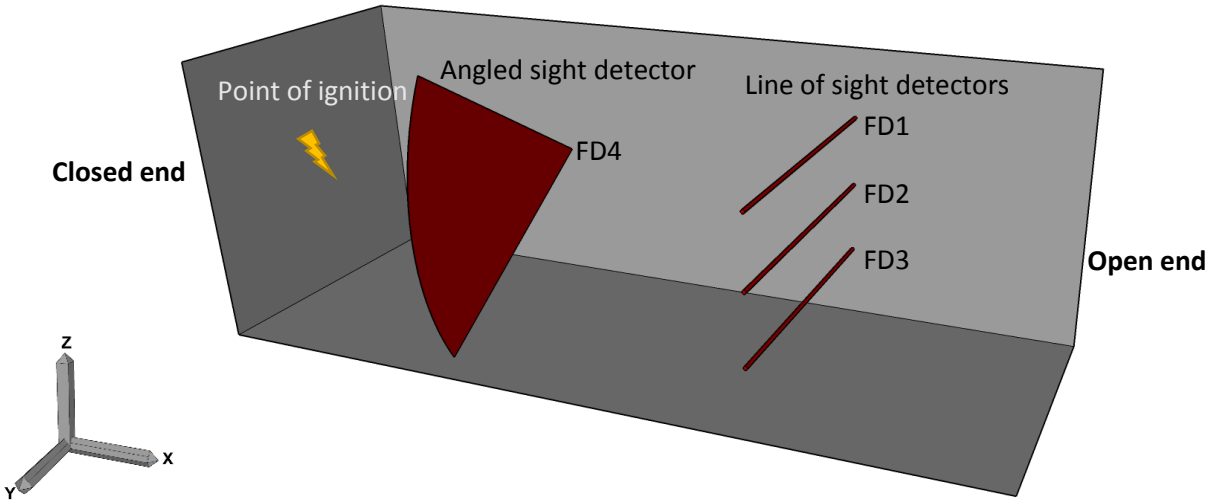

Figure 3-7: Detectors mounted in MOGELEG channel.

Angled sight detector (FD4) was fitted in mid back wall in z-direction and 62.5 centimeters from closed end in x-direction. The line of sight detectors were fitted 114cm from closed end in x-direction, above each other. FD2 was fitted mid back wall with FD1 and FD3 7.5cm above and under, respectively, in z-direction. The two different types of detectors observe in two different xz-planes. The use of this application will also give answer to the behavior of the PDs, especially if FD1, FD2 and FD3 are fast enough to detect the flame front in such a way that it reproduces its curvature as seen in [30].

A high speed (HS) camera was placed 409cm from the angled detector, so that the position of the flame front would be as accurate as possible with respect to this detector. For test series 00001, a Casio Elixim camera was used with 600fps configuration. Prior to test series 00002, this camera was substituted by a Phantom v210 camera with 3000fps with HD quality. Figure 3-8 shows the general experimental setup for test series 00001 through 00005.

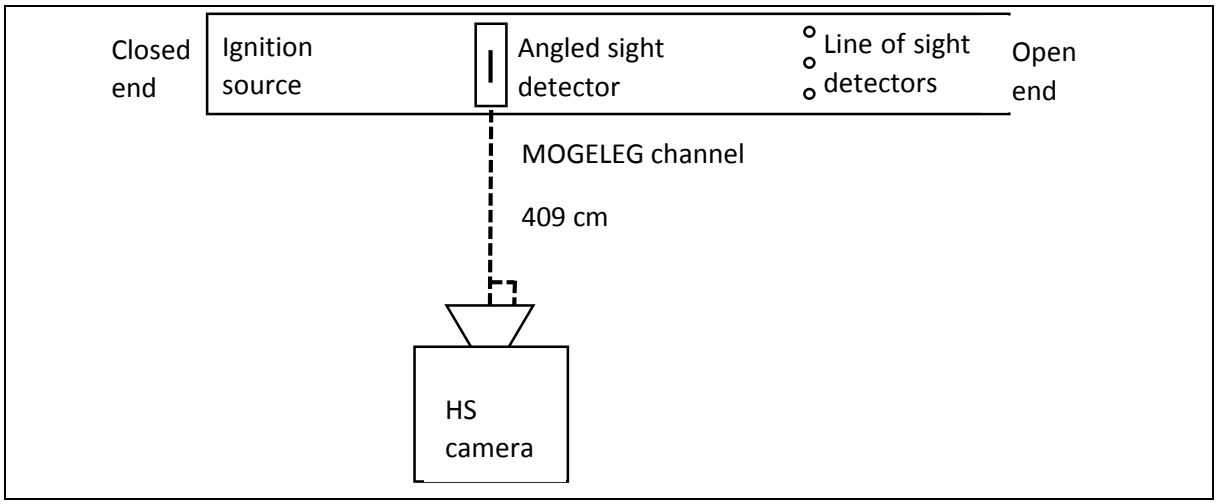

Figure 3-8: the general experimental setup for test series 00001 and 00002.

Figure 3-9 shows when the mixture is ignited during test 001, test series 00004. "A" is a grid of five 30 centimeters long horizontal tubes of 15mm diameter, generating turbulence. "B" is the angled detector (FD4), its slit is marked with a little reflector above it during testing. "C" indicates the positions of the line-of-sight detectors, FD1 through FD3, from top to bottom. The plastic foil is held in position by a wooden frame and three clamps.

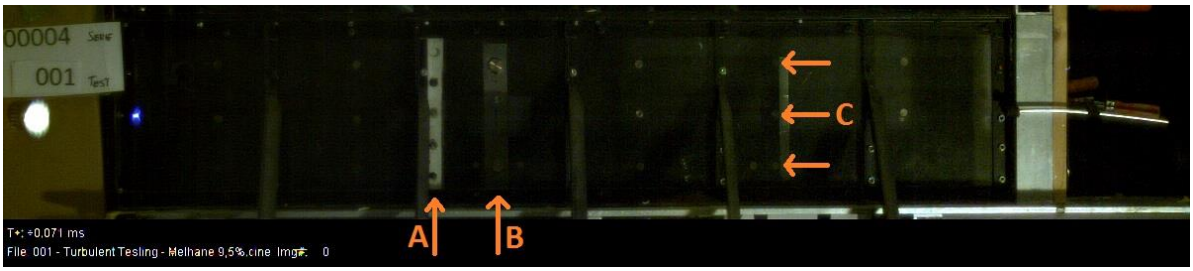

Figure 3-9: Video footage for test 001 of the 00004 test series.

As mentioned earlier, due to the undesired pressure development with the first plastic cover configuration, a pneumatic plastic release system was mounted onto the open end of the MOGELEG channel. Figure 3-10 shows the plastic release system to the right, during an explosion.

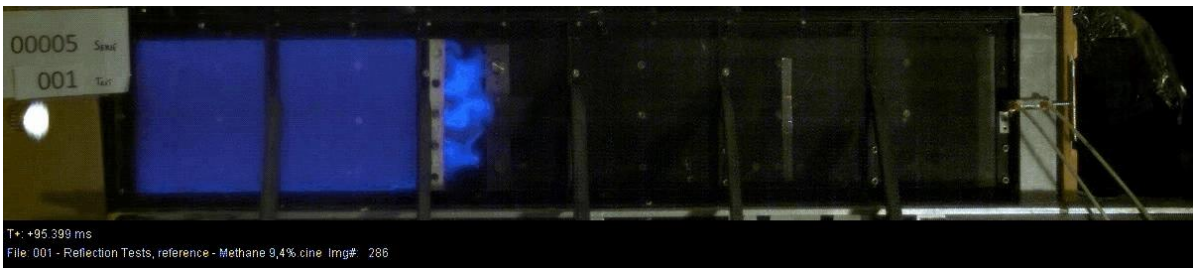

Figure 3-10: Release of the plastic due to explosion pressure. The plastic release system is activated 0.2s before ignition.

The position of the angled sight detector and the line of sight detectors was swapped prior to the test series 00006, as shown in Figure 3-11, to investigate how they would behave in slightly different combustion regimes.

The position of the Phantom V210 HS camera was also changed. However, it remained normal to the angled sight detector. The distance between the HS cameras and the MOGELEG channel was increased since it needed to cover the whole experimental channel, as shown by Figure 3-11.

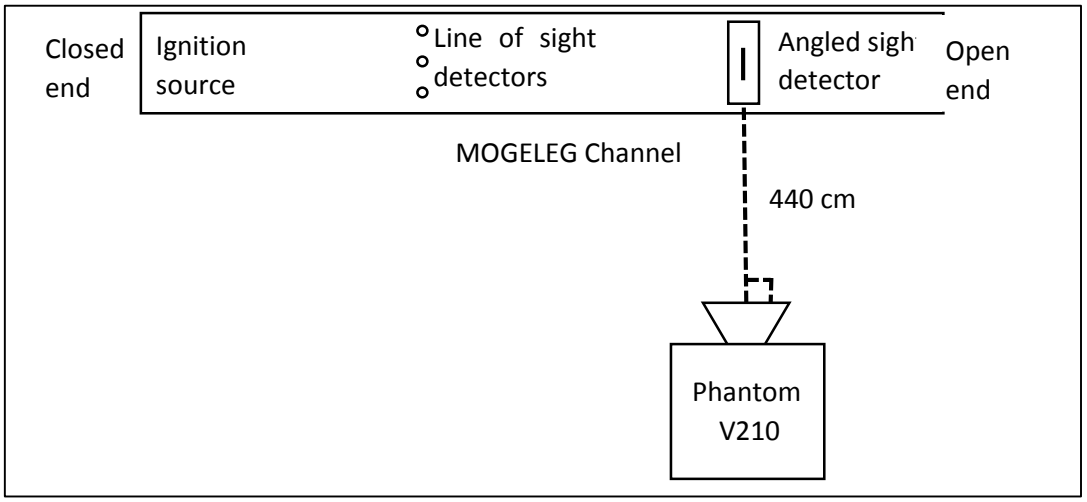

Figure 3-11: Experimental setup for test series 00006 and 00007.

Assuming that the aluminum tape makes the geometry opaque with strong reflectivity. From [19]: "Because incident energy onto an opaque surface is either reflected or absorbed by the surface, it follows that one unit of radiant energy incident on an opaque surface at a given wavelength and from a given direction will have a fraction absorbed and the remainder reflected, or

$$1 = \alpha'_\lambda + p'_\lambda$$

Similarly, for radiation at all wavelengths, it follows that

$$1 = \alpha' + p'$$

For aluminum tape, assuming that 80% of the radiation is reflected, the rest is adsorbed due to Kirchhoff's law. The remaining 80% is then radiated at the PMMA where 92% of the radiation is transmitted VIS. By assuming that the PMMA transparency at the responsivity area of the sensors is equal to that of VIS region, and since the PMMA is a highly transparent material, the absorption of radiation in PMMA is negligible. Hence, 8% is reflected towards the detector.

3.2.5 Gas filling system and trigging and acquisition system

As shown in Figure 3-12 a significant amount of instrumentation is connected to the MOGELEG channel. FD1 through FD4, pressure transducer, spark generator and plastic release system (later added) are connected to the computer and are being logged in a LabVIEW programmed VI. Valves #1 through #5 are parts of the re-circulation flow, which is connected to the back wall of the MOGELEG channel and makes it possible to circulate the mixture of air and fuel (propane or methane). Valve #5 is the connection between the gas flask and MOGELEG channel, controlling the access of gas. All valves operates pneumatically and have two configurations, closed and open. An overview of the valves used for the gas filling system and the re-circulation system is shown in Table 3-1.

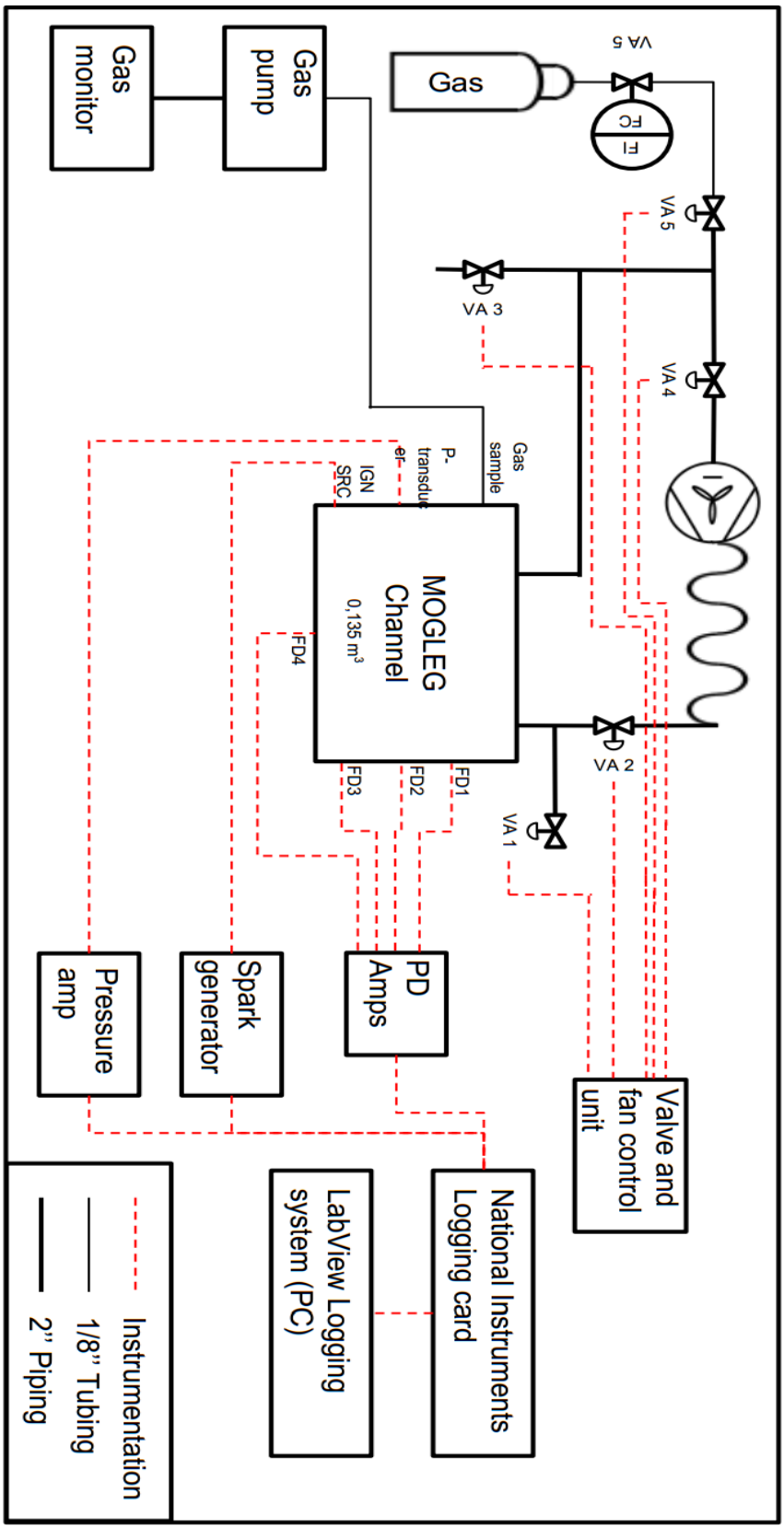

Figure 3-12: Overview of the experimental setup for the MOGELEG Channel.

Table 3-2: Overview of valves and their functions regarding the MOGELEG channel

Valves #	Functions
VA 1	Makes it possible to ventilate mixture to surrounding atmosphere
VA 2	Makes it possible to disconnect MOGELEG Channel from the circulation flow
VA 3	Makes it possible to ventilate mixture to surrounding atmosphere
VA 4	Makes it possible to disconnect MOGELEG Channel from the circulation flow
VA 5	Connected to the circulation flow and gas flask, possible to add gas to the circulation flow.

The plastic release system also operates pneumatically by two pneumatic cylinders holding a wooden frame jamming the plastic in tight between the wooden frame and the MOGLEG channel opening (see Figure 3-10 and Test Apparatus). A three-way pneumatic switch activates 0.2s prior to ignition by the triggering sequence in the VI and releases the plastic.

The operator starts the triggering sequence when the desired gas concentration is achieved and that the concentration has been stable for 1 minute. An air horn sounds the warning of an imminent explosion experiment in 10 seconds to notify the surroundings.

After the experiment, the acquired data was analyzed by using the LabVIEW programmed VI "*Plot program.vi*". The detected arrival time of the flame front was compared to the actual arrival time recorded with the HS camera.

The data from the *Plot programme.vi* look like Figure 3-13. The x-axis shows the time after the logging was started and y-axis shows the voltage output from sensors that the NI logging card receives from sensors. The first spike at 486.3ms is the ignition, the light blue curve represents the pressure, the wide angled detector,FD4 , is represented by the pink curve and the rest of the curves represents remaining flame sensors. In this test configuration, FD4 is closer to the closed end in the MOGELEG channel than FD1 through FD3.

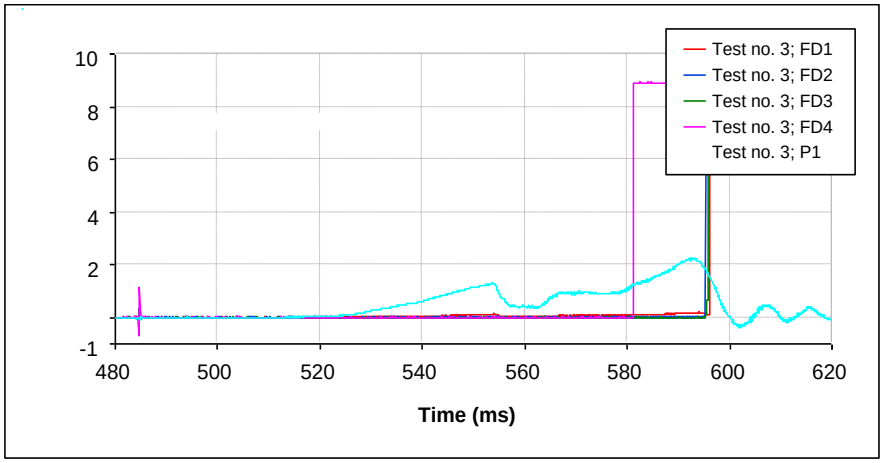

Figure 3-13: Example of measurements from test series 00003 – test 003 – 9.6% methane.

3.2.6 Experimental procedure – MOGELEG channel

The channel was filled with the desired concentration of propane/air or methane/air. Prior to ignition the circulation system is isolated and flushed, the mixture is ignited at the closed end and the flame front propagates towards the open end.

The following experimental procedure was performed:

i. Calibrate gas analyzer with calibration gas
ii. Check tubing, valves and connections regarding the gas system for leaks
iii. Connect Phantom HS camera*
iv. Check valves 1 through 5 and fan
v. Run dummy test
    a. Ignition source test
    b. HS Camera triggering
    c. Plastic release system test
vi. Check safety measures (Safe Job Analysis)
vii. Gas filling
viii. Stop gas filling at desired level
ix. Close valves 2, 4 and 5
x. Open valves 1 and 3 and circulate for 30 seconds
xi. Close all valves and turn off fan
xii. Sound the horn
xiii. Run trigger and logging sequence via LabView (*Sotralogger.vi*)

*note: for test series 00001 Casio Elixim f1 was used instead.

3.3 Large-scale experiments

These tests were conducted at GexCon AS Laboratories at Børnesskogen, Sotra. The 50m^3 test vessel referred to as the module used for large-scale testing measures 2.5x2.5x8m. Similar to the MOGLEG channel the vessel have one open end and a closed end. Three detectors were mounted in the module with intervals of circa 250 centimeters along the centerline in the roof. The ignition source was 20cm from the closed end, in the middle between the roof and the floor. The long sides of the module consists of four 2x2.5m sections as shown in Figure 3-14. The starting point is as shown in Figure 3-14, one steel wall section and three transparent sections were used.

Figure 3-14: The 50m^3 module used for large-scale testing.

The first detector is located 225cm from the closed end wall. Detector two and three are located 475cm and 725cm from the closed wall, respectively, as shown in Figure 3-15.

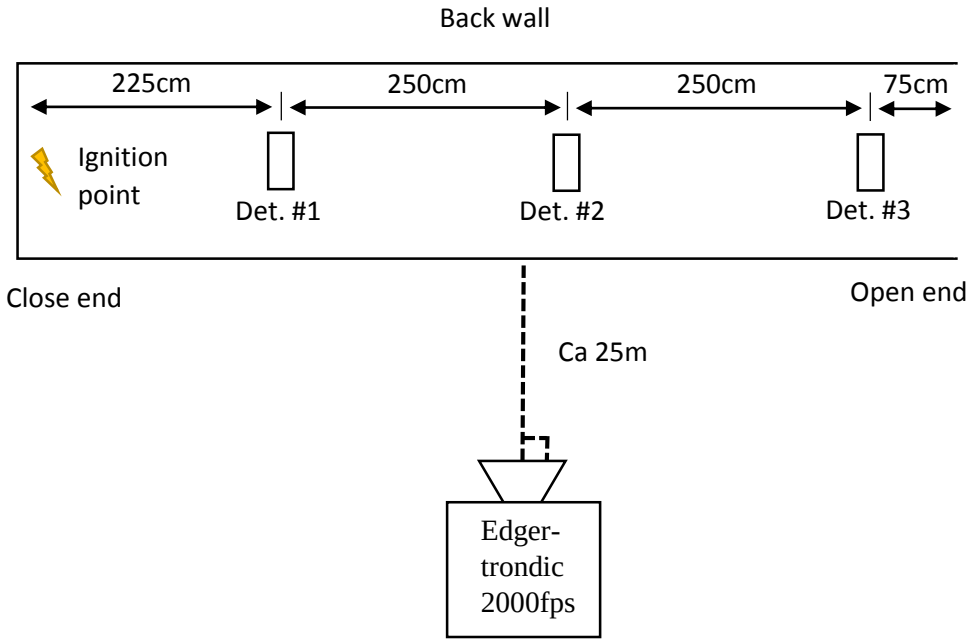

Figure 3-15: Simplified overview of test setup.

The camera used was an Edgertronic, configured with 2000fps and a basic Nikon 1.8f 50mm lens, at a distance of about 25 meters. Higher frame rates was not needed due to the dimension of the large-scale module.

The 50m^3 module had the same functionality as the MOGELEG Channel, only on a bigger scale. This includes a circulation system for gas filling, gas concentration measurements, plastic release system and an electric ignition source. The acquisition and trigger system was controlled using the *Sotralogger.vi*.

Each of the detectors consist of two flame sensors, called FD1 through FD6 during this test series, as shown in Table 3-3. FD1, FD3 and FD5 were observing towards the back wall and FD2, FD4 and FD6 observed towards the transparent wall. The positions of the flame detectors with their representative combined angled of view is shown in Figure 3-16.

Table 3-3: Detectors with respective flame sensors, FD1 through FD6.

Detector #1		Detector #2		Detector #3	
FD1	FD2	FD3	FD4	FD5	FD6

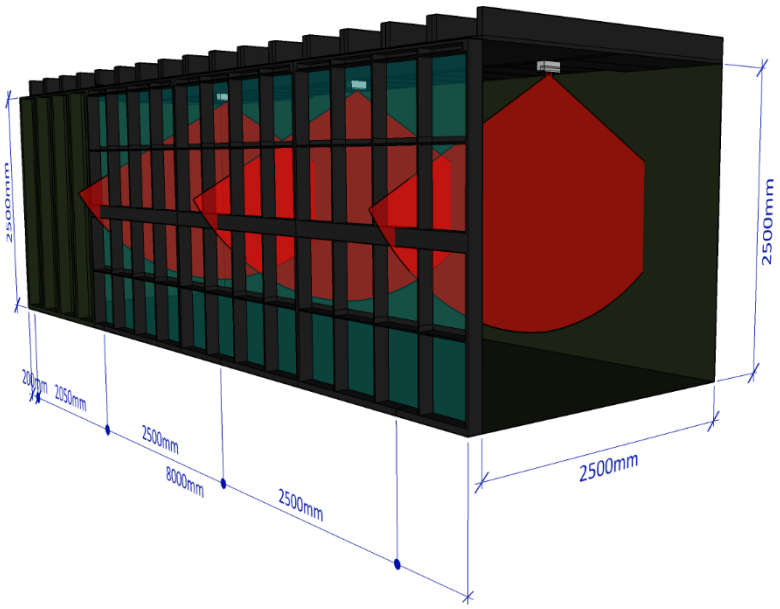

Figure 3-16: Illustration of the flame detectors positions inside the 50m^3 module with respective combined angle of view for each detector.

3.3.1 Flame detectors for use in large-scale experiments

The results produced from test series 00001 through 00007 were the basis of the new detectors. The detectors was designed using Google SketchUp and constructed at the workshop at IFT. The detector incorporated two photodiodes instead of one, hence, increasing the angled sight vision by almost the double. The each sensor has a slit with 60 degrees, 1mm wide slit. There are of sight is within the same plane with a small overlap giving the detectors a total angle of view estimated to about 110 degrees.

The detector was designed to withstand higher pressures. Their aerodynamic properties was neglected due to the small effect they would have on the flow inside the module.

The detectors consists of two photodiodes fitted onto a mounting plate from the top, as shown in Figure 3-17. A slit in the plastic allowed the diodes to view in one plane. The dimensions of the assembled mounting plate with slit bricks is 40x180x59mm.

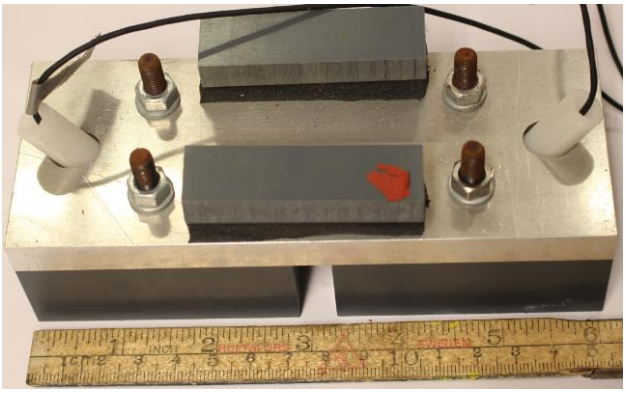

Figure 3-17: The mounting plate where the sensors and slit bricks are fitted.

Figure 3-18 shows the flame detector for use in large scale assembled. The signal cables from the sensors is lead out of the 50m^3 module through the pipe, which is fastened on the module roof. More information about the detectors is in Appendix B.iii – Mark III

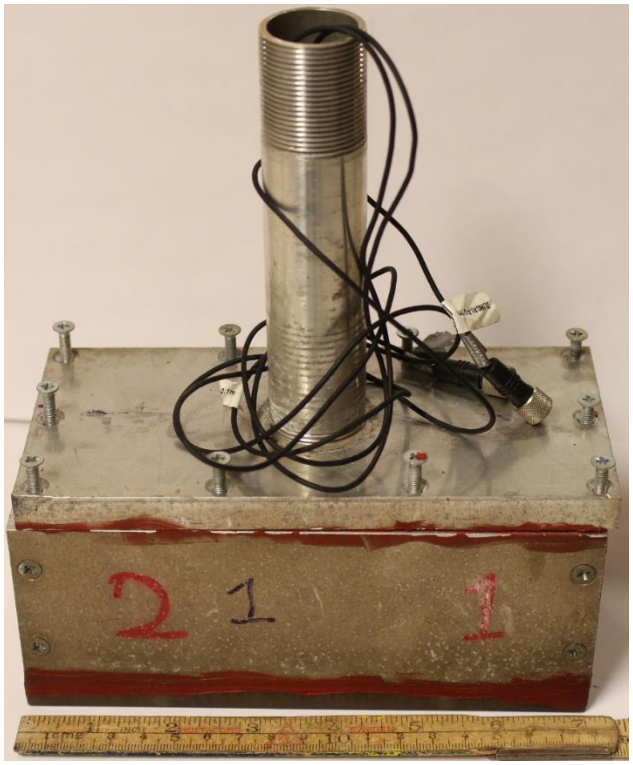

Figure 3-18: An assembled flame detector for use in large scale. The numbers 2 and 1 represents the sensor numbers inside the detector.

3.4 Methodology

3.4.1 Analysis of HS videos

The videos from the HS camera were compared with the time of arrival measured by the detectors. Figure 3-19 shows one frame from the video recording, where the flame front clearly can be seen. The camera was triggered simultaneously with the ignition. As Figure 3-19 shows, the time after ignition is indicated in the lower left corner of the video frame, here as T: +175.097ms.

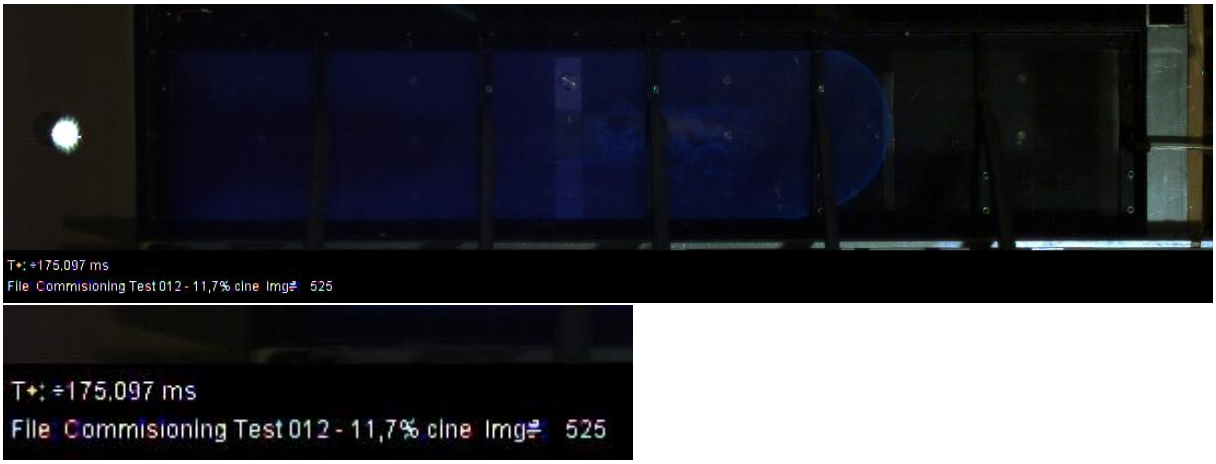

Figure 3-19: The time resolution of Phantom V210 for exported videos, here test series 00002, test 012.

This gave an opportunity to pin-point the flame front position at every on every frame. A frame rate of 3000fps and 5000fps was used. The accuracy of the read out was restricted by the time resolution implied by the frame rate, and the fact that increased flame front velocity leads to a less distinctive flame front. The videos was manually interpreted.

3.4.2 Flame arrival and flame speed

Figure 3-13 show the moment of detections for the sensors during an explosion test in the MOGELEG channel. In pictures from the same test is shown, at the instance of positive flame detection for the various flame detectors. The camera was set at a frame rate of 3 000 fps. The pictures show good correlation between logged time of detection and position of flame when detected. FD4 detects the wrinkle of the eddies generated by the obstruction of BR ≈ 5%.

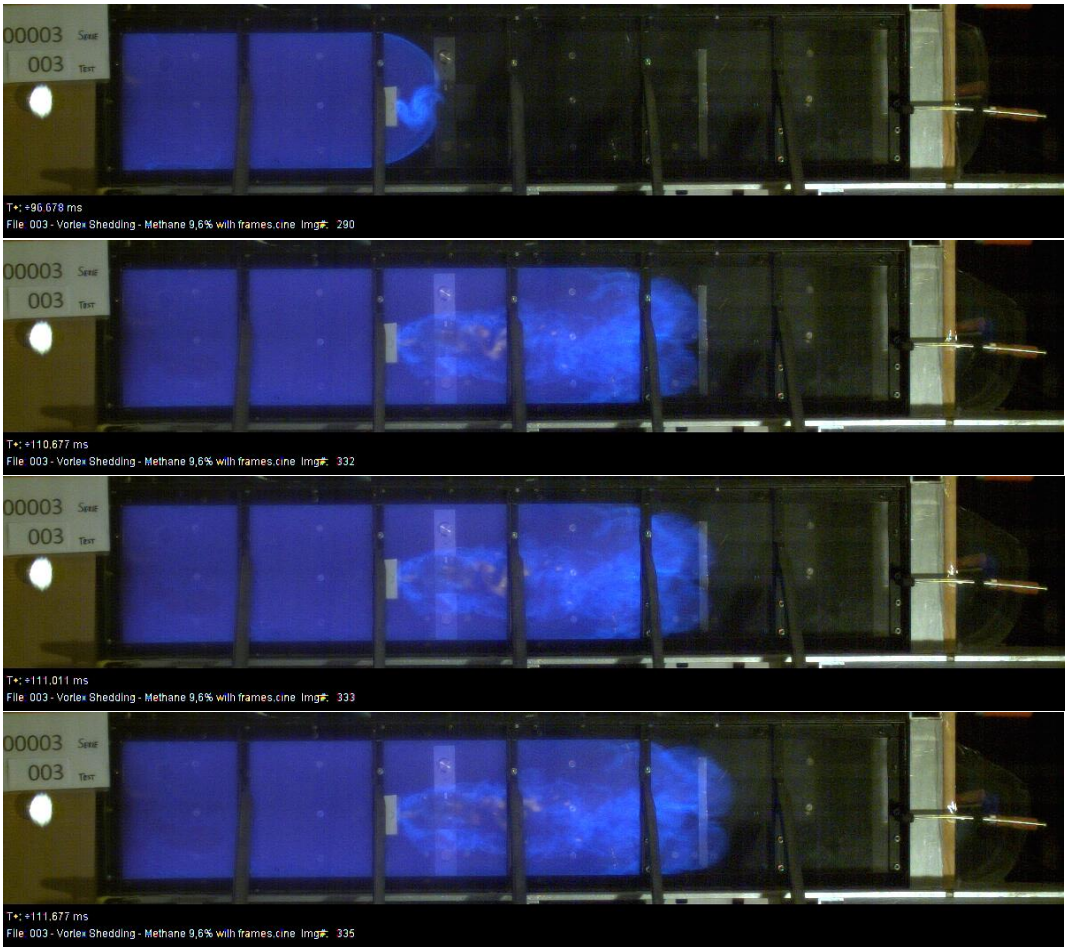

Figure 3-20: Moments of flame front arrival measured by FD4, FD2, FD3, and FD1, respectively.

3.4.3 Trigonometric correction of flame front HS video footage

Due to the camera configurations during the preliminary and optimization test series (see Figure 3-8 and Figure 3-11) the only accurate readout of the flame front will be when the flame front is in front of the angled sight detector. A simple geometric correction must be made for the FD1, FD2 and FD3.

The MOGELEG Channel have six windows divided by supporting irons. The division is used to find the angles between the perpendicular line of sight from the camera to the angled sight detector(FD4?), from camera to the supporting irons. The dimensions of the MOGELEG channel, given by Figure 3-21, were used in combination with the distance of camera given in Figure 3-8 and Figure 3-11 to determine the different angle of views when observing the propagation of a flame front through the channel.

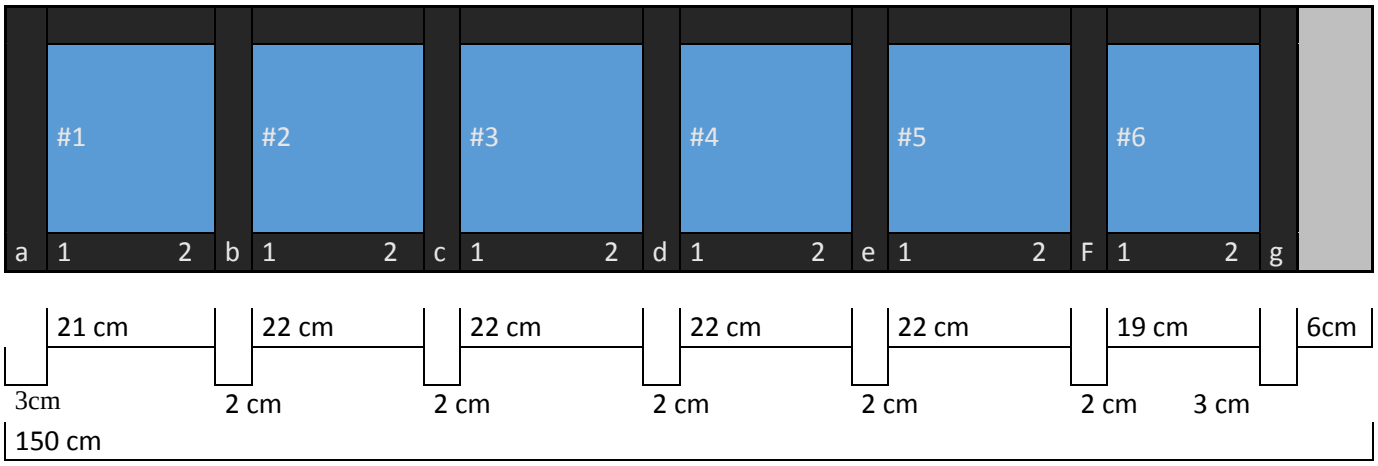

Figure 3-21: Division of the MOGELEG Channel.

Test series 00001 – 00004 had HS Camera perpendicular to window #3 and test series 00005 – 00006 perpendicular to window #5. Averaged angles were found for each window with respect to the distance between camera and angled sight detector. By assuming the flame front to be a semicircle with diameter of 26 centimeters (2centimeters from the walls on each side), finding expression of its slope and by treating the angles as vectors, simple linear algebra will give a distribution of the readout deviations with respect to what window the flame front is observed through. Table 3-4 shows the deviations from the real flame front positions for small-scale experiments.

Table 3-4: Deviations from the real flame front positions for small-scale experiments

	Deviation (cm)	
Window no.	Test series 00001 - 00004	Test series 00005 - 00007
#1	-1,5	-2,8
#2	-0,8	-2,1
#3	0,0	-1,5
#4	+0,8	-0,8
#5	+1,7	0,0
#6	+2,6	+0,8

The table above shows at what distance the flame front is present, with respect to what window frame being observed through. For test series 00001 – 00004, readout of window #1 give a distance 1,5cm shorter than the real position. The table indicates that the deviations are not affecting the results extensively. The biggest deviations are at window #6 and window #1 for test series 00001- 00004 and test series 00005 – 00007, respectively. Figure 3-22 gives the limits of the distribution with respect to

readout edge positions of the flame front. Left side of the figure (black line) represents the back wall of the channel and the right side (blue) the transparent plastic.

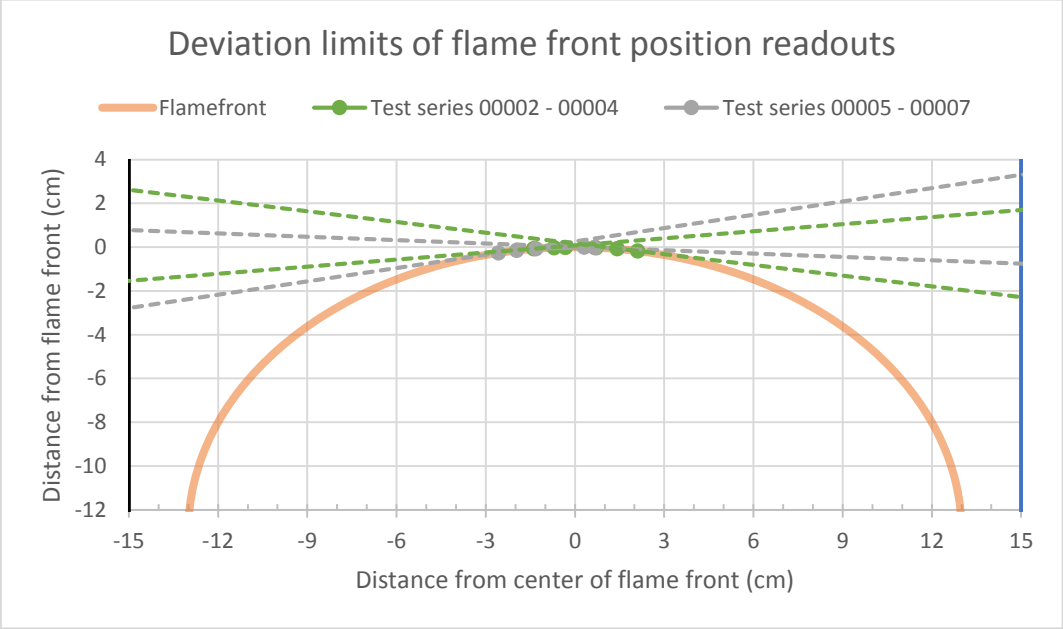

Figure 3-22: The limits of the deviation distributions regarding flame front position readout.

For test series 00002 – 00004, the upper green and grey lines to the left in Figure 3-22 represents the flame front readout from window #6 in Figure 3-21, while the lower green and grey lines indicates the readout from window #1.

The distance between the HS camera and the MOGELEG channel for tests 00002-00005 was 409cm. The relation of this distance divided by the length of the MOGELEG channel is

$$\frac{d_{camera}}{l_{MOGELEG}} = 2.7$$

For test series 00009 this correlation is

$$\frac{d_{camera}}{l_{module}} = 3.1$$

By approximation, the same deviations within the same sectors can be used for test series 00009 as for test series 00002-00005, when scaled.

4 Results and Discussion

The experimental results are presented and discussed in two sections.

Section 4.1 Small-scale - preliminary tests and optimization.

Section 4.2 Large-scale tests

Section 4.1 covers the different experiments carried out in the MOGELEG Channel, regarding testing of the behavior and properties of the photodiodes. The detectors were optimized through exposure of turbulent, transient and laminar combustion. A reflection study was also carried out under the same combustion regimes.

Section 4.2 covers large-scale experiments carried out in the 50m^3 test module, investigating new detectors that were designed based on the results from the small-scale testing.

4.1 Preliminary Tests and Optimization

All tests presented in section 4.1 were conducted in the MOGELEG channel.

4.1.1 Test series 00001 - laminar testing

Test series 00001 investigated the behavior and properties of the two flame detection principles when exposed to premixed methane gas explosions at different fuel-air ratios. The two types of detection principles were compared to investigate how the burning of lean mixtures and rich mixtures would affect the sensors and in what degree the sensors would detect the different flame fronts. According to [30], photodiodes could be applied to map the contour of the flame front, this was also investigated by the line-of-sight detectors. Table 4-1 shows an overview of the test configurations for test series 00001.

Table 4-1: Test configurations for test series 00001

Test series 00001		
Test no.	Gas concentration	Fuel-air ratio ϕ
002	9,4 %	1,01
003	6,3 %	0,68
004	7,3 %	0,78
005	6,5 %	0,70
006	6,7 %	0,72
007	6,9 %	0,74
008	11,9 %	1,28
011	10,9 %	1,17
012	11,4 %	1,23
013	10,5 %	1,13
014	9,8 %	1,05
019	12,4 %	1,33
020	12,9 %	1,39

Tests 003, 005, 006 and 007 provided interesting information about both the behavior of the photodiodes and of the two detection principles. As Table 4-2 shows, the flame front developed under these conditions did not radiate sufficiently to generate detections for all detectors. For ϕ=0.68 and ϕ=0.70, only FD4 (angled sight detector) detects the flame even though all sensors had equal preconfigured sensitivity, indicating a lower limit for the detectors at the specific amplifier setting with respect to fuel-air ratio.
The single detection by FD4 in test 003 and 005 is probably due to its slit configuration, giving space for more radiation be emitted onto the photodiode.

Table 4-2: Tests where the flame front was not detected by one or more detectors

Test no.	air-fuel ratio, ϕ	Detection?			
		FD4	FD3	FD2	FD1
003	0,68	YES	NO	NO	NO
005	0,70	YES	NO	NO	NO
006	0,72	YES	YES	YES	NO
007	0,74	YES	YES	YES	NO

At fuel-air ratio below unity, the 600fps camera was not sensitive enough to get a clear view of the flame front, making it difficult to determine the flame front position relative to the detectors.

No upper limit was found for the preconfigured sensitivity settings for the detectors. It is uncertain if a non-detected flame front would occur or not. However, it might be possible that a fuel-air ratio value of a non-detecting flame front would not be found, since the ignitability of the gas mixtures decreases when approaching LEL. The ignition system and the MOGELEG Channel were not designed to carry out such tests.

Figure 4-1 shows the measured positions of the flame front measured by the detectors relative to the flame front position measured using the camera . For these detections, the difficulty of mapping the tests with ϕ<1 were bigger than that of ϕ>1 due to lower intensity and the sensitivity of the 600fps camera. 1st detection represents the flame front detection carried out by the angled sight detector and 2nd detection represents the first detector of FD1 – FD3 that reacted to the flame.

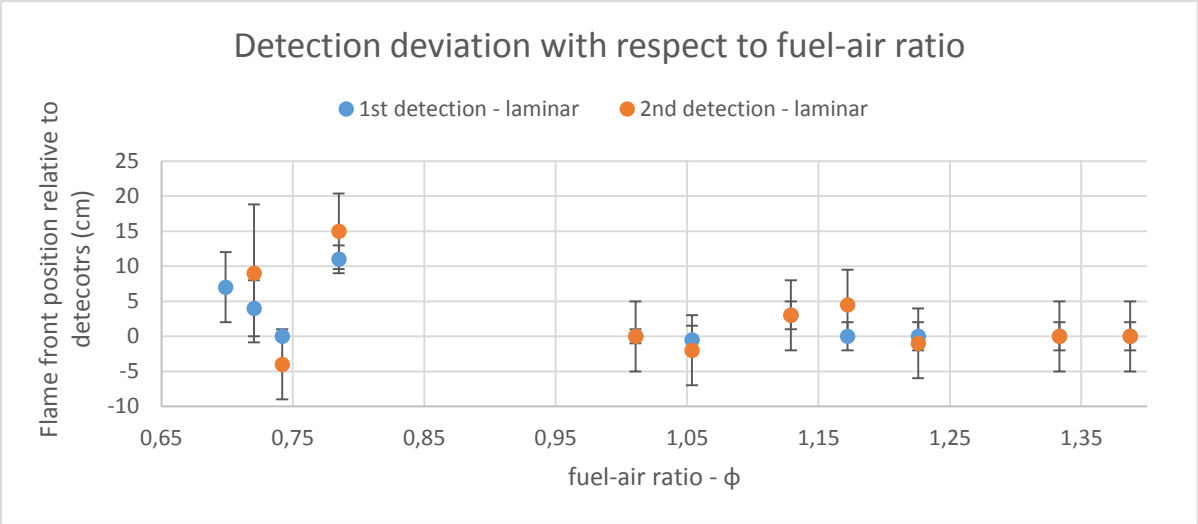

Figure 4-1: Detection distance between real flame front positions and detector positions.

FD2 reacted first of the three line-of-sight detectors for all experiments carried out during test series 00001, most probably due to the curvature of the flame front. Figure 4-2 shows that the flame fronts curvature changed with respect to the fuel-air ratio. Flame fronts during tests of $\phi \geq 1.0$ had a shape approximated to that of a hemisphere, as shown in Figure 4-2. Hence, the flame front passed FD2 before FD1 and FD3. For the tests with $\phi < 1$, the flame fronts had a shape closer to that of a half hemisphere. However, the highest intensities were at the bottom and to mid height in the channel, leading to detection at FD 2 before FD3.

Figure 4-2: Comparison of test 002, above, and test 006, below with approximated flame front and position of line of sight detectors. The angled sight detector is slightly visible in the middle of both pictures due its aluminum attachment.

Table 4-1 shows that test 002 had a fuel-air ratio $\phi = 1.01$ and Figure 4-2 shows the blue color of the flame front during the test. The figure also shows test 006 with $\phi = 0.72$. However, the brightness and contrast of the video had to be highly adjusted to bring forth some contour of the flame front.

Due to both noise and the low light sensitivity of the video footage for tests with $\phi < 1.0$, it was difficult to find the time of ignition, leading to readout deviations of a higher magnitude. . The time of ignition was estimated analyzing the flame propagation recorded by the camera. This methodology gave an accuracy regarding moment of detection within an uncertainty of ±10 frames (16.667ms).

The effect of the turbulence generated by the angled sight detector inside the MOGELEG channel was also assessed. The video from test 002 gave good indications on how the geometry of the angled sight detector affects the flow of the explosion. Figure 4-3 shows a closer view of the flame front test 002 as shown in Figure 4-2. It shows that the detector deflects part of the flow such a way that it crosses the nominal flow in the x-direction towards the open end. The black areas inside the flames in both Figure 4-2 and Figure 4-3 show that the flame front has burnt onto the walls of the long sides, and hence, extinguished locally because the fuel is depleted in that region or its concentration is below LEL.

Figure 4-3: Close up of flame front for test 002 as shown in Figure 4-2.

Based on the information in Figure 4-3, Figure 4-4 shows a possible approximation of the flow pattern generated during an explosion by the geometry of the angled sight detector . Most of the flame front stay unaffected when passing the detector. The flow at the inner long side was probably pushed out due to the decreased diameter of the channel. When the flame front position is in the middle between the angled detector and the open and, the flow which will be pushed out from the wall, as shown in the figure below, has managed to cross the nominal flow obliquely and burned onto the transparent plastic, hence generating a “black hole”.

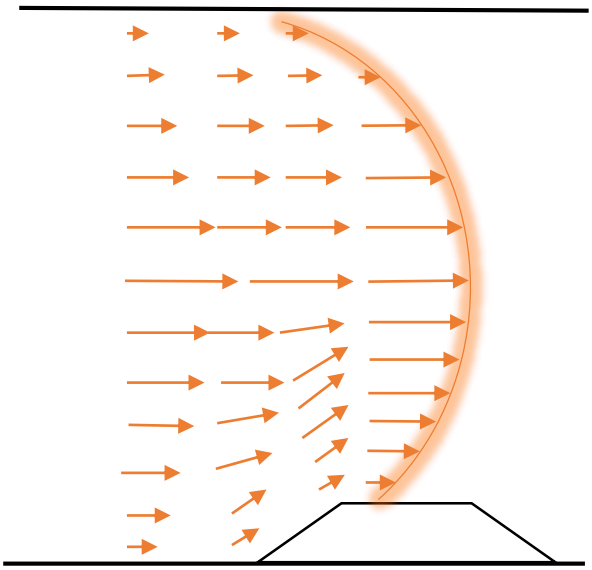

Figure 4-4: Approximation of the effect of the detector geometry on the flow, in the XY-plane mid height Z-direction.

The black areas in the center of the MOGELEG channel, shown in in Figure 4-3, is the burnt region of the explosion containing the products of the reactions, water and carbon dioxide among others.

For experiments with transient and turbulent premixed explosions, the 600fps camera was seen as unfit. Pedersen H.H. [32] gives indications that velocities exceeding 100m/s can be expected when conducting turbulent premixed explosions in the MOGELEG channel. By simple calculations, it is possible to show that the 600fps camera is unable to give sufficiently accurate measured data as the

flame front velocity increases. Table 4-3 show how the flame front will look like on a 24" computers screen when the videos are enlarged to 400%, which is needed for good readouts. Table 4-3 indicates that for higher flame front velocities, the flame front will be more stretched and dragged. The table show how long the flame front will travel during one frame, 1.6ms. When passing the velocity of 0.020 m/ms the flame front become blurry, making it hard to determine its position. Hence, the Elixim camera was only applied during the approximated laminar tests during tests series 00001.

Table 4-3: Overview of distance moved per frame at 600fps at different flame front velocities

Velocity (m/ms)	**Distance moved per frame on 24" observation screen (cm)**
0,001	0.1<
0,005	0,2
0,010	0,5
0,015	0,7
0,020	0,9
0,100	4,5

One way to improve the output of the videos at 600fps would be to do all of the tests with the lights in the ceiling and other surroundings, off. However, it would also make it very hard to find the detectors on the film, making it almost impossible to decide the position of the flame front with respect to these detectors.

For testing of the flame front mapping applicability of the photodiodes, the videos were sufficient . Since the line-of-sight detectors were dependent of the right fuel-air ratio value to detect the flame, the applicability were to some extent limited. However, when the flame fronts were detected by the line-of-sight detectors, the contour became mapped as Table 4-4 indicates. FD2 detects the flame front 1.3ms and 1.6ms before FD1 and FD3, respectively, due to the curvature of the flame front. FD1 detects 0.3ms before FD3, indicating that the flame front has been shifted a bit. By looking at Figure 4-5 and comparing the top half of the curve to the bottom half, it is barely observable that the top half is a bit closer to the roof of the channel than the other half is to the floor.

Table 4-4: Time of detection by line-of-sight detectors indicating the contour of flame front

Test series 00001	
Test no. 002	
Detector	Time after ignition (ms)
FD1	117,6
FD2	116,3
FD3	117,9

4.1.2 Test series 00002 – improved laminar tests

Test series 00002 was compared to and validated the investigated parameters found in the previous test series. An improved camera was applied and the same type of tests as in previous test series were carried out. The tests carried out during test series 00002 had fuel-air ratio between $0.70 < \phi < 1.30$. An overview of the tests conducted and their configurations is shown in Table 4-5.

Table 4-5: Test configurations of test series 00002

Test series	**00002**	
Test no	Gas concentration (%)	Fuel-air ratio
002	9.7	1,04
006	9,3	1,00
007	6,6	0,71
008	7,9	0,84
010	9,4	1,01
011	10,3	1,11
012	11,7	1,26

A Phantom V210 HS camera with 3000fps and resolution of 420x1140, replaced the 600fps camera. It was placed in the same position as the previous camera, normal to the angled sight detector. The HS camera was fitted with a 1.4f 50mm Nikon lens giving an opportunity to change the aperture, hence eliminating the light sensibility issue. A piezoelectric pressure transducer was fitted close to the upper corner in the closed end of the MOGELEG Channel, measuring the pressure development of the gas explosions. Both the camera and a LED spot bulb were added to the trigger sequence. The LED spot bulb indicated by illuminating when the ignition was trigged.

The relative flame front positions when detected for test series 00002 compared to those of test series 00001 are plotted in Figure 4-6.

Figure 4-6 shows that when comparing the measured flame front positions relative to their respective detectors, readout deviations of test series 00001 is of a higher magnitude than that of test series 00002. The flame front positions of 00002 is within the range of about -2cm to +5.5cm, while for test series 00001 it varies from almost -5cm to +15cm. The largest deviation with lean mixture for series 00001 is at $\phi=0.71$ with a magnitude of ±10 centimeters. For 00002, the highest magnitude of deviation is ±1 cm at $\phi=1.00$ and $\phi=1.04$. Test series 00002 shows how the improved camera and time resolution lead to a higher degree of accuracy, hence the lowered magnitude of readout deviations. Figure 4-6 also shows for test series 00001 that the accuracy is increased with increased fuel-air ratios, however test series 00002 is still more accurate. The results show how the accuracies of detections is dependent on the quality of the applied equipment.

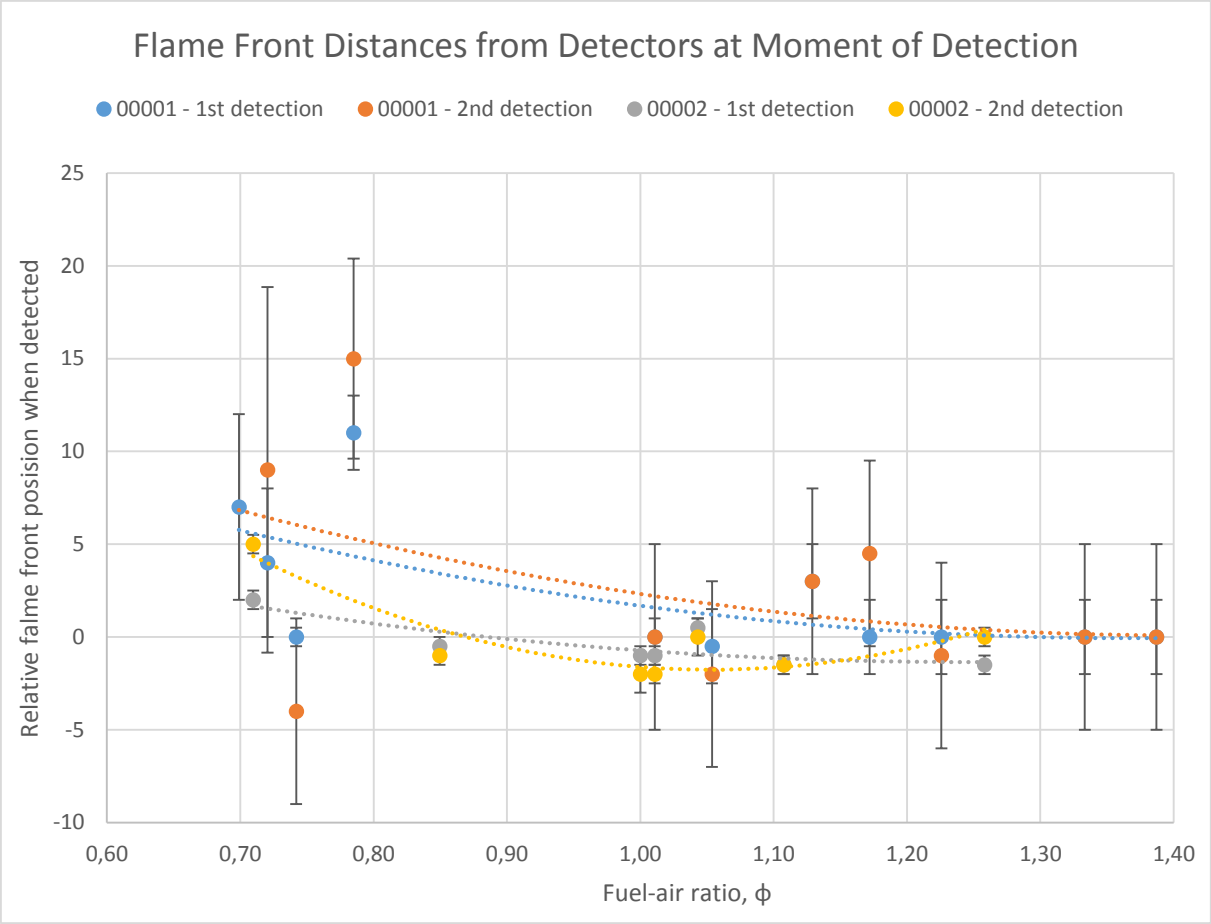

Figure 4-6: Comparison of detection deviations between test series 00001 and 00002.

4.1.3 Test series 00003 – 00004 transient and turbulent combustion

Test series 00003 and 00004 were conduct to investigate the behavior and properties of the flame detectors when exposed to transient and turbulent explosions. In addition, it was also investigated if FD1-FD3 would achieve flame front mapping within these combustion regimes. Test series 00003 was carried out with transient explosions while test series 00004 was carried out with turbulent explosions.

Prior to test series 00003, the MOGELEG Channel was fitted with a 16mm horizontal pipe about 50cm from the ignition source, mid height, achieving BR = 5%. The fuel-air ratio of the tests covered lean, stoichiometric and rich mixtures, as shown in Table 4-6: Test configurations for test series 00003 and 00004Table 4-6.

Table 4-6: Test configurations for test series 00003 and 00004

Test series 00003		
Test no.	**Gas concentration**	**Fuel-Air ratio**
002	9,6%	1,03
003	9,6%	1,03
004	9,6%	1,03
005	11,9%	1,28
006	7,9%	0,85
007	10,7%	1,15
Test series 00004		
Test no.	**Gas concentration**	**Fuel-Air ratio**
001	9,5%	1,02
003	12,1%	1,30
004	10,6%	1,14
005	7,8%	0,84
007	6,8%	0,73

Tests 002 and 004 were carried out with the same gas concentration to validate the repeatability of the test setup. Tests 002 and 003 lack pressure data. Table 4-7 shows some deviations between the tests at 1st detection and at 2nd detection, shown as milliseconds after ignition. One reason for this may be the lack of a plastic release system. The plastic was mounted between the aluminum end of the channel and a wood frame that was held by three clamps. It was difficult to fasten the plastic in such way that it would yield at the same conditions every time. According to Pedersen [32] the plastic yielded at ~30mbarg for this plastic fastening method. For the lean mixtures, the plastic yielded either when the flame burned through it or right before the flame arrived at the open end. For rich mixtures, higher pressures were generated and the plastic yielded before that of lean mixtures. The mixtures close to stoichiometric concentrations generated the highest pressure before the plastic yielded.

Table 4-7: Moments of detections (in ms after ignition) and some pressure data – test series 00003.

Test no.	**1st detection (ms)**	**2nd detection (ms)**	**p_{max}**	**dp/dt**
002	96,0	111,0	-	-
003	96,6	110,8	-	-
004	96,9	112,3	0,24	130 bar/s

Prior to test series 00004, four more tubes were added to the MOGELEG Channel, all with the same dimensions as the previous one. The tubes were put 5cm apart from each other to generate a premixed turbulent combustion process leading to turbulent explosions. Figure 4-7 shows the relative flame front positions of the detections in the explosions carried out in test series 00003 and 00004. Test series 00003 is close to transient due to the transitional flow pattern compared to 00002 (laminar), and with the presence of vortex shedding. For test series 00003, the characteristic curve of the flame front is torn in the center when passing the obstacle, however, the edges of the flame front endure until the center of the torn flame front reaches FD2.

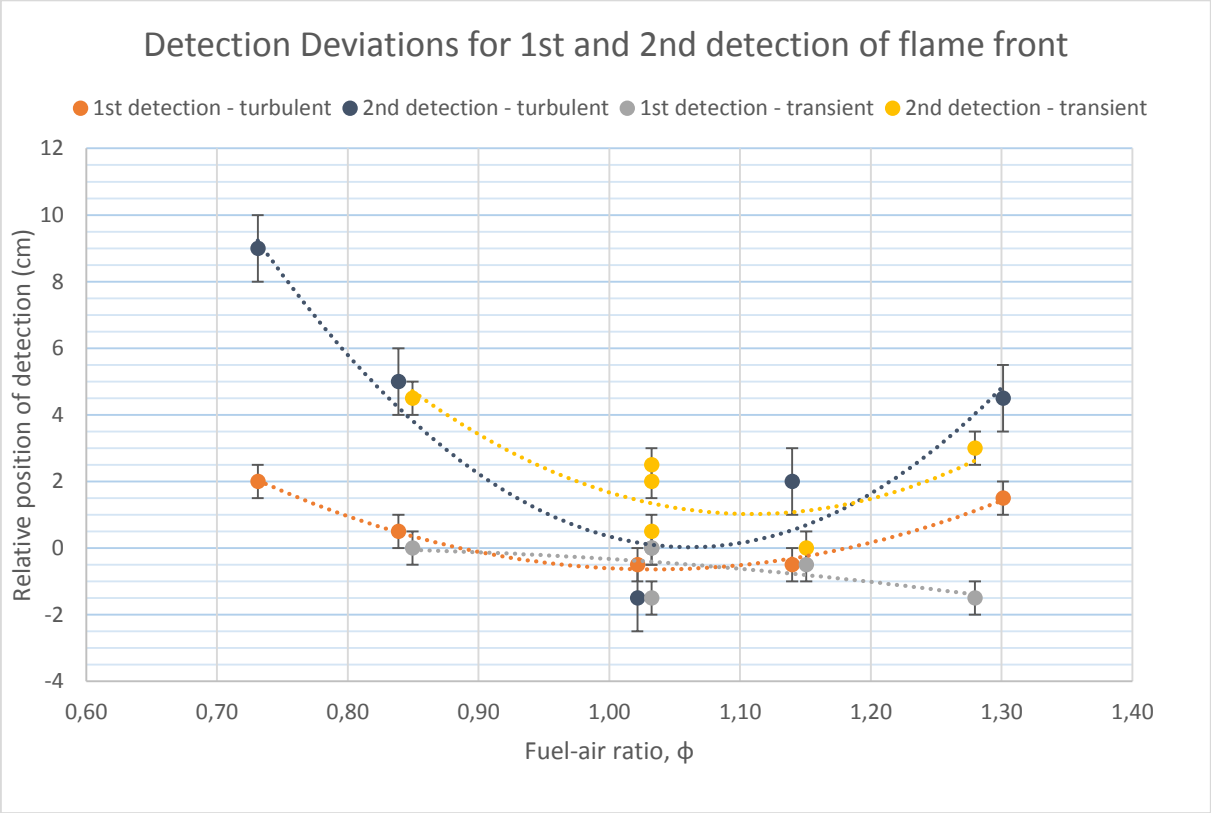

Figure 4-7: Distance between flame front and detector in x-direction at the moment of detection for test series 00003 (transient) and test series 00004 (turbulent).

An interesting result from test series 00003 and 00004 is the correlation between the fuel-air ratio and the distance from detectors to the flame front when they are detecting the flame. The graph in Figure 4-7 imply shows that the detectors are more accurate around stoichiometric fuel-air ratio mixtures than for leaner and richer mixtures. There are probably various reason for this. The lean mixtures burns with less intensity, hence, less radiation are being emitted as the fuel-air ratio decreases. Therefore, the photodiode struggle to achieve enough photons to pass the threshold determined by the sensitivity on the amplifier to generate detections. This is also observed in the test series 00001 and 00002. The trend of increasing distance deviations for detection as the fuel-air ratio increases is quite interesting. The tube mounted in the MOGELEG Channel generates vortex shedding. The vortex eddies transform into larger eddies which then go around from the outside at the edge to the inside of the

center, hence, generating a wake in the middle of the flow. This wake often occurred in front of FD2, which detect the flame front first. One other reason for the wake generation might be the effect of angled sight detector's geometry has on the flow, as shown in Figure 4-4, pushing the center flow towards the transparent plastic.

Another observation is that the flame front propagates slower at the edges of the channel due to friction at the walls, hence, FD1 and FD3 detects the flame after FD2.

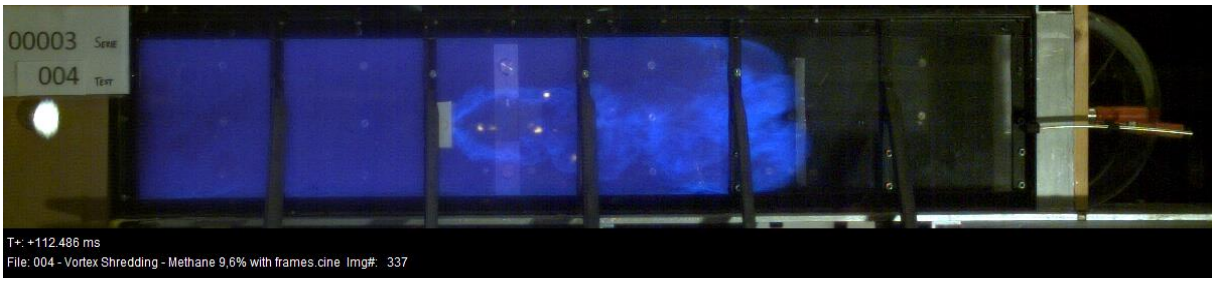

Figure 4-8: The combination of friction at wall, turbulence and eddies generation, and the angled sight geometry, affect the flow in such a way that a effect is generated.

Figure 4-9 shows zoomed view of the flame front in Figure 4-8. It is not straight forward to distinguish the flame front when it became more turbulent than that of test series 00001 and 00002. Two reasons for this, among others, are the speed of flame front with respect to fps rate of the camera and that the flame front is somewhat wrinkled.

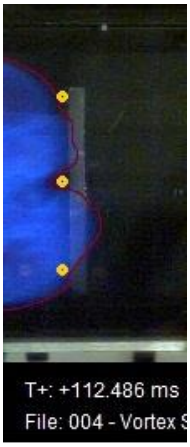

Figure 4-9: Close up from Figure 4-8 showing the approximated outline of the flame front and the line-of-sight detectors.

Regarding the plotted data in Figure 4-7, the relative position of the flame front with respect to the angled sight detector when detected is depending on types of combustion and the type of detectors. It is important to understand that these numbers are strongly dependent on the geometry.

Table 4-8 shows ranges of relative flame front positions with respect to combustion types for the angled sight detector and the line of sight detectors.

Table 4-8: Ranges of relative flame front positions with respect to combustion types

Test series 00003-00004		
Type of detector	Combustion regime	Range
Angled sight	Turbulent	-2.0cm, +2.5cm
Angled sight	Transient	-2.0cm, +0.5cm
Line-of-sight	Turbulent	-2.0cm, +9cm
Line-of-sigh	Transient	-0.5cm, +5cm

For the testing of the applicability of the photodiodes regarding mapping the flame front during transient combustion, the data acquisition compared to the HS video were ambiguous. The moments of detections by the line-of-sight detectors are listed in Table 4-9.

Table 4-9: Time of detection by line-of-sight detectors indicating the contour of flame front

Test series 00003	
Test no. 004	
Detector	Time after ignition (ms)
FD1	113,1
FD2	112,3
FD3	112,5

FD2 detects the flame front 0.8ms and 0.2ms before FD1 and FD3, respectively, due to the shape of the flame front. By looking on the flame front from Figure 4-9, the flame front consists of two “bumps” and a wake between them. FD2 is placed in the wake while the “bumps” passes FD1 and FD3. The bottom “bump” is in front of the other, which is also confirmed by the moments of detections. Example of drawing a flame front on the basis of Table 4-9 is shown in Figure 4-10.

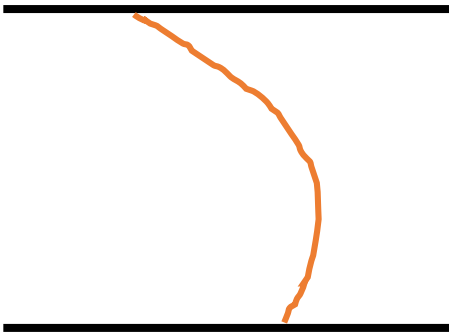

Figure 4-10: Approximated flame front based on the data of Table 4-3.

Comparing the flame front illustrated in Figure 4-10 with the flame front in Figure 4-9, indicates the limitation of using the line-of-sight detectors for mapping the flame front. Knowledge about the flow speed and the geometry is needed to predict a more realistic description.

4.1.4 Test series 00005 – 00007 reflection tests

This test series was conducted to investigate the behavior of the detectors when exposed to a reflecting environment. The MOGELEG Channel is ideal when considering non-reflecting conditions. The interior is painted with matt black paint except from the transparent plastic, and a few aluminum tape pieces to mark certain position within the channel. Test series 00005 investigated how the 2mm slit of the angled sight detector would react with increasing reflective area around it with constant fuel-air ratio. Test series 00006 investigated how the sensitivity adjustments could optimize the accuracy of the angled sight detector at lean, stoichiometric and rich mixtures. Test series 00007 investigated the effect on accuracy when changing the slit dimensions.

Test series 00005

Test series 00005 was carried out by gradually adding reflecting areas around the detectors. to investigate the effect reflection has on the detection at almost constant stoichiometric mixtures (0,99 < ϕ < 1,02). Aluminum tape was added around the detectors and was chosen due to the metal's highly reflective properties. Table 4-10 shows an overview of test configurations for test series 00005.

Table 4-10: Test configurations for test series 00005

Test series 00005				
Test no.	Gas concentration	Fuel-air ratio, ϕ	Configuration	Added effective reflection area
001	9.4 %	1.01	Reference test, no added reflection	0%
003	9.2 %	0.99	Reflection on the transparent plastic, button and top.	70%
004	9.5 %	1.02	Reflection on the transparent plastic, button, top and back wall.	92%
005	9.5 %	1.02	Reflection on the transparent plastic, button, top, back wall and on detector geometry.	100%
006	4.0 %	1,00	Reflection on the transparent plastic, button, top, back wall and on detector geometry (extreme reflector). Change of gas: Propane gas.	100%

The area calculations is based on how much of the area inside the MOGELEG Channel that is being covered by aluminum tape. The reflection added on the inclined plane of the angled sight geometry prior to test 0005, tried to bounce thermal radiation back and forth between the back wall and transparent plastic or from the reflecting inclined plane of the angled sight geometry and onto the transparent plastic. The reason for this configuration was to compel the earliest detection possible, making an almost worst-case scenario for the angled sight detector.

The relative positions of the flame front with respect to gradually addition of reflective areas are shown in Figure 4-11. The figure describes the detection relative flame front position with respect to angled sight detector when detected. As expected, the more reflection added, the earlier detection, especially when extreme reflection was achieved (100%). The extreme reflection's relative reflection area is actually 93%, but due to the inclination of the reflecting area on the angled sight detector geometry,

it was put 100%. This reflection and detection deviation distribution is quite simplified and scarce, but it clearly shows the results from the tests.

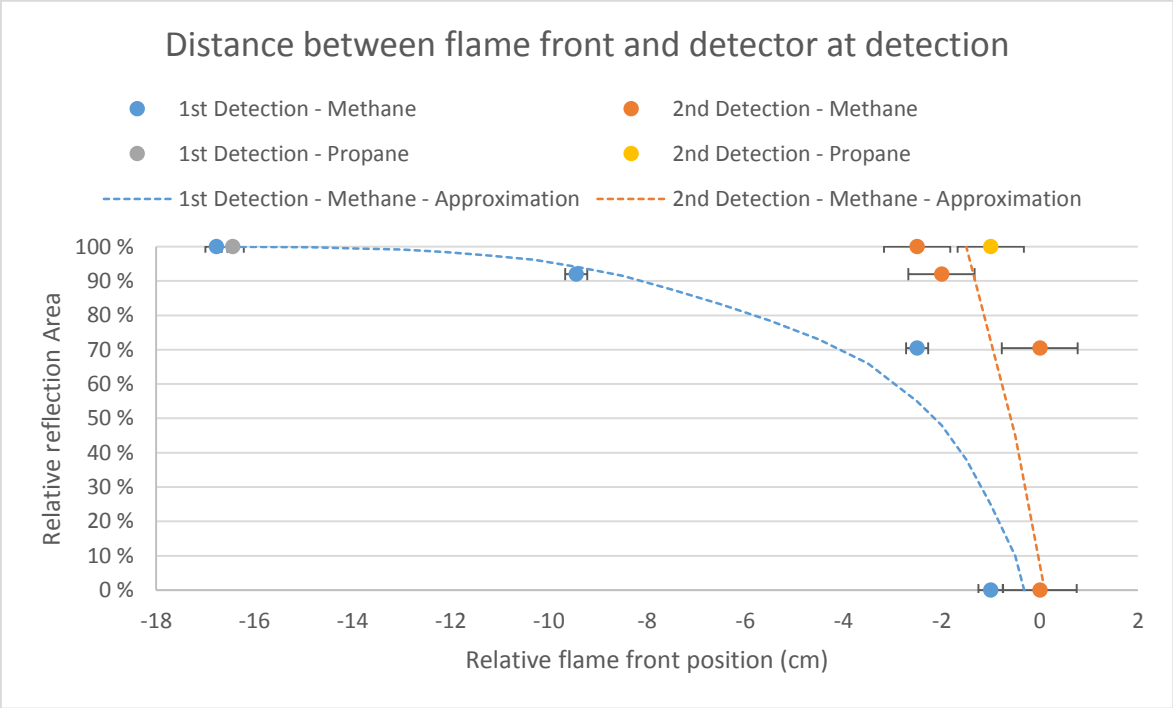

Figure 4-11: Correlation between amount of reflection and detection deviation.

That the line of sight detectors is also affected, but not to the same extent, is possible due to the reflection surface added around the angled detector. Though it is a significant distance between the angled and line of sight detectors, the pebbled surface of the aluminum tape can contribute to earlier detection due to reflections that “sends” more photons towards the line of sight detector so that they elevates above the threshold (determined by the sensitivity configuration) resulting in premature detection.

The contribution of the extreme reflection is sufficiently large enough to generate even earlier detections than without it. There are probably several reasons for this. By adding the aluminum to the inclined plane on the geometry will by pure logic, contribute to the earlier detection. However, the magnitude of the contribution is another question. One way to find out is to look for the limits of the reflections on the inclined plane. By working backwards from the angled sight detector and towards the source of radiation, it is possible to project an area onto the flame front from where the radiation come from using the vectors which define the limits of the necessary directions of radiation to hit inside the slit opening. Figure 4-12 shows an illustration of the backwards reflection projections.

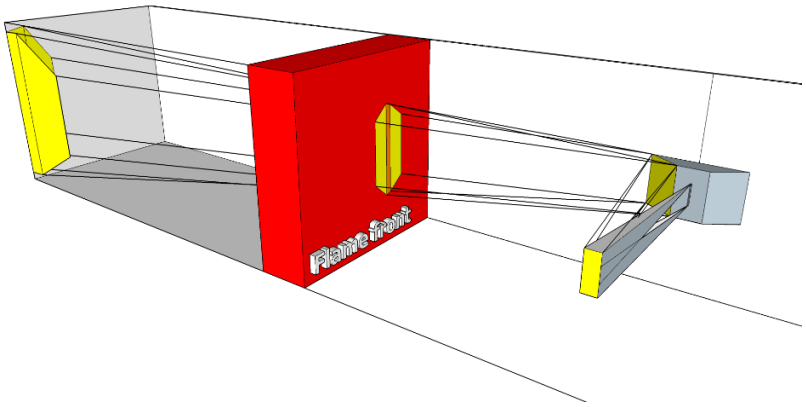

Figure 4-12: Backwards reflection projections.

Figure 4-12 is simplified but can describe the phenomena. The flame front is 15cm from the angled view detector. The yellow areas corresponds to the areas of reflection. The smallest area is the reflection occurring onto the transparent plastic on the outer wall. The reflection that occurs at the inclined area of the angled sight detector geometry makes it possible to project the flame front and beyond it.

As seen in Figure 4-8, the flame front has an approximated curvature geometry and it does not burn as a plug. It takes more time for the flame front to burn towards outer walls (transparent plastic) than towards the open end. It is easier for the expanding forces of the explosion to push the mixture in front of itself than the unmoving walls. Figure 4-13 shows projected area of reflecting radiation of a curved flame in the MOGELEG Channel viewed from above.

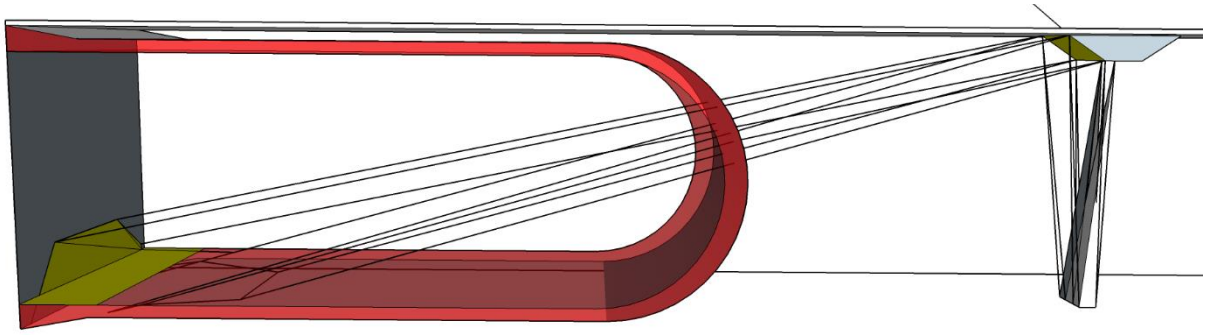

Figure 4-13: Projected area of reflecting radiation of a curved flame in the MOGELEG Channel, top.

This is a simplified model to illustrate that the area of emission is not at the front but also at the back of the flame front.

Test series 00006 was conducted with various fuel-air ratios, lean, close to stoichiometric and rich mixtures. The frame rate of the camera was increased from 3000 to 5000 fps without changing the resolution. The test series was also conducted to investigate if reducing the sensitivity decreases the detection deviation due to higher threshold before detection. Since the amplifiers are digital and the sensitivity is only a control dial, the sensitivity level is difficult to calculate.

Test series 00006

This series was a comparative study of extreme reflection cases regarding the angled sight detector with rich, lean and stoichiometric mixtures. HS video footages show that the flame front accelerates throughout the channel after passing the vertical obstacles. Hence, the two different kind of detectors changed positions, on order to investigate how they would behave under slightly different conditions (see Figure 3-11).

The tests were carried out in groups of three with different fuel-air ratios. The reflection configurations of the tests were unchanged for each group as shown in Table 4-11: Test configurations for test series 00006 . The amplifier sensitivity was adjusted prior to tests 004 – 006 and tests 007-009. Reference tests were necessary due to the new position of angled sight flame detector.

Table 4-11: Test configurations for test series 00006

Test series 00006			
Test no.	Gas concentration	Fuel-air ratio, ϕ	Sensitivity configuration
001	4.1 %	1,02	Reference (no change) – High sensitivity
002	3.1 %	0,77	
003	4.8 %	1,19	
004	4.8 %	1,19	Medium sensitivity
005	3.2 %	0,80	
006	4.2 %	1,04	
007	4.8 %	1,19	Low sensitivity
008	4.1 %	1,02	
009	3.2 %	0,80	

Flame front positions relative to the angled sight detector are plotted in Figure 4-14. High sensitivity leads to a higher grade of scattering between the relative positions. Two trends appear when the sensitivity decreases. Firstly, the difference in flame front positions relative to the angled sight detector for tests with different fuel-air ratios decrease when reducing the sensitivity. Secondly, the flame front positions relative to the angled sight detector decreases by reducing the sensitivity. In other words, it becomes more independent of the difference in thermal radiation intensity of the flame fronts. The red line indicates the position of the angled sight detector.

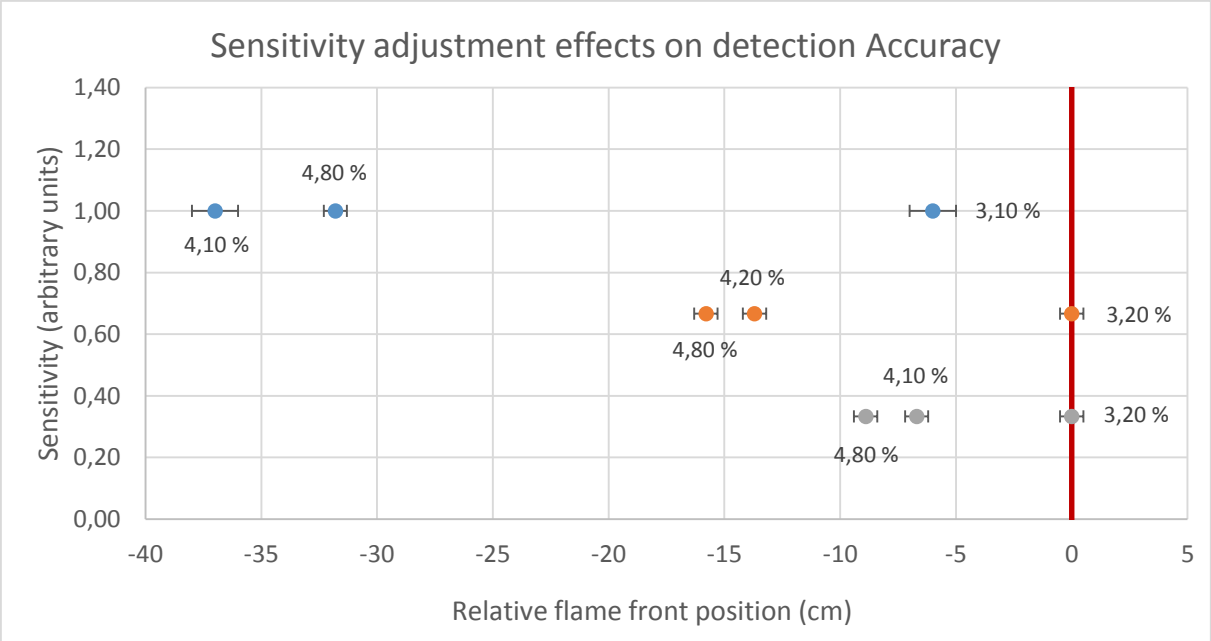

Figure 4-14: Detection accuracy results - test series 00006.

Test series 00007

This test series was conducted to investigate the influence of different slit configurations on the detection accuracy of the angled sight detector. All tests prior to test series 00007 were conducted with slit properties as described in Appendix B, Figure B-4. The tests carried out during test series 00007 were performed with different slit bricks under various fuel-air ratios. Tests 001 through 010 were carried out with the same reflection configuration on the transparent plastic as test series 00006. Prior to test 011, the reflection configuration on the transparent plastic was changed. The middle of the window, which was used to observe the flame front, was covered with aluminum tape to investigate the effect of a more reflective surface than transparent plastic. As the radiation vectors in Figure 4-12 and Figure 4-13 indicates, the extreme reflection bounce the radiation onto the middle of the transparent plastic. The new reflection configuration tried to compel earlier detections due to more reflection. The fuel-air ratio used in these tests were similar to previous tests, hence the approximate time of detection after ignition could be estimated.

Table 4-12 shows an overview of tests carried out during test series 00007.

Table 4-12: Test configurations for test series 00007

Test series 00007				
Test no.	**Gas concentration**	**Fuel-air ratio, ϕ**	**Configurations**	
001	4,5 %	1,12	Slit #1	Without extreme reflection
002	3,8%	0,96		
003	4,9%	1,22		With extreme reflection
004	4,9%	1,22	Slit #2	
005	4,8%	1,19		Without extreme reflection

006	4,0%	1,00		
007	4,5%	1,12	Slit #3	With extreme reflection
008	4,5%	1,12		Without extreme reflection
009	4,7%	1,17	Slit #4	
010	4,7%	1,17		
011	4,3%	1,07	Slit #2	With extreme reflection
012	4,8%	1,19		
013	4,3%	1,07		
014	4,3%	1,07	Slit #4	
015	4,3%	1,07		Without extreme reflection
016	4,2%	1,04	Slit #1	

Four new slit geometries were constructed with a CNC milling machine at IFT's workshop (see Figure 4-15). All slit geometries had the same main properties (length, width and depth). The geometries were polished with sand paper since the surfaces were initially reflecting. The angled sight detector was modified so it would be easy to change slit bricks between tests. The slit properties are listed in

Table 4-13.

Table 4-13: Slit configurations for test series 00007

Test series 00007	
Slit no.	Slit configurations
1	Width: 0,65mm ± 0,05, angle 60 ± 2°
2	Width: 0,95mm ± 0,05 , angle 60 ± 2°
3	Width: 1,15mm ± 0,05 , angle 80 ± 2°
4	Width: 0,45mm ± 0,05 , angle 80 ± 2°

The four slit blocks are manufactured of PVC material and slit opening width measured using a feel gauge from Teng Tools. The milled blocks is shown in Figure 4-15, before being put together. More information about the slit bricks is found in Appendix B.ii – Mark II.

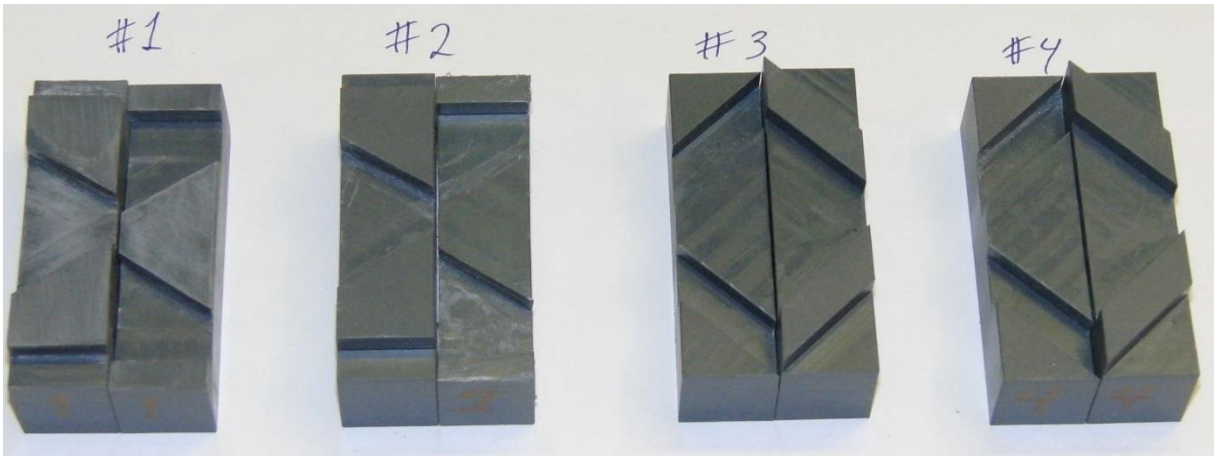

Figure 4-15: The slits geometry bricks used in test series 00007.

Initial tests were performed by using the Casio Elixim camera to take pictures looking through the slits to find the effect of roughening the slits with sandpaper. As Figure 4-16 shows, there were significant reflection effects. The top right picture shows that the reflection above the text “Rechargeable Sealed Lead Acid Battery” is a reflection of the text below ; “FM 12180 12V18Ah/20HR”. This reflection is reduced after roughening with sandpaper (lower right picture).

Figure 4-16: Left: Reference picture, top right: slit before roughening with sandpaper, bottom right: slit after roughening with sandpaper.

The flame front positions relatively to the angled sight detector during explosions were measured for the four different slit bricks. Figure 4-17 shows the specific slit bricks used on the y-axis with respective measured flame front position relative to the angled sight detector in centimeters, on the x-axis. The measured flame front positions differ for the slit bricks. Slit brick #1 struggled to detect the lean mixture of 3.8% propane, also the rich mixtures detects too late. Slit brick #2 indicates more accuracy with a small degree of independence of both concentration and the presence of extreme reflection. The main trend in Figure 4-17 shows that all detections were either late or approximated accurate. The detected flame front positions are in a range of 0cm to 13 cm.

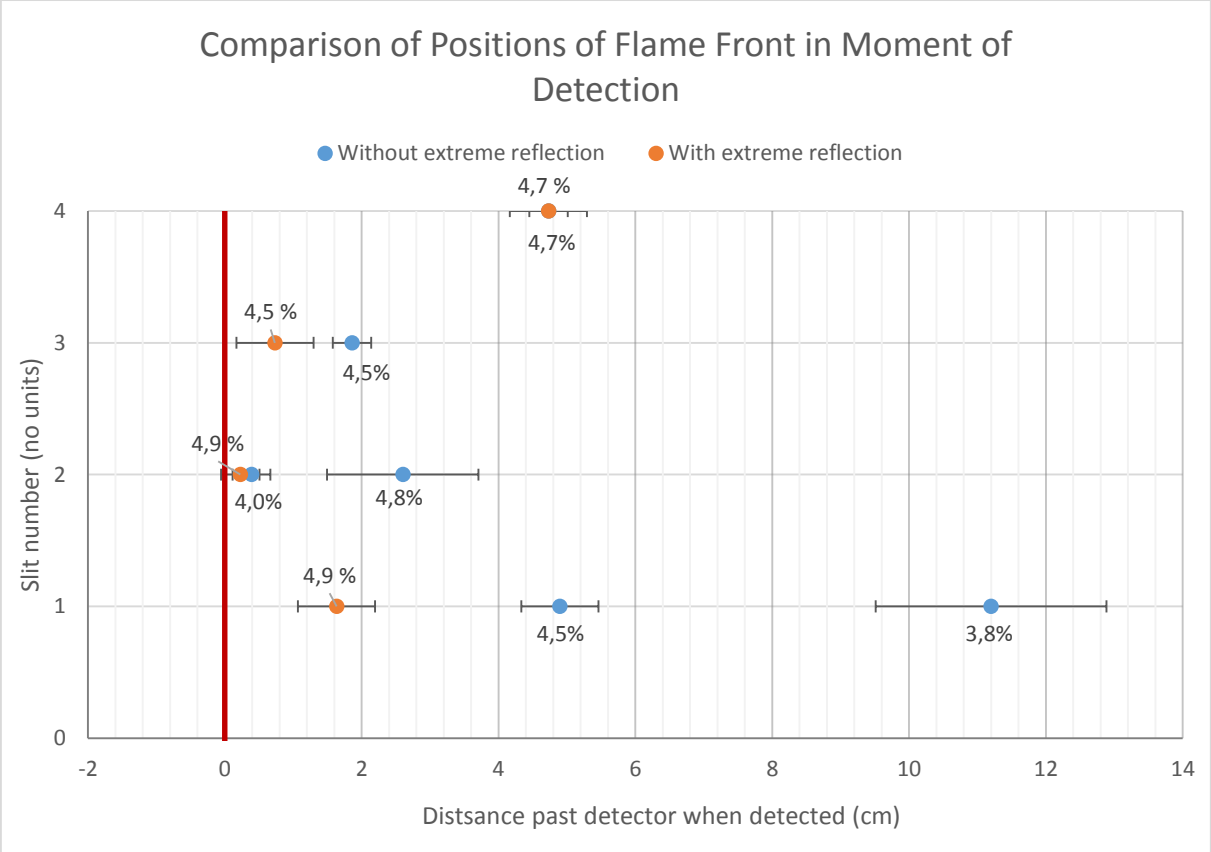

Figure 4-17: Results of comparison study during test series 00007.

Figure 4-18 shows the detected flame front positions relative to the angled sight detector, with the second reflection configuration of the transparent plastic. When comparing this figure with Figure 4-17, half of the tests were early detection and the other were late detections within a range of -8.1cm to 4.5cm relative to the angled sight detector. Figure 4-18 indicates that the accuracy problem does still exist even when the slit and reflection configurations are altered.

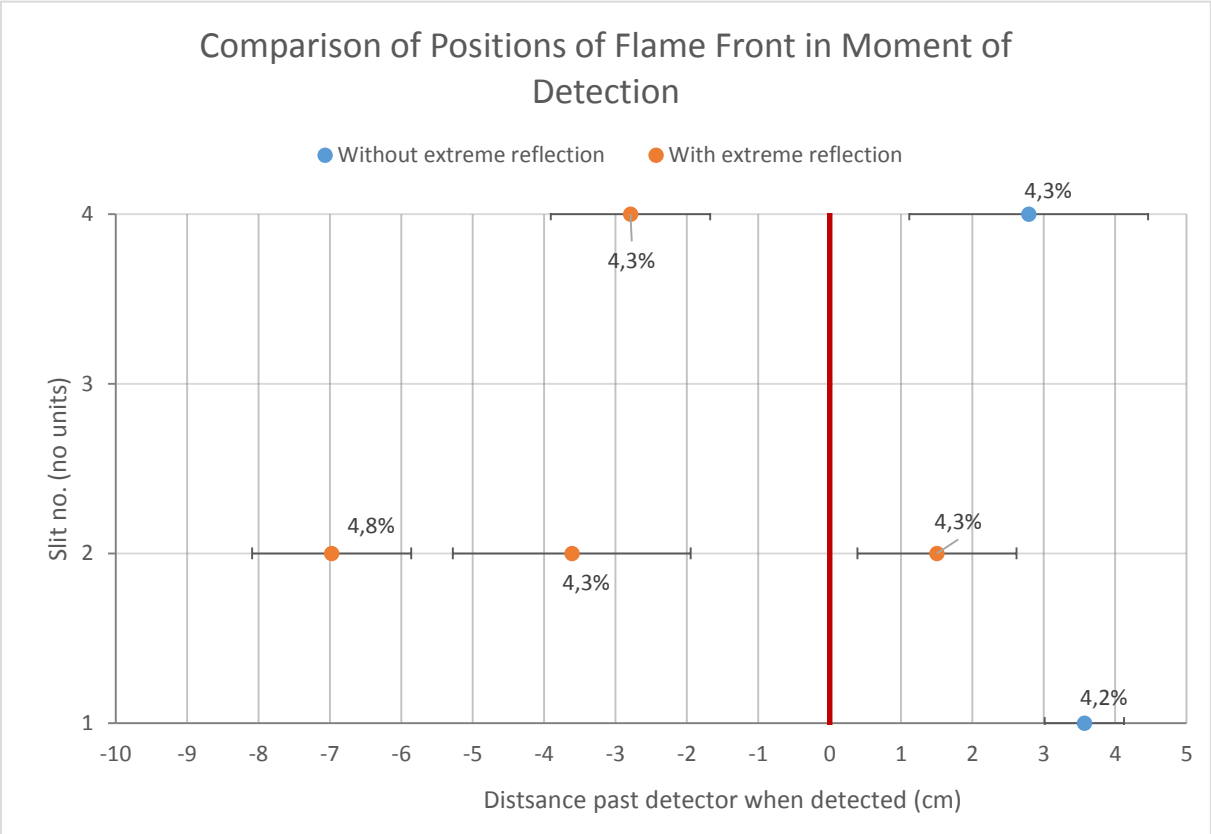

Figure 4-18: Detected flame front positions relative to the angled sight detector for tests 011-016.

Slit brick #2 shows two different detected flame front positions for 4.3% mixture with extreme reflection. The late detection represents test 013 and the early detection represents 011. The reflection configuration of transparent plastic in test 011 made it difficult to determine the position of the flame front. Therefore, the reflection configuration was altered to ease the determination of the flame front position, when detected by the detector. The first and the subsequent reflection configuration is shown in Figure 4-19. The area of the second reflection configuration is less than of the first configuration (test 011). The figure also shows the difference in brightness between a mixture of 4.3% propane and of 4.8%. The differences can be compared at two places, in the flame front and on the reflective inclined plane of the angled sight detector (marked with an arrow). The lower left picture shows a 4.2% propane explosion without addition of the extreme reflection on the angled sight geometry.

Figure 4-19: Top left: first reflection configuration, top right: Extreme reflection, 4.8% propane. Bottom left: Extreme reflection, 4.3% propane, bottom right: no extreme reflection, 4.2% propane.

4.2 Large-scale tests

This section covers the testing of the flame detector for use in large scale. A short test series for proving the functionality was performed in the MOGELEG Channel. The large-scale experiments were carried out in a 50m^3 test vessel (the module). Both tests series were carried out with propane gas as fuel, 00008 with 99.5% propane and 00009 with industrial propane.

4.2.1 Test series 00008 – functionality tests

The test series consisted of five tests with approximately constant fuel-air ratios. The reflection configuration from the previous test series was kept, except the aluminum tape on the windows, which had to be removed. The test configuration of the test series is listed in Table 4-14. The first test used the same sensitivity configurations as test series 00007.

Table 4-14: Configuration for test series 00008

Test series 00008			
Test no.	Gas concentrations	Air-fuel ratios	Reflection configurations
001	4,8%	1,19	Aluminum tape
002	4,8%	1,19	
003	4,8%	1,19	
004	4,7%	1,17	
005	4,7%	1,17	Black duct tape

For test series 00008, the flame detectors for use in large scale had to be mounted on a wooden frame outside the MOGELEG channel, observing its inside. Two of the detectors were positioned in front where the line-if-sight detectors and angled sight detector had been fitted in the previous test series. The third observed just outside the open end, as shown in Figure 4-20.

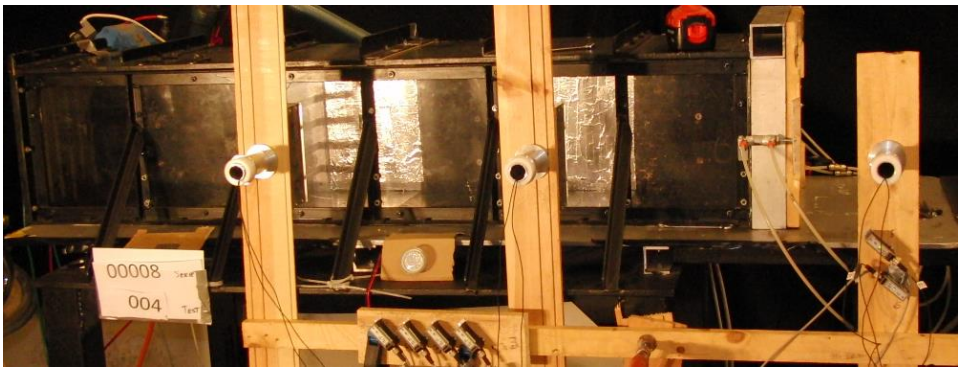

Figure 4-20: The flame detectors for use in large scale mounted on a wooden frame observing the inside of MOGELEG channel and outside the open end.

Due to the new slit properties and detectors positioned outside the channel, the sensitivity had to be fine-tuned in order to obtain accurate flame detections (test 001 through 003). Test 004 were conducted to confirm the detection results from test 003, while test 005 investigated the detected flame front position relative to the flame detector positions without the reflective aluminum tape.

Table 4-15 shows the time of detection after ignition for the three detectors with their six respective sensors. It was important to achieve simultaneous detection from both sensors within each and one of the detectors. The table show some accordance to this fort tests 003 through 005. The largest deviation between a sensor pair is 0.3ms. The averaged deviations between the detection by sensor pairs is equal to 0.1.

Table 4-15: Overview of moments of detection after ignition for test series 00008

Test series 0008						
Test no.	**Time of detection after moment of ignition (ms)**					
	Detector #1		Detector #2		Detector #3	
	FD1	FD2	FD3	FD4	FD5	FD6
001	ND	ND	ND	93,4	88,3	ND
002	84,7	94,4	86,6	89,8	88,0	ND
003	78,2	78,4	84,5	84,5	87,6	87,5
004	78,6	78,7	85,0	84,9	88,1	88,1
005	79,3	79,6	85,0	85,0	87,4	87,3

ND = No detection

Since it was decided that the new detectors would be tested in the 50m^3 module at Sotra, the slit brick no. 2 was chosen on the basis of results from the first part of test series 00007. The module at Sotra have most of the similar properties, with transparent plastic along one of the sides, plastic release system and possibility for HS camera (2000fps). The module is darkened on the inside due to better visual contrast between flame and surroundings.

The first two tests resulted in inaccurate detections of the flame. The reason for this is probably the combination of low sensitivity. Sensitivities were adjusted to maximum since the slits allows less light than before and the casings are rigged externally. The table show some accordance to this fort tests 003 through 005. The largest deviation between a sensor pair is 0.3ms. The averaged deviations between the detection by sensor pairs is equal to 0.1.

Table 4-15 shows that the difference between moments of detection of the sensors within the same detector, are within acceptable time scale. It is also observable that all of the explosions were quite similar and showed a high degree of repeatability. Figure 4-21, Figure 4-22 and Figure 4-23 show the measured flame front positions relative to the detectors during test 003 – 005. Figure 4-21 shows that the flame front positioned of tests 003-004 are slightly passed by a few centimeters the detector. The measure flame front position, however, is around 8 centimeters passed the detector. This trend is also present for the second detector (detector #2) as shown by Figure 4-22. Detector #3, however, is placed outside the open end of the MOGELEG channel where the flame has larger room to propagate. In addition, there were no transparent plastic, which the flame front radiated through. Figure 4-21 shows that the measure flame front positions measure of detector #3 remained constant.

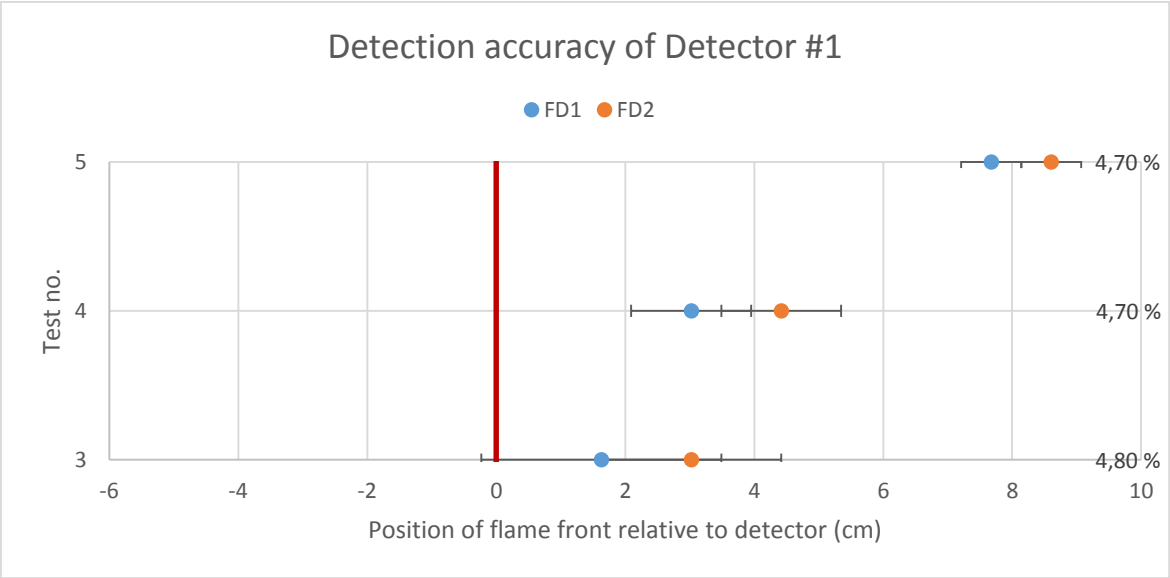

Figure 4-21: Measured flame front position relative to detector #1 .

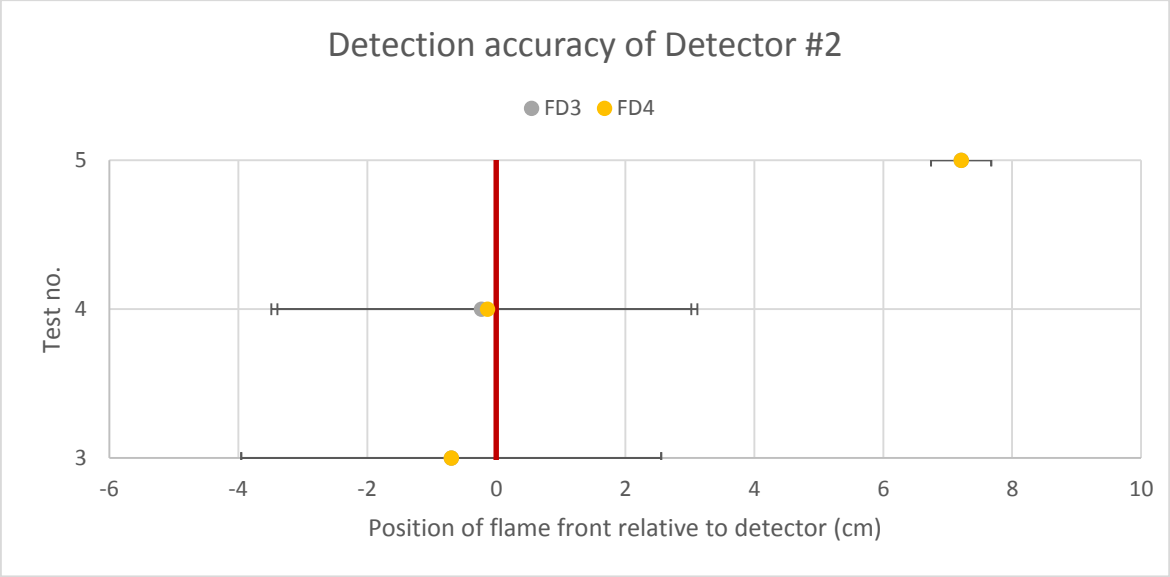

Figure 4-22: Measured flame front position relative to detector #2.

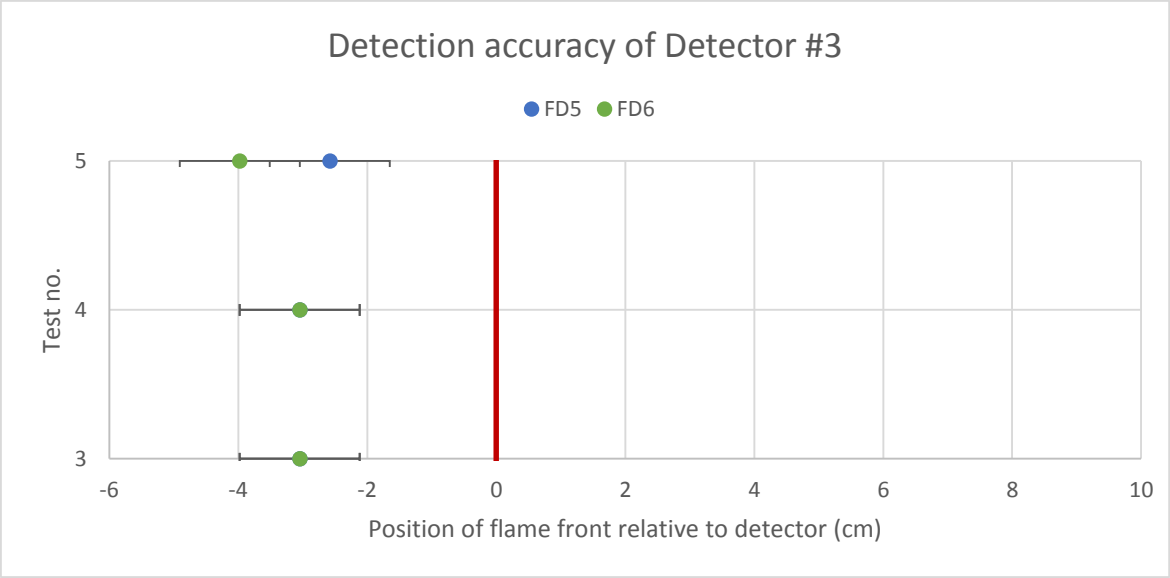

Figure 4-23: Measured flame front position relative to detector #3.

Figure 4-24 shows two subsequent frames from the test 005. The first frame shows the moment of just before FD6 detects the flame, the second frame shows the moment right after detection by FD5.

Figure 4-24: Moments of detections by FD6 and FD5, top and bottom.

4.2.2 Test series 00009 – large scale tests

During test series 00009 the performance of the flame sensors and the flame detectors in premixed turbulent large-scale gas explosions in a 50m^3 module was investigated. The tests were conducted with fuel-air ratios between $0.87 < \phi < 1.09$. The testing of the detectors was carried out in combination of an already ongoing project, hence, detailed information on the test setup is not provided. However a brief overview of the tests configurations is shown in Table 4-16. During the test series, one of the sensors were replaced to give an accurate trigger return of the ignitions source, giving more accurate flame front positions.

Table 4-16: Test configurations for test series 00009

Test series 00009			
Test no.	Gas concentration	Sensitivity configuration	Wall configuration
2	3,8%	High	1 steel (closed end), 3 transparent plastic sections
3	4,0%		
8	3,5%		
10	4,3%	Medium-high	
11	4,3 %		
13	4,2 %		2 steel (closed and open end), 3 transparent plastic sections
14	4,3 %	Medium	
16	4,4%		
19	4,3%	Low sensitivity	

The positions of the flame detectors for use in large scale is shown in Figure 4-25.

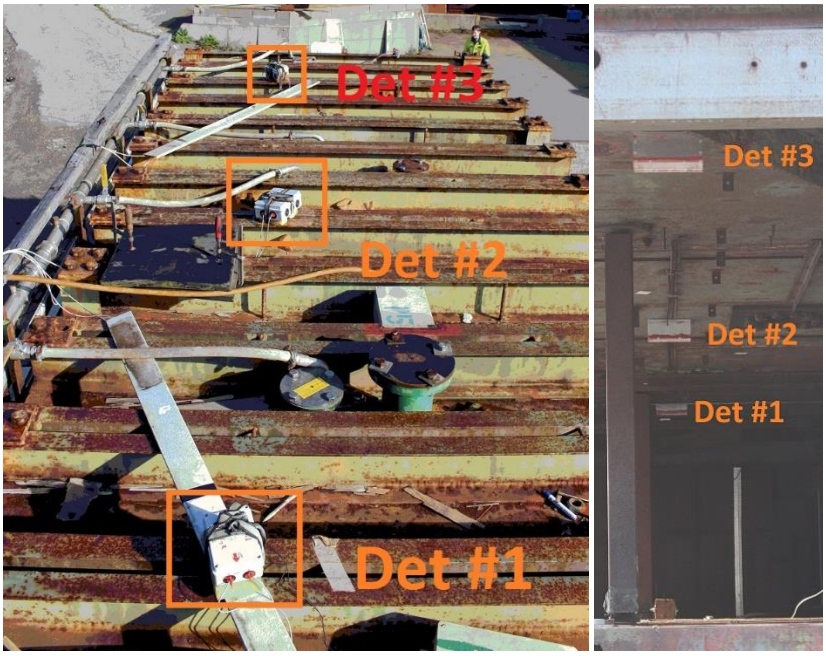

Figure 4-25: Left: Top of 50m^3 module, from closed end, right: The detectors mounted in the roof of the 50m^3 module, from open end.

All the data acquired were reviewed and time between detections and ignition were found and mapped giving measured flame front positions relative to the video recordings. Figure 4-26, Figure 4-27 and Figure 4-28 show the observed flame front positions relative to the flame detector for use in large scale #1, #2 and #3, respectively.

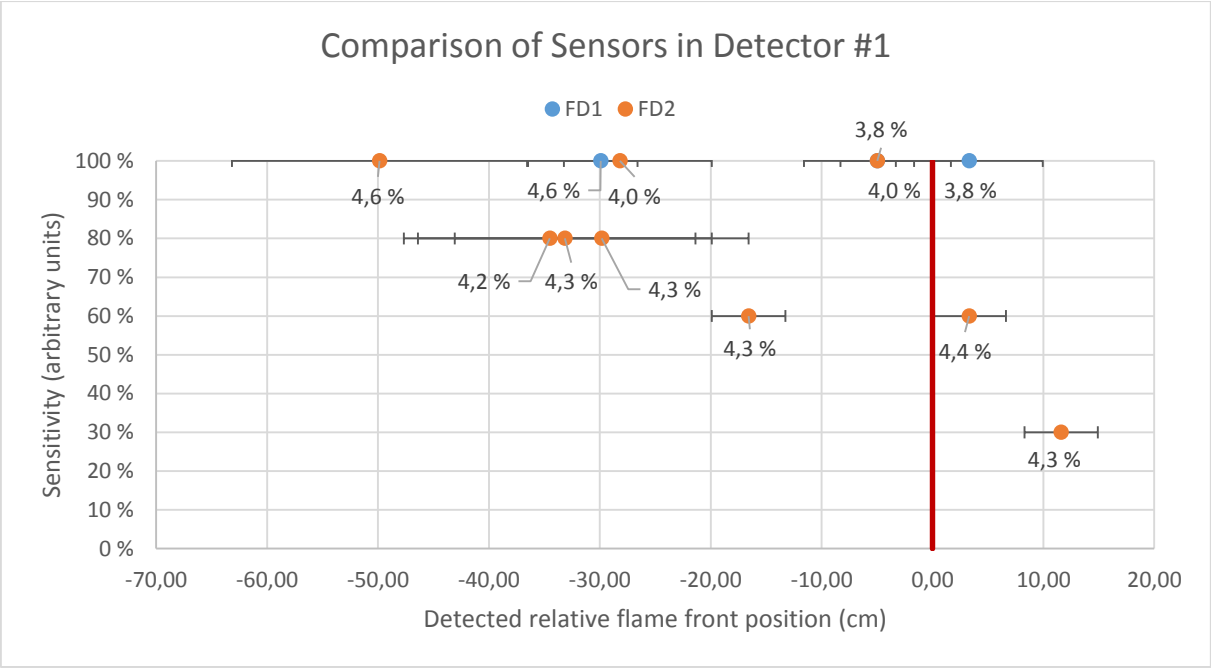

Figure 4-26: Flame front position relative to detector #1.

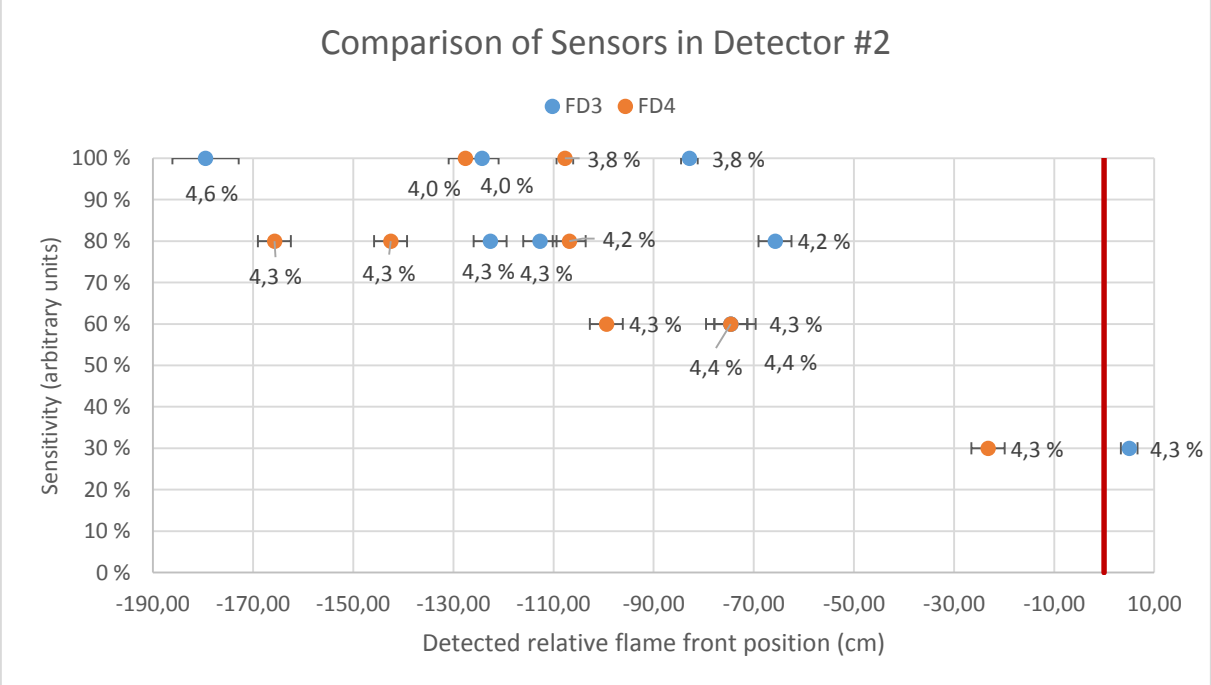

Figure 4-27: Flame front position relative to detector #2.

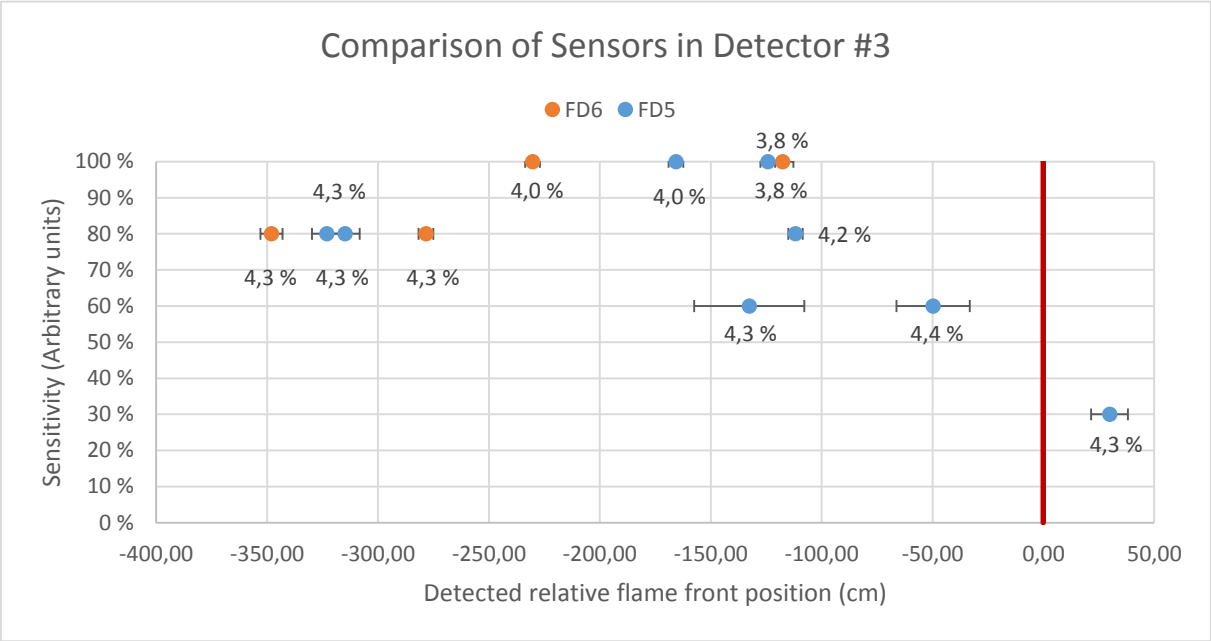

Figure 4-28: Flame front position relative to detector #3.

The three figures above, Figure 4-26, Figure 4-27 and Figure 4-28, shows a trend similar to that of the results during test series 00007 summarized in Figure 4-14. The rich mixtures are strongly represented to the left. Stoichiometric mixtures and lean mixtures tends to be detected later. As the sensitivity decreases, the points gather more and more to the right. The last test, test no 019, shows signs of too low sensitivity since the detections occur too late. The trend shows that fine-tuning is necessary for accurate flame detection. This is the downfall of the detection system, due to the digital amplifiers and their lack of fine-tuning ability and resolution of the sensitivity, the system requires a lot of effort to become accurate within reasonable ranges.

Figure 4-29, Figure 4-27 and Figure 4-28 shows the moments of measured flame front positions relative to detector #1, detector #2 and detector #3, respectively. The figures illustrate the effect of reducing the sensitivity from high to medium-high. For test 013, FD1 and FD6 had stopped working.

Although the reflection challenges during the tests in the MOGELEG Channel were overcome, the magnitude of reflections and emission intensities in the 50m^3 test vessel of another level. The application of “extrapolation” from small-scale to large-scale experiments have been discussed over several decades and to what extent it is within reasonable range. The experiments done in the downscaled model of Gullfaks A compressor module shows some of the problems which could occur when scaling up the size of the test vessel the flame detectors are used within.

An important trend during test series 00009 was that the sensors observing towards the transparent plastic, measured the flame front position before the other sensors, which observed towards the back wall. It is possible to correct this deviation by optimization, hence, it is possible to show more accurate how the flame front propagates through the module.

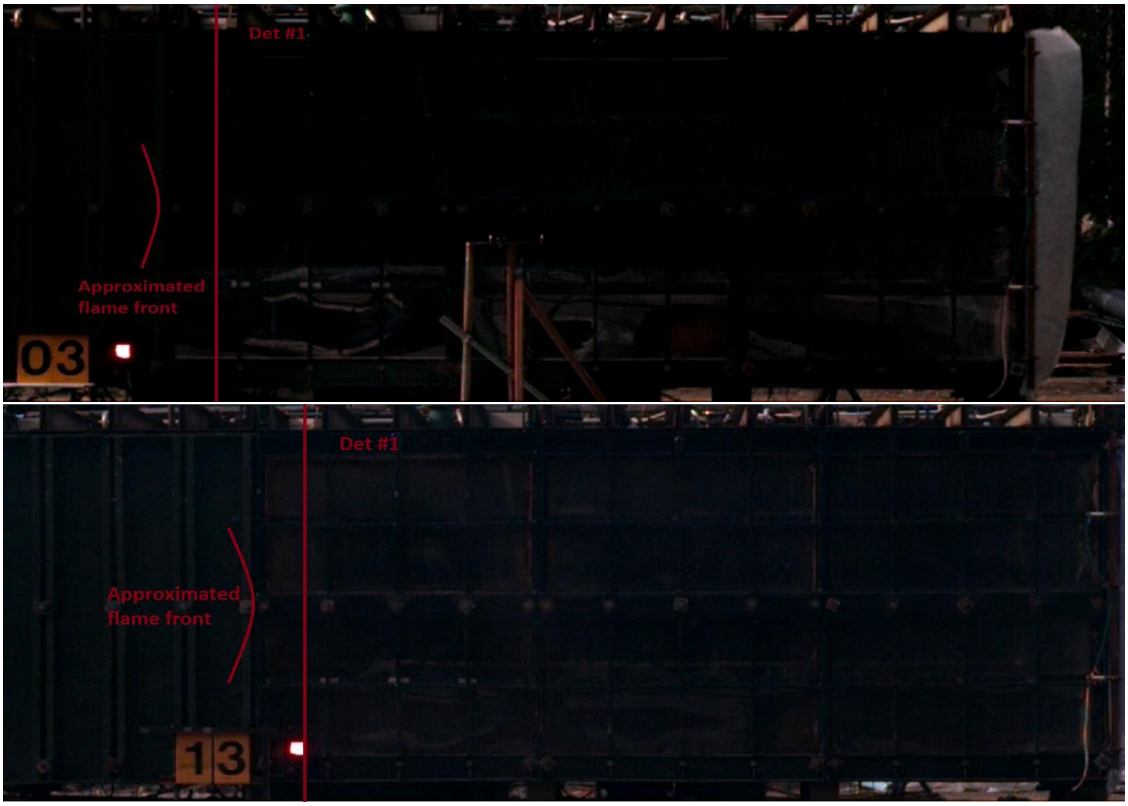

Figure 4-29: Comparison of measured flame front positions by detector #1 during tests 003 and 013.

Figure 4-30: Comparison of measured flame front positions by detector #2 during tests 003 and 013.

Figure 4-31: Comparison of measured flame front positions by detector #3 during tests 003 and 013.

5 Conclusions

An investigation of using photodiodes as sensor inside three different types of flame detectors in laminar, transient and turbulent explosions was carried out. Also, sources for error was detected and investigated, such as the effect of reflective surroundings. Two types of detection methods were tested, line-of-sight detection by observing in a straight line along a narrow cross section of a channel, and angled sight detection by observing with a vertical angle in narrow cross section if a channel.

Experimental data have been acquired through small-scale and large-scale explosion experiments. The analyze gave information about the behavior and properties of the photodiodes. The photodiodes were tested in vented gas explosions of various fuel-air ratios and under various reflection conditions. Experiments with premixed methane/air and propane/air mixtures were carried out.

High-speed cameras were used to pinpoint the actual flame front positions relative to the detectors.

Detectors for use in large-scale explosion have been developed and optimized, based on the data and experience acquired through preliminary tests, modifications and optimization in small scale.

The presented work demonstrates that the photodiodes, without addition of optical filters, can be used as flame sensors. By using a geometry with slit configurations in combination with optimized sensitivity settings, it is possible to achieve high accuracy of measuring flame front positions.

Limitations has been found for line-of-sight detectors of same slit width as angled sight detectors regarding fuel-air ratios $\phi \leq 0.70$, compared to the angled sight detectors which has higher degree of accuracy for a wider range of fuel-air ratios.

No significant differences of measured flame fronts positions relative to the angled sight detector were noted during small-scale experiments, after propane substituted methane as fuel.

The reflection challenges regarding large-scale explosions were reduced through optimization of the amplifier sensitivity. The much higher magnitude of emission intensities in large-scale experiments, compared to that of small-scale, was coped with by sensitivity adjustments.

6 Recommendations for Further Work

Significant changes of test conditions lead to much effort regarding optimization of the detectors, to achieve sufficient and satisfactory measured flame front positions. To ease this process in the long run, an analogue amplifier could be developed. The amplified output signal should be run through an algorithm that depends on both the gradient of the output signal as well as a threshold value.

To reduce the reflection challenges, narrow band optical filters can be added to the photodiodes, hence, large amounts of radiation is filtered out. However, the intensity should be is of sufficient magnitude in front of detector.

To increase the accuracy of the measured flame front positions, photodiodes with sensitivity in the UV area could be used for detection of excited radicals that only exists in the flame. In addition, by adding photodiodes with sensitivity further out in the IR area in combination with optical band filters, it is also possible only to detect the combustion products, i.e. CO_2. Hence, both the flame and the transition into the burnt region is taken into account.

7 References

1. Eckhoff, R.K., *Explosion Hazards in the Process Industries*. 2005: Gulf Publishing Company.
2. *ISO Standards*. 2014 [cited 2014 10.26.2014]; Available from: http:\www.iso.org.
3. Norge, S., *NORSOK S-001*. 2008: standard.no.
4. Mannan, S.D., *Lee's Loss Prevention in the Process Industries*. Vol. 3. 2005: Elsvier Inc.
5. Board, B.M.I.I., *The Buncefield Incidient 11 December 2005 - The ginal report of the Major Incident Investigation Board*. 2008.
6. Board, U.C.S.a.H.I., *INVESTIGATION REPORT OVERVIEW*. 2010, U.S. Chemical Safety and Hazard Investigation Board.
7. UK, O.G. *Piper Alpha: Lessoned Learnt*. 2008 [cited 2014 20. november]; Available from: http://www.oilandgasuk.co.uk/cmsfiles/modules/publications/pdfs/HS048.pdf.
8. Jacobson, E. and O. Spector, *Optical Flame and Gas Detection for the Oil & Gas Industry*, in *Fire & Safety Magazine*. 2005, FS-World. p. 8.
9. Arias, L., et al., *Photodiode-based sensor for flame sensing and combustion-process monitoring.* Applied Optics, 2008. **47**.
10. *Oxford Dictionary - Online*. 2014 [cited 2014 20. november]; Available from: http://www.oxforddictionaries.com/.
11. Warnatz, J., U. Maas, and R.W. Dibble, *Combustion - Physical and Chemical Fundamentals, Modeling and Simulation, Experiments, Pollutant Formation*. 4 ed. 2006: Springer-Verlag.
12. Kanury, A.M., *Introduction to Combustion Phenomena*. 2 ed. 1975: Gordon and Breach Science Publishers.
13. Spakovszky, Z.S. *16.Unified: Thermodynamics and Propulsion*. 2007 [cited 2014 20. november]; Available from: http://web.mit.edu/16.unified/www/FALL/thermodynamics/notes/node111.html.
14. Peters, N., *Turbulent Combustion*. 2000: Cambridge University Press.
15. McAllister, S., J.Y. Chen, and A.C. Fernandez-Pello, *Fundamentals of Combustion Processes*. 1 ed. 2011: Springer.
16. Peters, N., *Lecture 10 - Turbulent Combustion: The State of the Art*, in *Combustion Theory - CEFRC Summer School, Princeton, June 28th - July 2nd, 2010*, RWTH Aachen University. p. 107.
17. Bjerketvedt, D., J.R. Bakke, and K. van Wingerden. *Gas Explosion Handbook*. 2013 [cited 2014 20. november]; Available from: http://www.gexcon.com/article/handbook-content
18. McGraw-Hill, *McGraw-Hill Encyclopedia of Science & Technology - Volume 8*, in *McGraw-Hill Encyclopedia of Science & Technology*. 1987, McGraw-Hill Book Company.
19. Rohsenow, W.M., J.P. Hartnett, and Y.I. Cho, *Handbook of Heat Transfer*. 3 ed. 1998: McGraw-Hill.
20. Lillestoel, E., O. Hunderi, and J.R. Lien, *Generell fysikk for universiteter og høgskoler bind 2*. 2003: Universitetsforlaget.
21. Holman, J.P., *Heat Transfer*. 10 ed. 2010: McGraw-Hill Higher Education.
22. Zizak, G., *Flame Emission Spectroscopy: Fundamentals and Applications*, in *ICS Training Cours one Laser Diagnostics of Combustion Processes*. 2000: University of Cairo, Egypt.
23. Knoll, G.F., *Radiation, Detection and Measurement*. 3 ed. 2000: John Wiley & Sons, Inc.
24. Conti, R.S., K.L. Cashdollar, and I. Liebman, *Improved optical probe for monitoring dust explosions.* Review of Scientific instruments, 1982. **53**(311).
25. Eckhoff, R.K., K. Fuhre, and G.H. Pedersen, *Dust Explosion Experiments in a Vented 236 m^3 Silo Cell.* Journal of Occupational Accidents, 1987. **9**: p. 15.
26. Kalvatn, I.B., *Master Thesis: Experimental Investigation of the Optical Measurement Method for Detecting Dust and Gas Flames in a Flame Accelerator Tube*, in *Department of Physics and Technology*. 2009, University of Bergen. p. 89.

27. Liu, S.X., et al., *Experimental and Theoretical Analysis of Accelration of a Gas Flmae Propagating over a Dust Deposit.* Proceedings of the Combustion Institute, 2002. **29**: p. 6.
28. Bauer, P., *Experimental Investigation on Flame and Detonation Quenching: Applicability of static flame arresters.* Journal of Loss Prevention in the Process Industry, 2005. **18**: p. 6.
29. Babkin, V.S., A.A. Korzhavin, and V.A. Bunev, *Propagation of Premixed Gasous Explosion Flames in Porous Media.* Combustion and Flame, 1991. **87**: p. 182-190.
30. Dorofeev, S.B., et al., *Deflagration to Detonation Transition in Large Confined Volume of Lean Hydrogen-Air Mixtures.* Combustion and Flame, 1996. **104**: p. 16.
31. Haloua, F. and M.L. Brouilette, V. Dupré, G., *Characteristics of Unstable Detonations Near Extinction Limits.* Combustion and Flame, 2000. **122**: p. 17.
32. Pedersen, H.H., *Investigation of Concentration Effects on the Flame Acceleration in Vented Channels.* Tenth International Symposium on Hazards, Prevention and MItigation of Industrial Explosions Bergen, Norway 2014, 2014: p. 505-520.

Appendix A Test Apparatus

A.i MOGELEG Channel setup

The MOGELEG Channel (Mitigation of Gas Explosion …) was built as part of a joint project in 1998 with five sponsors looking into the effects of inert gases on gas explosions. The channel used in thesis is a small-scale model of a four times bigger large scale, used at Sotra.

The channel is original dimensioned 30x30x144 cm, but at the open end, an aluminum frame has been installed due to better compliance of plastic cover, making the channel six centimeters longer.

The experimental setup of this thesis consists of multiple elements, as Figure 3-12: Overview of the experimental setup for the MOGELEG Channel Figure 3-12 indicates,

- Acquisition and trigger system
- Logging card – NI- USB-6259 1.25MS/s
- Valve and fan interface
- High speed camera
- Spark generator
- Plastic release system
- Flame detectors
- Pressure transducer
- Review program – *Plot program.vi*
- Circulation system
- Gas pump
- Gas analyzer
- Gas flow
- Flowmeter
- Compressed gas (fuel)
- Compressed gas (calibration gas)

The acquisition and trigger system has come together as one unit through the VI *Sotralogger.vi* running in LabVIEW on a laptop, the acquisition and trigging occurs through a logging card from national Instruments.

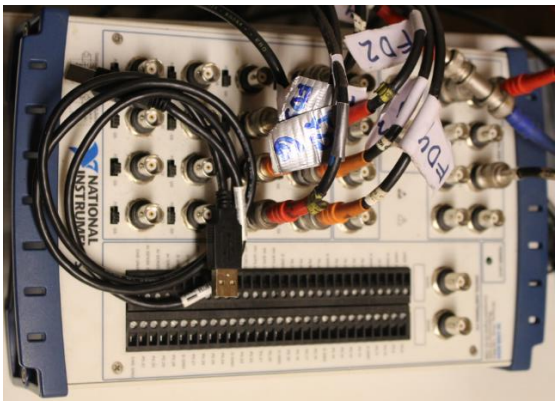

Figure A-1: National Instrument Acquisition and trigger card

Acquisition and trigging system

The acquisition and trigger system has come together as one unit through the VI *Sotralogger.vi*, which runs in LabVIEW on a laptop. The program is an internal IV at CMR GexCon AS and therefore no figures of the programming done in LabVIEW is displayed. The acquisition and trigging occurs through a logging card from National Instruments, NI- USB-6259 1.25MS/s Multifunction I/O with correlated digital I/O, connecting the computer to the HS camera, amplifier for pressure transducer, flame detectors and plastic release system and spark generator.

The program consists of two parts, acquisition and trigging. First part lets the user choose which input channels should be sampled and at what length and rate (time interval and sampling rate, respectively). Second part, trigging, consists of a trigging sequence, which the user can choose the length of and at what moments the specific components shall be trigged. The acquisition of the test series was carried out with a time interval of 2.5 seconds with a sample rate of five per ms (every 0.2 ms), except for test series 00001 which had an time interval of 10 seconds (changed due to unneeded large files).

The trigging sequence was always put to ten seconds. The trigging of camera and spark generator was activated after four seconds. After the plastic release system was mounted, it was trigged after 3.8 seconds, throughout the explosion until 2 seconds later. This was due to the valve configuration in the pneumatic setup of the system. The valve giving pressurized air to the pneumatic cylinders is a three-way type, hence, possible to make the wooden frame pressed against the aluminum frame to keep the plastic in place in normal operating situation. When the valve is trigged, it changes the direction of the air, making the cylinders push the wooden frame away from the aluminum frame. The plastic is now free, but is sticky enough to hang and keep the gas mixture inside the MOGELEG Channel until a small over pressure is generated.

Valve and fan interface

A user face connecting all the valves and the fan were applied during the tests. The four pneumatic valves regarding the circulation system and its fan are coupled into the switch box in the bottom of the picture. The switch box runs on 220V and 12V.

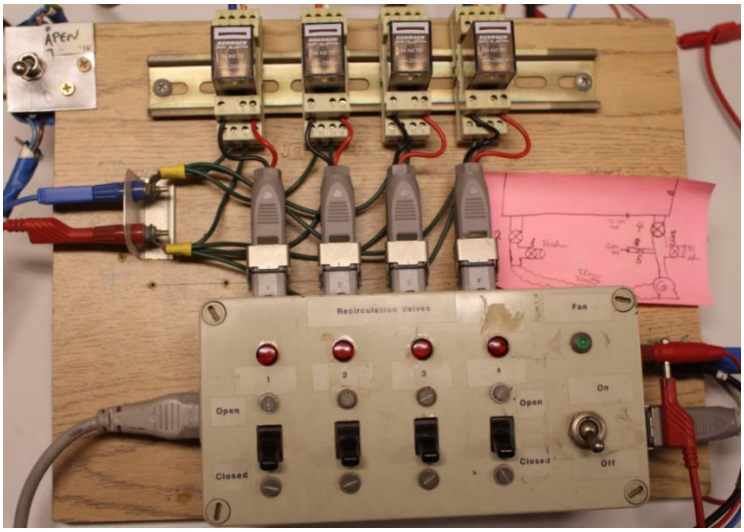

Figure A-2: Valve and fan user face

The 220V are used to switch the four associated three-way valves (marked “B” in) opens and closes the four associated pneumatic valves (marked “A”). The 12V are used on the fan (marked as “C”). Up in the left corner, in Figure A-2, is the switch for the gas valve (valve #5) which is pure electric and opens when its supplied 220V and closes when disconnected.

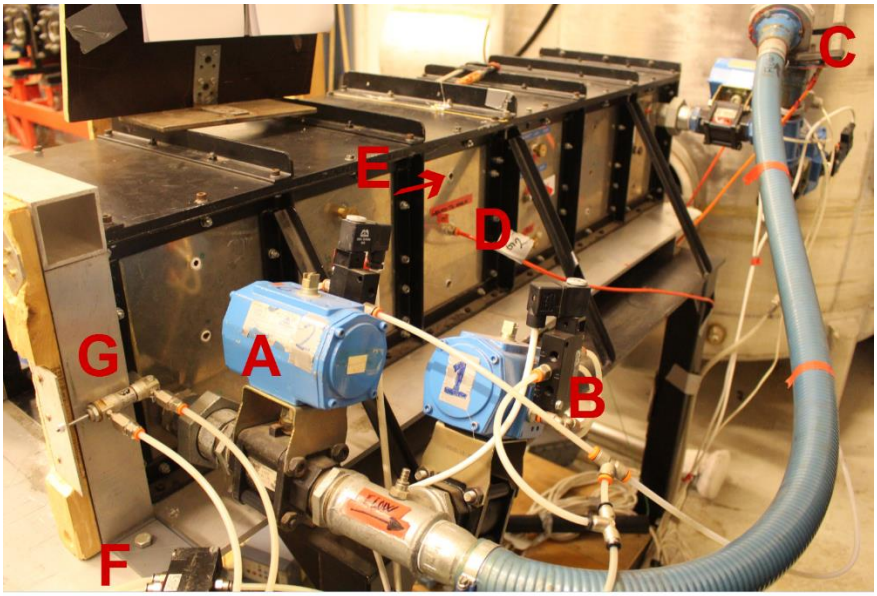

Figure A-3: The backside of the MOGELEG Channel

High-speed camera

Test series 00002 – 00008 was filmed with a Phantom V210 HS camera at 3000 and 5000fps. The camera has the ability to post-trigger, which means that it records continuously over sequence of a length, with a configured frame per second and resolution, relative to its internal memory. This leads to the opportunity to have footage from before the actual trigging has occurred. This is done as a

failsafe against early ignition of the gas mixture. The frame closest after the moment of trigging become frame number zero. When the footage is done, after an experiment, the accompanied software makes it possible to export the video from the camera's internal memory onto the hard drive of the laptop with respective frame number and time after trigged. If the user do not export the footage from camera to laptop before the camera is turned off or a new test is started, the internal memory will be rewritten with the new footage and deletes the previous work.

Figure A-4: Phantom V210 HS camera

Spark generator

The spark generator was built during the thesis of Ivar Børtnes Kalvatn and Gisle André Enstad. The estimated energy generated to be around 50mJ by discharging a capacitor that has been loaded from regular power net, 220V. It is triggered by either a negative or a positive flank of voltage manually or externally.[26]

Plastic release system.

This system was added prior test series 00005, first of the reflection test series. Pressurized air makes the wooden frame push against the aluminum frame with enough force to ensure the plastic foil is in place. By trigging, the three-way valve (marked as "F" in Figure A-3) changes the direction of the air which then makes the pneumatic cylinders to push the wooden frame away from the aluminum frame until the trigging is stopped. During trigging, the plastic foil is sticky enough to keep the mixture enclosed within the channel, until a small overpressure is generated by the combustion.

Gas pump and analyzer

The gas pump is delivered from Håkon Rygh and was kept at 150 ml/min throughout the testing. The gas pump sucked the mixture from the middle of the back wall of the MOGELEG Channel (marked "D" in Figure A-3) and fed the gas analyzer, such that the mixture would be at satisfactory when ignited.

The analyzer would always be calibrated each day of testing with the compressed calibration gas which was fed by the same flow as the monitoring during testing was.

The gas analyzer is a Servomex 4200 Industrial Gas Analyser with accuracy error of 1% of full scale. The gas analyzer is shown in Figure A-5.

Figure A-5: Servomex 4200 Industrial Gas Analyser (picture from www.directindustry.com).

Calibration gases

Table A-1: Calibration gases used

Calibration gases	Compositions
Propane	4.19% C_3H_8 , 95.81 % N_2
Methane	9.78% CH_4 , 90.22 % N_2

Flame detectors

The sensors of the flame detectors was delivered from STM Sensors (now BALLUFF STM). DLM60 can be used as a counter device due to its two main components, a radiator with wavelength of 880nm and a radiation receiver (photodiode) with a responsitivity peak at 850nm. As mentioned earlier, the photodiodes was ordered from the dealer with addition of digital amplifiers. The photodiode has the sensitivity range 400nm to 1100nm with the radiant sensitive area of 0.11mm^2. Due to confidentiality, more information about the photodiode cannot be retrieved.

The amplifiers consists of several OP amps with respective manufacturers:

- MCP6282 – Microchip
- MCP602 – Microchip
- LMV 822 – Texas Instruments/National Semiconductor
- LMV358 - Diodes

Figure A-6: Flame detector amplifiers. A: signal out indication (detection), B: Sensitivity, C: Stability (here: yes), D: Resolution and Delay settings.

Figure A-6 shows the amplifiers for FD4, FD3 and FD2 on the left and on the right their user face. The thin black cable is signal from the photodiodes and the thicker grey cable is the amplified signal output.

Pressure transducer with amplifier

A differential pressure transducer of the (Kistler Type 701A) was fitted in the back end (marked "D" in the Figure A-7) of the channel. The pressure transducer registers the change of pressure in terms of difference from the initial state (1atm). The magnitude of pressure changes is represented by the magnitude of voltage output. The signal from the transducer is quite small and must be amplified the shortest signal cable and amplifier closest possible due to signal loss and contamination of signal by noise from surrounding cables.

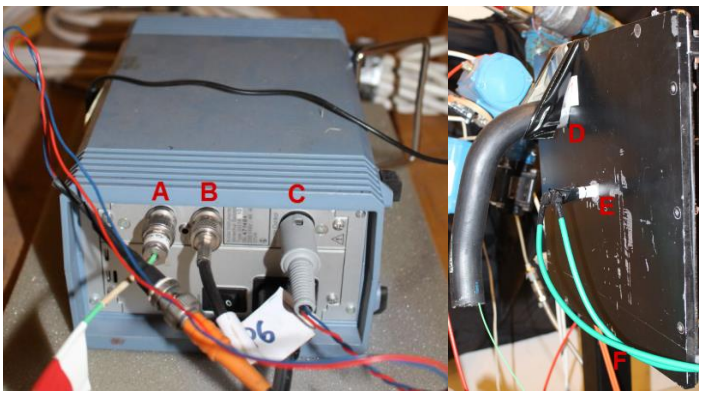

Figure A-7: Pressure transducer amplifier and pressure transducer fitted into the back of the closed end of MOGELEG Channel.

Figure A-7 shows six point,

A The signal output from the sensor to the input of the amplifier (blue box, left).
B The acquired amplified signal output of the pressure.
C The trigger input from user.
D The fitted pressure transducer, partly covered from the electrical cabling with tubing
E The fitted ignition source
F The electrical cables, turquoise is for the ignitions source (220V) and orange (12V) for the fan

Appendix B Development of detectors

Three versions of angled sight flame detectors were developed during the thesis. The drawings were created with help of *Google Sketchup*. The three models are named Mark I, Mark II and Mark III, respectively.

All detectors and the development and modifications was made at workshop at IFT.

B.i Mark I

This was the first model. The geometry was designed with some roughness with *Google SketchUp*. Several ideas for the design was discussed but the final design for the model was considered better due to the position, vision and applicability of the detector. The geometry consists of two parts that is fitted together, making the slit opening. The geometry dimensions as whole equals 120x70x29mm. The main idea was to fit the sensor in the back wall with the angled sight geometry on top of it. The geometry was milled with a CNC machine (except the black plate).

Exported pictures from the 3D model in Google SketchUp were used as mechanical drawings.

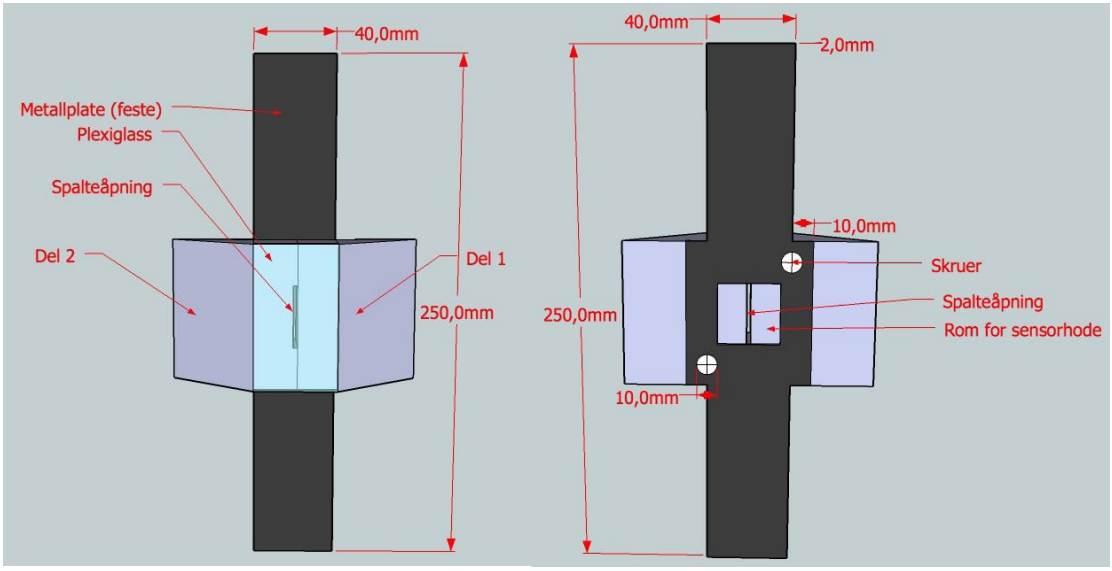

Figure B-1: Front and back of the geometry

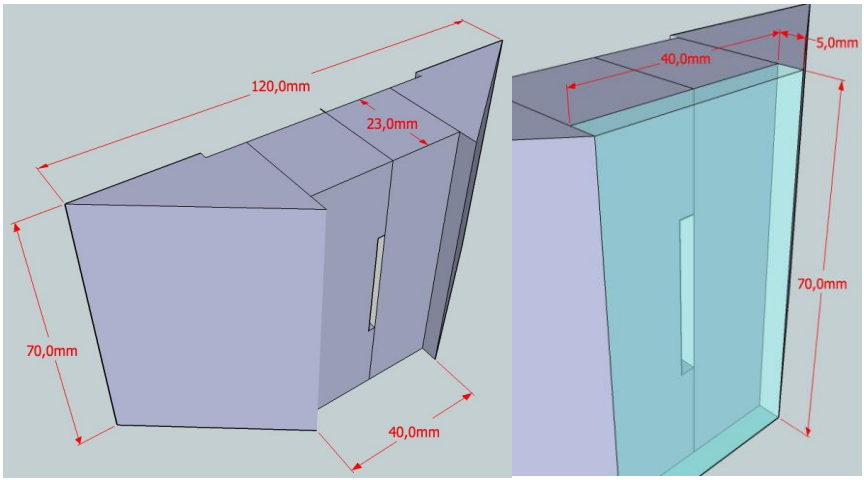

Figure B-2: Front up close without and with PMMA cover

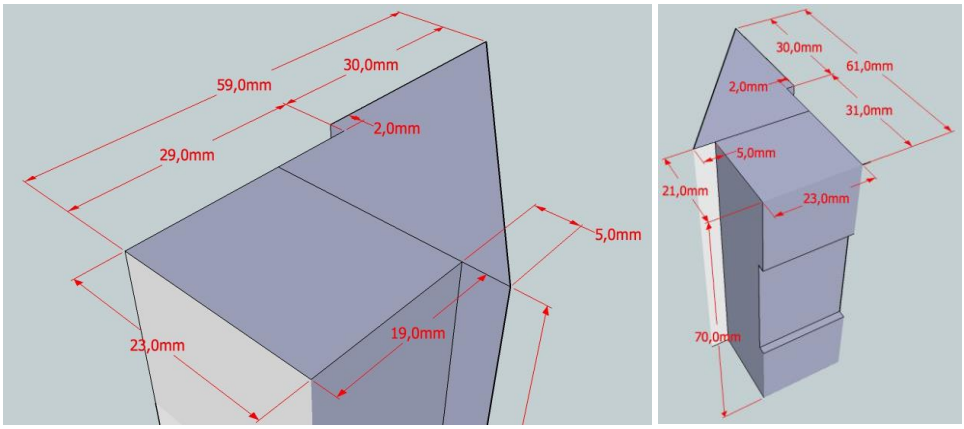

Figure B-3: Part one and two of the geometry

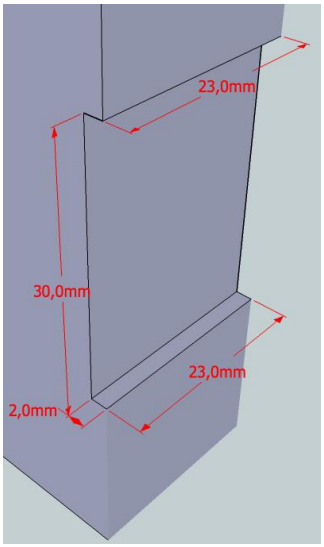

Figure B-4: Slit dimensions on part two.

B.ii Mark II

Most of the space behind the PMMA of Mark I was milled away, giving room for slit bricks with different slit properties. The four bricks were made with manual milling, two parts per brick – bottom and top.

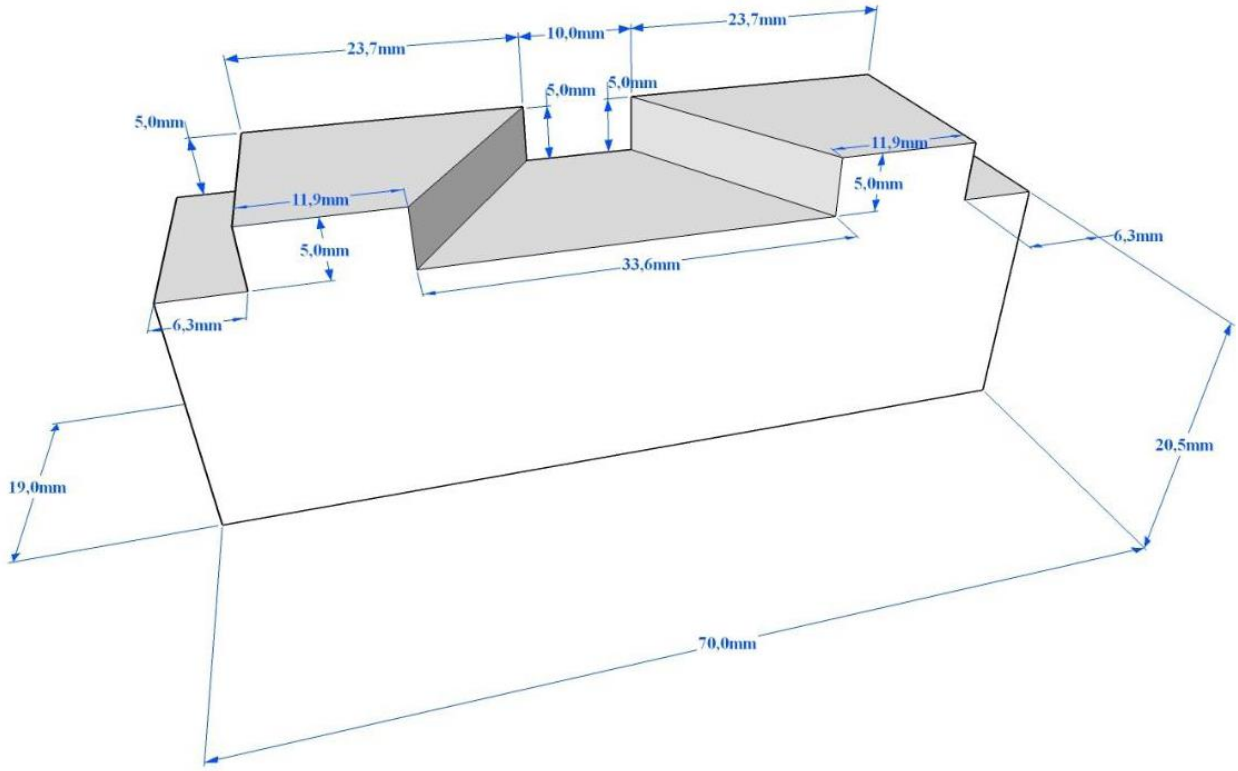

Figure B-5: Slit #1 dimensions, bottom part

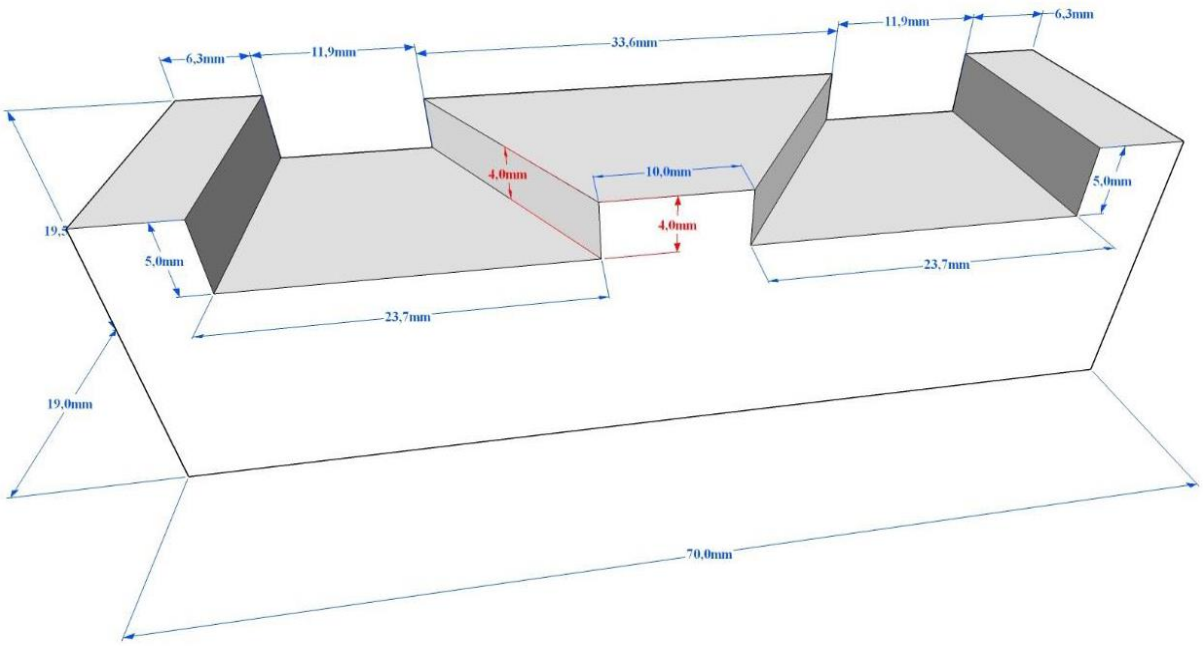

Figure B-6: Slit #1 dimensions, top part.

The top part of the bricks were made with a lowered elevated center than that of the elevation at edges, giving a space between the parts when fitted together. Figure B-6 shows the top part of Slit #1 brick with the center “plug” of 4.0mm height. This plug covers the center hole of slit#1 bottom in Figure B-5 part of brick with a distance of 1.0 mm between the surfaces, the slit.

B.iii Mark III (Flame DetecTHOR)

After the reflection testing during test series 00005 through 00007, it was decided that if the new idea of improved detectors was designed and manufactures fast enough, it was possible to test them in large scale experiments at Sotra. The new idea was to integrate another sensor to the flame detector, giving it a wider total angle of sight. On thought behind this was to see if the flame detector would be both fast and sensitive enough distinguish if the flame front is closer to the inner or the outer wall during propagation.

Since the detector was positioned onto the ceiling, inside of the module, they would be exposed to violent conditions, both temperature and pressure based. Therefore, the sensors was mounted into an enclosure, for each of the detectors. The detector consists of three main parts

- Sensor mounting plate
- Slit brick (mounted on the sensor mounting plate)
- Casing with PMMA and a tube leading the electronics out of the conditions.

Sensor mounting plate

The plate consists of six holes, two large 60° angled sensor fittings and four smaller holes for fastening the slit bricks.

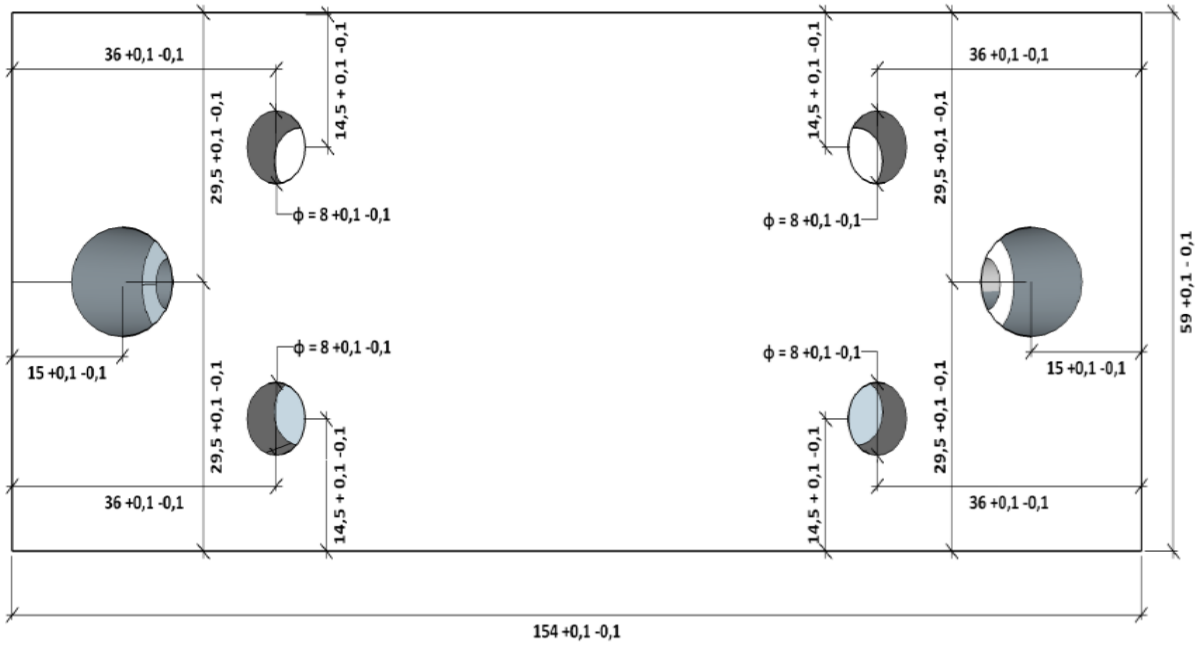

Figure B-7: Sensor mounting plate – top

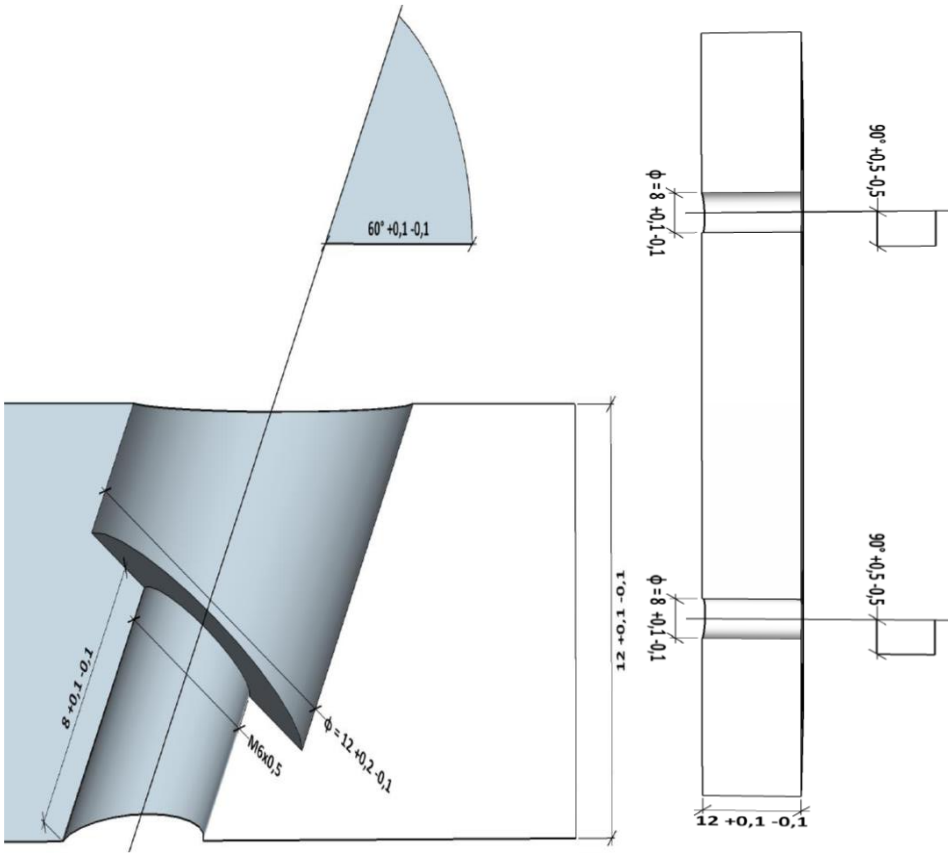

Figure B-8: The angle of mounted sensors and the cross section along the axis holes for slit brick fastenings.

Slit bricks

The slit bricks combined makes the slit with the width and angle corresponding to Slit #2. There are three bricks, to smaller which is the reflection of each other and a third close the gaps, creating the slits.

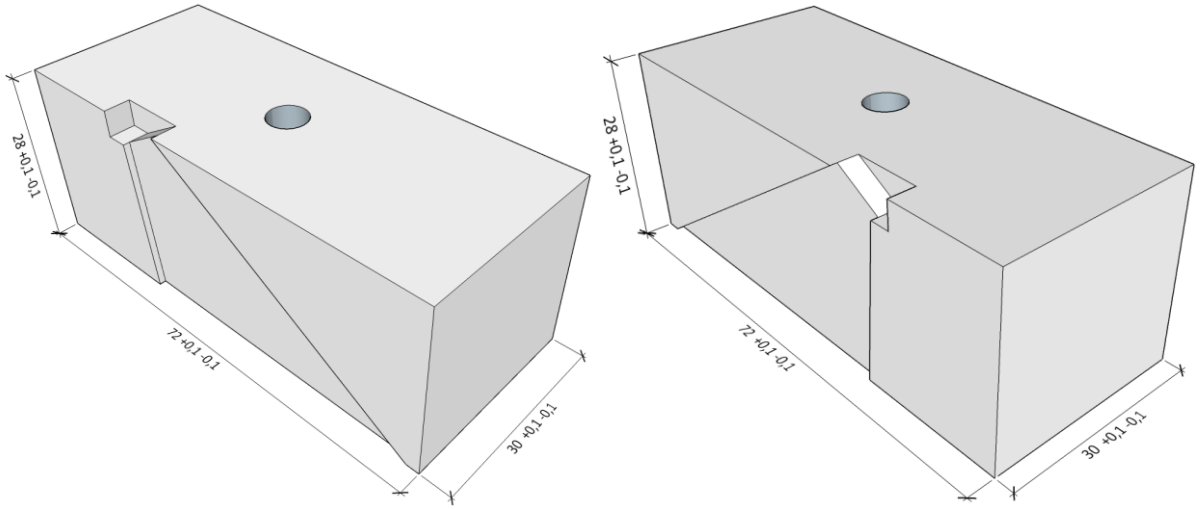

Figure B-9: The left slit brick and the right slit brick, respectively.

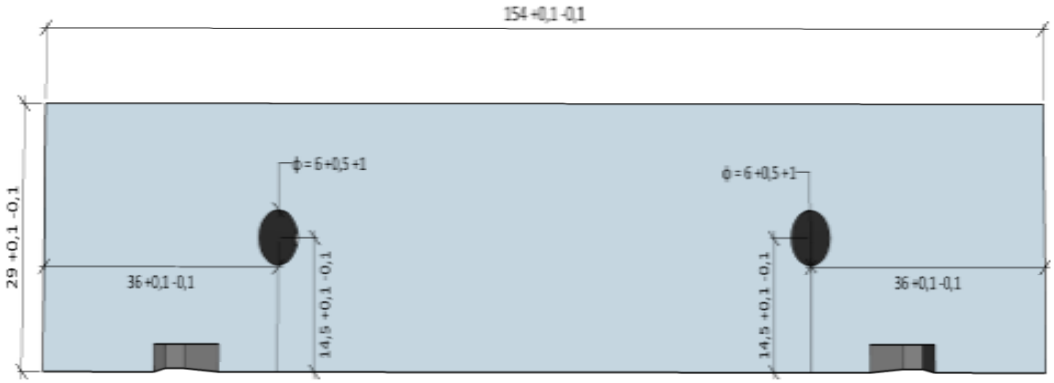

Figure B-10: Top brick, creating the slits.

When the two smaller slit bricks, the large slit bricks and the sensors are fitted to the sensor mounting plate, it will look as Figure B-11. Figure B-12 shows how the slits is fitted into the casing.

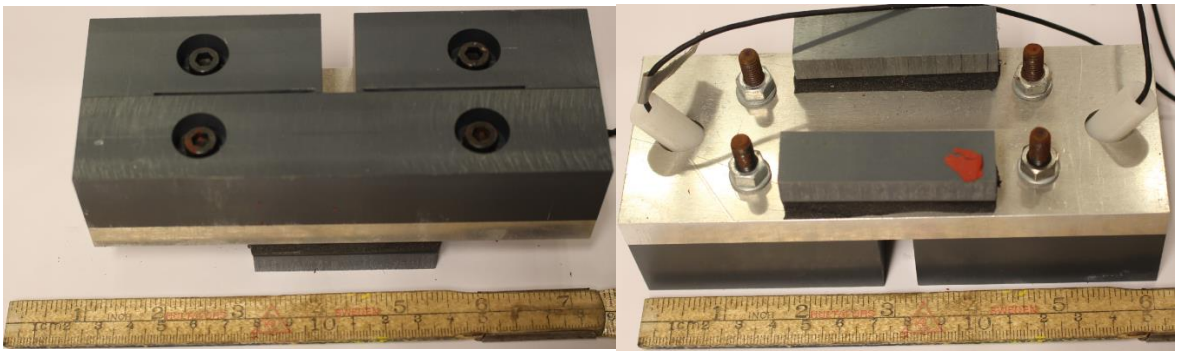

Figure B-11: Fully assembled of detector's sensor mounting plate, bottom and top.

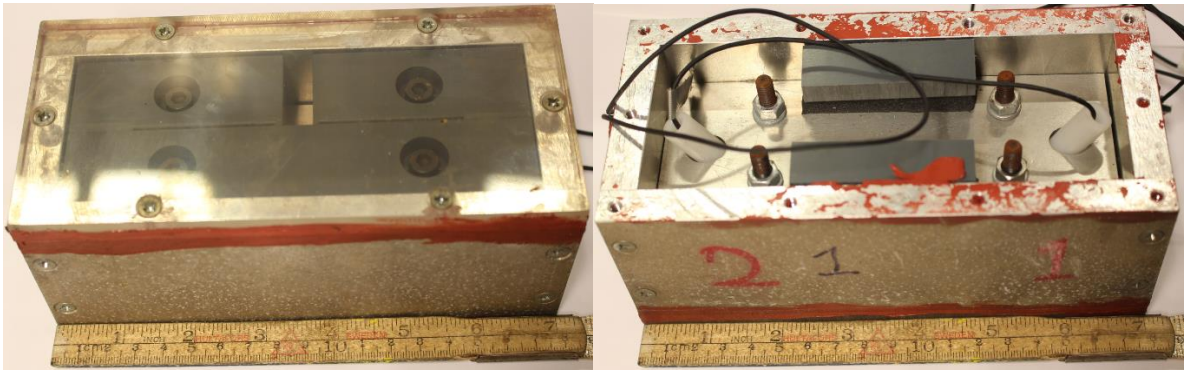

Figure B-12: Left: Sensor mounting plate inside casing, bottom up, right: fully assembled mounting plate inside casing.

The casing has the outer dimensions 180x80x80mm. The aluminum plates are 10mm thick and make the aluminum frame with a 10mm PMMA bottom. The red numbers “2” and “1” represents the sensor 1 and sensor 2, respectively.

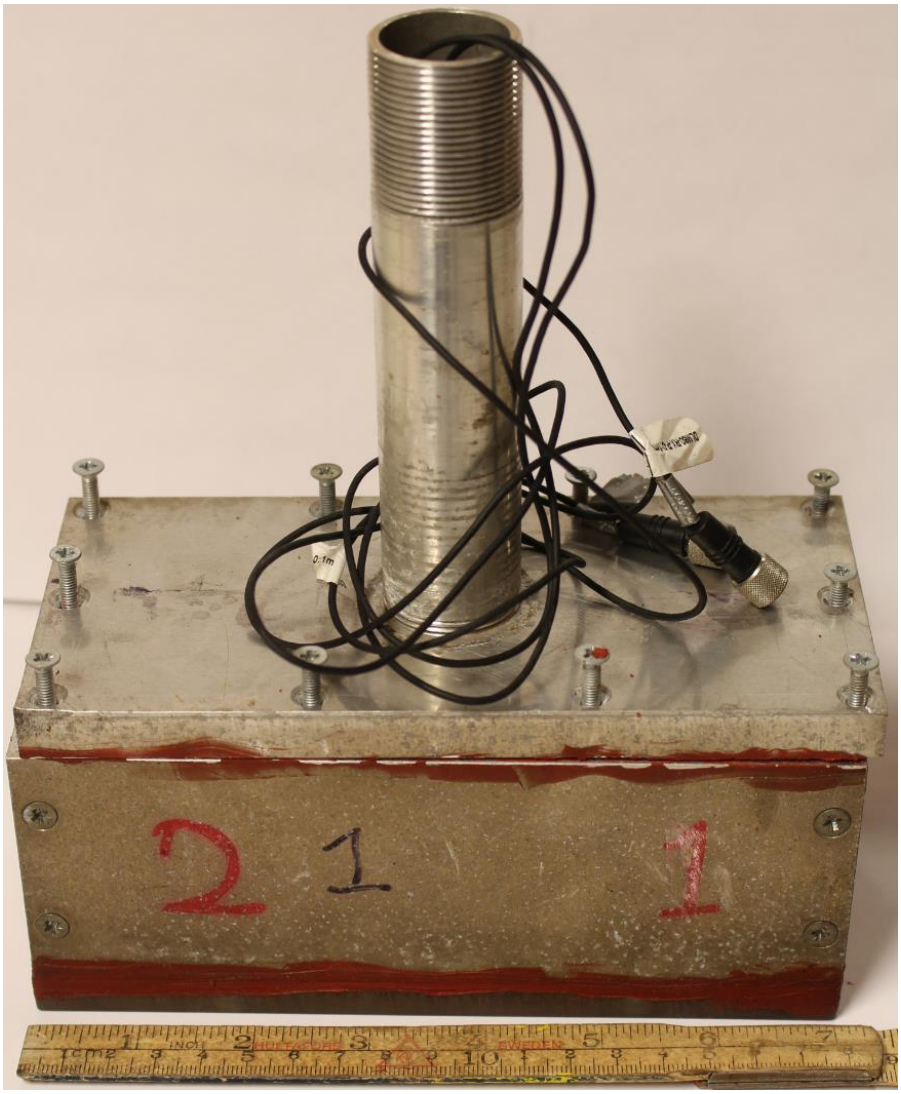

Figure B-13: Assembled detector

The diameter of the pipe is 30mm; hence, it is just small enough to pass through the 1 ¼" fittings, which the deluge system is mounted on (see figure below).

Figure B-14: Deluge fitting with 1 1/4" dimension

B.iv BOROFLOAT® Protective windows for line-of-sight detectors

The following information is gathered from the webpages of edmundoptics.com, November 2014.

5mm Diameter x 1.75mm Thickness, Uncoated, BOROFLOAT® Window

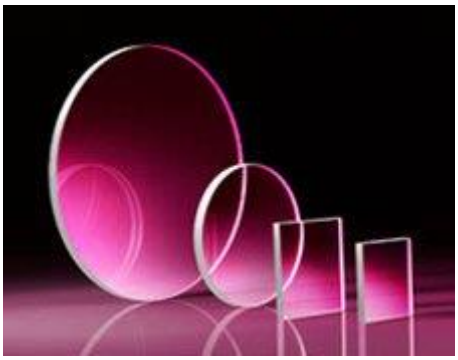

Specifications

Diameter (mm)	5.0
Thickness (mm)	1.75
Index of Refraction n_d	1.472
Abbe Number (v_d)	65.65
Coating	Uncoated
Transmission (%)	90
Surface Accuracy (λ)	4 - 6
Coefficient of Thermal Expansion CTE (10^{-6}/°C)	3.25
Operating Temperature (°C)	1 hour @ 500; >100 hours @ 450
Resistance to Temperature Difference (K)	1 hour @ 110; 1-100 hours @ 90; <100 hours @ 80
Thermal Shock (K)	175
Surface Quality	80 - 50
Diameter Tolerance (mm)	± 0.5
Thickness Tolerance (mm)	± 0.2
Transformation Temperature (°C)	530
Modulus of Elasticity (kN/mm^2)	63
Density (g/cm^3)	2.2
Poisson's Ratio	0.2

Stress-Optical Coefficient (mm^2/N)	4×10^{-6}
Wavelength Range (µm)	0.35 - 2.0
Type	Protective Window
Substrate	BOROFLOAT®
RoHS	Compliant (View Certificate)

Technical Images

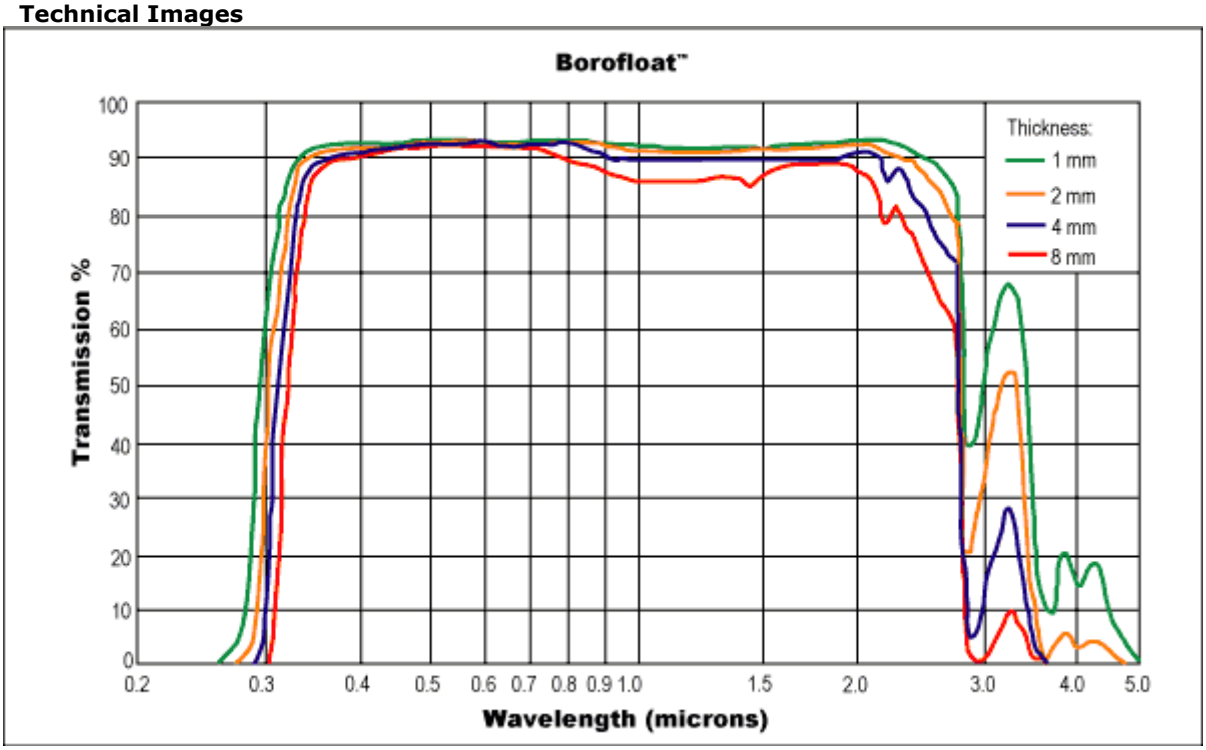

B.v PMMA – Astrup group.

The transparent plastic used on the detectors is of PMMA (polymethylmethacrylate) a substitute for Plexiglas®. The PMMA was delivered by Astrup AS and its transmissivity in VIS is stated to be 92%, as shown in Table B-1.

Table B-1: The general properties of the applied PMMA

			Verdi		
Noen egenskaper	**Norm**	**Enhet**	**Støpt (ST)**	**Ekstr. (EX)**	**Ekstr. (EX) slagfast**
Egenvekt	DIN 53479	g/cm^3	1,20	1,19	1,17
Strekkfasthet	DIN 53455	N/mm^2	74	72	45
Slagfasthet	DIN 53453	KJ/m^2	12	15	60
E-modul	DIN 53457	N/mm^2	3000	3300	2000
Brukstemperatur	–	°C	÷10/+80	÷10/+70	÷10/+70
Lysgjennomgang	DIN 5036	%	92	92	90
Temperaturutvidelse	ASTM D 896	mm/m/°C	0,07	0,07	0,09
Friksjonskoeffisient	Mot stål	–	0,5	0,5	–
Vannopptak	DIN 53495	%	2,1	2,1	2,9
Elektrisk motstand	ASTM D 257	ohm x cm	$>10^{15}$	$>10^{15}$	–
Dielektr. overflatemotstand	DIN 53482	ohm	5×10^{13}	5×10^{13}	$<10^{14}$
Brennbarhet	Normal brennbar (som tre). Avgir ingen farlige stoffer				